UNIVERSITY OF SUSSEX

Strong coupling of a single ion to an optical fibre cavity

Costas Marios Christoforou

Submitted for the degree of Doctor of Philosophy

University of Sussex

September 2020

Declaration

I hereby declare that this thesis has not been and will not be, submitted in whole or in part to another University for the award of any other degree.

Signature:

Costas Marios Christoforou

10th March 2021

UNIVERSITY OF SUSSEX

Costas Marios Christoforou, Doctor of Philosophy

Strong coupling of a single ion to an optical fibre cavity

Summary

Achieving strong coupling between a single ion and a cavity is an important condition for cavity quantum electrodynamics, mainly for its applications in quantum networks, quantum computing and quantum interfaces. While strong coupling has been achieved in various physical systems, so far it remained elusive for single atomic ions. In this thesis I present the first observation of strong coupling between a single ion and an optical cavity. Our system is a hybrid system where a fibre based Fabry-Pérot cavity was incorporated to a 3D Paul trap. The position of the ion, relative to the cavity mode, was adjusted by applying additional rf signals on the radial electrodes of the trap, in order to maximise the coupling between the ion and the cavity. The coupling strength was measured to be $g = 2\pi \times (12.3 \pm 0.1)$ MHz, which exceeds both the atomic decay rate, $\gamma = 2\pi \times 11.5$ MHz, and the cavity decay rate, $\kappa = 2\pi \times (4.1 \pm 0.1)$ MHz, placing the ion-cavity coupling in the strong coupling regime. Cavity assisted Raman spectroscopy was used to precisely characterize the ion-cavity coupling strength, and observe a spectrum featuring the normal mode splitting in the cavity transmission due to the ion-cavity interaction. Due to geometric constraints in our trap, Doppler cooling was not optimal along the cavity axis, hindering the localisation of the ion and thus its coupling to the cavity. To improve the localisation of the ion, cavity cooling was used to efficiently cool the ion along the cavity axis. By using cavity cooling, we obtain an enhanced ion-cavity coupling of $g_0 = 2\pi \times (16.7 \pm 0.1)$ MHz, compared with $g_0 = 2\pi \times (15.2 \pm 0.1)$ MHz when using only Doppler cooling.

Acknowledgements

The work presented in this thesis was carried out from September 2016 until September 2020 in the ion trap cavity QED and molecular physics (ITCM) group at the University of Sussex, under the supervision of Professor Matthias Keller. I am extremely grateful for the amount of support I have received from so many people these past four years.

First, I would like to thank my supervisor, Professor Matthias Keller. You always took the time to answer thoroughly every question I had, and help me with my research. I appreciate everything you did for me and it was a privilege working under your supervision.

I would also like to express my gratitude to Hiroki Takahashi. You were a great mentor and a good friend. Thank you for being patient enough to answer all my questions. You taught me that hard work pays off. I wish you all the best in your career. Additionally, I thank Ezra Kassa for all his help on the experiment. I appreciate everything you taught me while working together. Good luck in your career.

I want to thank everyone in the lab for making this four years a fantastic experience. Thank you to Amy and Laura for allowing me to "borrow" their equipment when needed. Tom, you have been a great colleague and an excellent scientist. I am sure you will have a successful career in academia. Callan, it was a pleasure working with you. I wish you all the best in your future career. Samir, I appreciate that you took out of your time every time I needed help. Good luck to you and your family. Hamzah I wish you all the best in your future endeavours. Xavi, I knew that I could always count on you when I had a technical problem. Gracias por todo. Thanks to Sam, you were great company during the long hours in the office. Good luck with your research. Good luck to David and Travers on their experiments. Finally, I would like to thank Corentin, for helping me set up the cavity cooling experiment. Thank you for carrying on the experiment. I wish you good luck in the future.

I would like to thank Kate for her support and understanding during my studies. Thank you for putting up with me and my insane work schedule. Jason thank you for all your help. I will miss our discussions over coffee.

I would also like to thank all my friends in Cyprus for their support and friendship. Talking to you was my remedy when I was feeling homesick. To all my friends in the UK, you were my family away from home. Tassos, Katerina, Georgia, Stefanos, Marita thank you for being there for me all these years, whenever I needed you. ¨Φιλία εστί μία ψυχή εν δυσί σώμασιν ενοικουμένη'

I would like to express my gratitude to my family. Evgenia, Christian, Christina, Savvas thank you for your encouragement and your assistance. Lastly but most importantly I would like to say a big thank you to my parents Despina and Charalambos. Your constant support was more than I could ever ask for.

To my father Charalambos,

My best friend and my guiding light.

Contents

Chapter 1

Introduction

The idea of creating a quantum processing unit is not a new concept. Although recently quantum computers have got a lot more publicity, especially in this age of social media. This goes back to great visionaries like Feynman [1] and Deutch [2] . These pioneers, and others, envisioned another way of manipulating and carrying information, not bound by the laws of classical mechanics but by the laws of quantum mechanics. The realisation of a quantum computer will revolutionise our world, changing the way we approach cybersecurity, improving drug development, optimising traffic solutions and many more [3].

Although the ultimate power of classical computers is not yet known, it needs to be understood that a quantum computer will not be fundamentally faster than a classical computer. By comparing the complexity (the amount of resources, like time, required to run an algorithm) of the solution, in some cases a classical computer will perform just as well as quantum computer [4]. In some cases a quantum processors will offer a moderate increase in complexity, such as Grover's algorithm [5]. Grover's algorithm can search an unsorted database with N entries in $O(\sqrt{N})$ time complexity, compared to a classical computer where this process is done in $O(N)$ time complexity. In other cases a quantum processor will offer an exponential increase, like Shor's algorithm [6]. Factoring an arbitrary large number N into prime numbers can be done in $O(\log(N)^3)$ time complexity with Shor's algorithm, while there is no known classical algorithm that can factor a number N in time $O(\log(N)^k)$ for any k. In the field of communications, a quantum computer can offer both quantitative and qualitatively improvements compared to a classical machine [7] [8].

Having seen the benefits of building such a system we now move on to the hard part of how to build such a machine. In 2000 DiVicenzo published a paper where he layed out the blueprint of how to build a quantum a computer [9]. What follows are the DiVicenzo criteria, which are necessary for a physical system to be able to work as a quantum computer.

1. **A scalable physical system with well characterised qubits.** A qubit is "well characterised" if its physical parameters are accurately known, including its Hamiltonian, the presence and couplings to other states of the qubit, the interactions with other qubits, and the couplings to external fields used to manipulate the qubit.

2. **The ability to initialise the state of the qubits to a simple fiducial state, as $|000...\rangle$.** The registers of the system need to be initialised in a known value before the start of computation. Additionally, qubits prepared in a certain quantum state are required for error correction.

3. **Long decoherence times, much longer than the gate operation time.** The execution time of any individual quantum gate must be significantly shorter than the decoherence of the qubit state.

4. **A "universal" set of quantum gates.** The physical system provides the means to implement a universal set of quantum gates. Any algorithm can be realised in this system by using a finite set of quantum gates.

5. **A qubit specific measurement capability.** The result of the computation must be able to be read after its completion. Therefore this system must be able to measure the final state of the system. If the measurement is non-destructive it can be also used for state preparation, but this is not necessary.

These criteria are enough for computation, but as stated earlier if communication is needed in order to create a quantum network, or a modular quantum computer architecture, these criteria are expanded to include two more.

6. **The ability to interconvert stationary and flying qubits.** The ability to transfer the quantum state of a stationary qubit to a flying qubit and vice versa for communication purposes.

7. **The ability to faithfully transmit flying qubits between specified locations.** This criteria is essential when you consider communication protocols such as quantum key distribution(QKD). It is essential for stationary qubits to interact with flying qubits and faithfully transmit those.

Based on these criteria over the past years there have been many attempts to create a quantum computer/network based on different physical systems. Each of these systems have its drawbacks as well as its advantages over the other systems. Some of the most promising realisations include:

- **Superconducting quantum computers.** A superconducting quantum system is built based on superconducting circuits which can contain trillions of electrons. Their quantum state is manipulated by using electromagnetic pulses to control the magnetic flux, the electric charge or the phase difference across a Josephson junction (a device with non-linear inductance and no energy dissipation) [10].

- **Trapped Ion quantum computer.** Using Paul traps, ions can be trapped for a long time and can be used as qubits for the system. Using lasers, coupling is achieved between the internal states of the qubit and the external motional states, as well as coupling between the internal states for a single qubit [11].

- **Quantum computing with neutral atoms.** Using optical traps, 2D and 3D arrays of atoms can be achieved, while preserving the fundamental properties of quantum matter. Using the internal states of these atoms a qubit can be implemented [12].

These are just the most prominent physical implementations of quantum computing, there are of course many others that are not mentioned above which also show great promise [13]. Every system mentioned until now has its pros and cons for being a viable implementation of quantum computer.

In 1994, American mathematician Peter Shor came up with the factoring algorithm that is bearing his name, where a large scale quantum computer can factor into prime numbers any number in polynomial time [14]. Shortly after in 1995, Cirac and Zoller proposed a blueprint where such algorithms could be implemented in a device using individual atomic ions [15]. In this proposal, trapped atomic ions in RF Paul traps serve as qubits. Atomic ions are the ideal candidate for this scheme [16]. This is due to the long trap lifetimes, the ability to entangle ions using the shared ion motional modes, the long internal state coherence times, strong ion-ion interactions and the existence of cycling transitions between internal states of ions for measurement and laser cooling [17]. Using trapped ions single qubit gates [18], two qubit gates [19] and qubit state preparation and detection [20] have been demonstrated with fidelity more than that required for a fault tolerant quantum computer. Trapped ions are still to this day one of the leading physical implementations of quantum computer. The main challenge for trapping ions is scalability, increasing the number of trapped ions while maintaining the abilities mentioned above. Before getting into the challenges faced, we have to check if trapped ions satisfy DiVicenzo's criteria and how. As mentioned before, any large scale quantum computer must abide by these criteria.

For trapped ions, the internal states represent the qubit states $|0\rangle$ and $|1\rangle$. These qubit states can be either: hyperfine qubits; where the states are the hyperfine levels of the atom, Zeeman qubits; where qubits are the Zeeman sublevels, fine structure qubits; where the qubits are the fine structure levels of the ion or finally optical qubits; where the qubits are the energy levels of the ion separated by an optical transition.

Initialization of the ion in a state can be performed by optical pumping into a specific state using laser manipulation. The readout of the final state of the ion is performed by tuning a laser to the specific transition, while the wavelength of the laser is not resonant with any other transition and a detector gathers the scattering of photons from the ion. Usually, these processes are accompanied by laser cooling of the ion. These processes have been demonstrated experimentally in [20] [21] [22]. Applying a laser or a microwave drive, a single qubit gate rotation can be performed. Using the shared motional modes of two or more ions with a couple of single qubit gate rotations, a two qubit entangling gate is realised, normally chosen to be a CNOT gate [23] [24] [25]. Combining the single and two qubit gates, we can form a universal set of gates for quantum computation. The operation times for single qubit gates are around a few microseconds whereas, for two qubit gate between ten and hundred microseconds. The coherence time of ions has been shown to reach 2.1 seconds in optical qubits [26] and 600

seconds for hyperfine qubits [27]. From this comparison we can see that the coherence times are much longer than the gate operation times. Finally, we can see that trapped ions fulfil the essential DiVicenzo criteria for building a stationary quantum computer. The two additional criteria are essential for creating a quantum network, as well as interconnecting ions with photons.

Trapped ions are one of the only few technologies that satisfy DiVicenso's criteria, but why do we choose trapped ions over the competing technologies? To begin, trapped ions have the highest ratio of coherence time to gate operation time than any other technology. The ratio for a two qubit gate for trapped ions is $\sim 10^6$ compared to $\sim$1000 for superconducting qubits [28], and $\sim$200 for Rydberg atom qubits [29].

In addition, for trapped ions, single and two qubit gates can be implemented with high fidelity. Single qubit gates for trapped ions were demonstrated with 99.9999% fidelity [21], two qubit gates with 99.9% for hyperfine qubits [25] [30] and 99.6% for optical qubits [31]. Furthermore, state preparation and readout for trapped ions has been demonstrated with fidelity greater than any other qubit technology [20] [21] [22]. Compared to superconducting qubits, trapped ions are essentially identical while in superconducting qubits frequencies and coherence times differ from qubit to qubit due to the fabrication process [32]. In addition, trapped ions have a limited number of internal states when compared to the continuum of additional states in solid state physics, making them easier to manipulate during any quantum process. Finally, as already mentioned, ions can stay trapped for a long period of time and can easily be reloaded in case of loss or error correction.

Like any other technology, trapped ions have a couple of disadvantages. While the coherence time to gate operation time ratio is highest than any other technology, the gate times are slow compared to superconducting qubits. For example, a two qubit gate in trapped ions is performed in 1.6 microseconds [33], while in superconducting qubits in tens of nanoseconds. Realistically, if trapped ions were used to factor a 1024-bit and a 2048-bit number it would take 10 and 100 days respectively [34]. Therefore, if we want to achieve quantum supremacy [35] using trapped ions we must find a new way for gate operations. Some proposals include entangling gates using sequences of ultrafast pulses [36] or shaped pulses of continuous wave light [33]. In both cases, the gate fidelity did not exceed 76%. Another disadvantage and the main hindrance, is scaling up the system to large number of qubits(ions). For the demonstration of a quantum computer, where it can perform better than a classical computer, in excess of 10^5 qubits are needed [37] [38]. Although large numbers of ions can be trapped in ion clouds, there is no meaningful control over individual ions. The largest ion systems with meaningful control are in linear chains in RF traps [39] and two dimensional arrays [40], although no entanglement between ions has been observed in these systems. Recently IonQ [41] showed a system where they have run single qubit gates on a 79 ion chain, and complex algorithms on chains up to 11 ions. On the other hand, there are systems that can hold thousand of superconducting qubits (D-Wave 2000Q) with limited connectivity between the qubits and similarly no entanglement between qubits.

For all the above reasons (long decoherence times, high fidelity gates, etc), trapped ions are ideal candidates for the realisation of quantum computers. However, as with all the other technologies, the main obstacle from achieving a large scale quantum computer is scalability.

To solve this scalability problem, distributed quantum computing was proposed [42]. In this scheme, many independent small scale quantum systems are interconnected to form a large scale quantum computer or a quantum network. One approach to this modular scheme of quantum computing is monolithic integration, where microfabricated ion trap systems (microfabricated chips) are interconnected together and ions can shuttle between trapping zones [34] [43]. This scheme very much resembles the way classical computers are realized. Using this scheme, it was shown that ions can be transferred between different trapping zones, split chains of ions, [44] [45] as well as move around corners. Nevertheless, the complex fabrication techniques and process unreliability are the main obstacles for scaling up these systems.

In the scheme mentioned above, the qubits are physically shuttled between trapping zones using electric fields. A different method to connect trapping zones is by using photonic interconnects. This allows for photons to distribute entanglement over large distances, making it feasible to interconnect two individual ion traps [46]. It was shown experimentally in [47], that remote entanglement can be achieved between two traps with probabilistic interaction through photons. In this case, the spontaneous emitted light from the ions was collected through an optical fibre, with the polarisation of the collected photon entangled with its parent ion. This photonic entanglement rate was 4.5 s^{-1} with fidelity 78 %. Recently, using a similar collection, by coupling the emitted light to a fibre using a high numerical-aperture, a remote entanglement rate of 182 s^{-1} and 94 % fidelity was measured [48] between two atomic ion qubits.

A significant increase to this rate can be achieved by using an optical cavity. In this scheme, an optical resonator is combined with an ion trap to couple flying (photons) with stationary (ions) qubits [49] [50] [51] [52]. Many smaller scale hybrid systems are interconnected through a photonic(optical) link to create a quantum network, or a large scale quantum computer. Cavity Quantum Electrodynamic (cQED)-ion trap systems are ideal for this scheme since they have been shown to be able to generate a controlled production of single photons [53]. The stationary qubits are used for gate operations, while the flying qubits carry the information to and fro the different subsystems. Using a cQED ion-trap system, entanglement between a trapped ion and a photon was observed over 50 km of optical fibre [54].

This scheme relates back to the two additional DiVicenzo criteria, and how it can be used ,not just to build a quantum network but also as a solution to the scalability problem of trapped ions. The main challenge of this process is to attain coherent control over the interaction of light and matter at the single photon level [42]. Interactions in the node are characterised by the coherent coupling of the matter with light, g, and the parasitic losses

(decoherences) of the system, atomic decay, γ, and cavity decay, κ.

To achieve strong and coherent interactions between light and matter, and increase the efficiency of the system, the ion-cavity coupling, g, should be greater than the decoherences of the system. It has to be noted that there are some proposed schemes for distributed quantum computing where achieving this strong coupling regime is not necessary [55] [56], but all of this schemes have been contested in [57].

The coherent coupling, g, of an ion to an optical cavity is inversely proportional to the cavity volume. Therefore, to increase the coupling and be in the strong coupling regime, the cavity mirrors must be moved closer together to reduce the cavity volume. By doing this though, we reduce the optical access to the trap. In addition, and more importantly, as the cavity mirrors move closer together, the light fields charge the dielectric surface of the cavity, so when incorporated in an ion trap they disturb the trapping field, making the trapping of ions almost impossible [58].

The need for these cavities with smaller volume than macroscopic cavities, led to the development of fibre-based Fabry-Pérot cavities (FFPC) [59]. These cavities are formed by laser machining the end facets of optical fibres to create a curved surface, then coated with a low loss dielectric coating to form a high-finesse cavity. FFPCs allow for greater optical access.

Using FFPCs strong coupling was achieved with neutral atoms [60]. In comparison with trapped ions, FFPCs are easier to incorporate with neutral atoms, since there is no trapping potential to be disturbed by the dielectric coating of the cavities. Nevertheless, since trapped ions are ideal candidates for qubits as explained before (high fidelity gates, long coherence times etc), there have been many unsuccessful attempts over the past years to incorporate FFPCs with ion traps, and achieve strong coupling for ions. In [61], the integration of the fibre cavity with the ion trap disturbs the trapping potential, while in [62], although the ion was coupled to the cavity successfully, it was not well localised and well controlled.

In this thesis, I will report on a hybrid ion trap-cavity system that demonstrated strong coupling successfully for the first time. In our system, FFPCs that were manufactured in our laboratory [63], were combined with a 3D RF Paul trap by shielding the fibre cavities in the hollow trapping electrodes. Using additional RF sources (to the main trapping RF), the ion's position was optimised both radially and axially, relative to the cavity mode to maximise the coupling of the ion to the cavity field. This allowed us to measure for the first time ever a coherent ion-cavity coupling rate greater than both the cavity and the atomic decay.

This thesis will be a paper based thesis. During my PhD work, I have authored and co-authored four peer reviewed publications which will be the main body of the thesis. Before each of the main chapters, I will provide an introduction to the publication included in the chapter as well as my contribution. The structure of this thesis reflects the evolution of our system and the results obtained over the past years.

Chapter 2 will provide a brief overview of the theory, from ion trapping to solving the master equation, to simulations for the experiments. Chapter 3 will include the first publication "Precise positioning of an ion in an integrated Paul trap-cavity system using radiofrequency signals" [64], where a description of how the system was built, and the process of optimising the position of the ion in the cavity mode is given. In chapter 4, I discuss the second publication "Strong coupling of a single ion to an optical cavity" [65], where I explain how we measured the coupling of the ion to the cavity. Chapter 5 covers the third publication "Enhanced ion-cavity coupling through cavity cooling in the strong coupling regime" [66], in which after measuring strong coupling, we used the concept of cavity cooling to improve the localisation of the ion along the cavity axis, and measure an improved value of ion-cavity coupling. Finally the Appendix includes the fourth publication "Cavity-induced anticorrelated photon-emission rates of a single ion" [67]. This publication is chronologically first but I chose to include it as a supplementary material in the Appendix, as I did not see it fitting with the narrative of the main body of the thesis.

Chapter 2

Theory

The purpose of this section is to provide some background information on the theory part of the experiment. Our system is a hybrid system, consisting of an optical cavity combined with an ion trap. Therefore, I will try to cover some basic information on ion trapping theory before moving on to cQED. In the cQED section I will cover the fundamental theory and how we used it in the simulations.

2.1 Ion Trapping Theory

The principle of ion trapping is based upon Earnshaw's theorem [68] that states: *A charge acted on by electrostatic forces cannot rest in stable equilibrium in an electric field.* Therefore, it is not possible to confine an ion using only an electrostatic field. Imagine a charge enclosed by a spherical shell. There is no possible configuration where we apply electrostatic fields on the shell and the charge stays confined at the centre of the sphere. This statement follows from Gauss's theorem, $\mathrm{div}\vec{E} = 0$. Hence, to confine a charge we need to use a time-varying potential.

Wolfgang Paul invented an ion trap, that also bears his name, Paul trap,which can confine an ion in $3D$ [69]. His work won the Nobel Prize in 1989. These Paul traps are made of three metallic electrodes, a ring and two hyperbolically shaped endcaps. On these electrodes a time-varying voltage is applied (Figure 2.1)

$$\Phi_0 = U_{DC} + V_{AC}\cos(\Omega t) \tag{2.1}$$

where Ω is the driving frequency of the AC field and U_{DC} and V_{AC} are the amplitudes of the direct and alternating voltage respectively. There are different ways on how the electric potential is applied on the electrodes. In the scenario in Fig. 2.1, the potential is applied to both the endcaps and the ring with opposite phase. It is also possible to ground the ring electrode and apply the same potential to the two endcaps with the same phase, which is what we did in our system (see Chapter 3).

Using the geometry of the trap in Fig. 2.1 ($r_0^2 = 2z_0^2$) and applying the boundary conditions on the electrodes, we can express the potential Φ in the Paul trap in cylindrical

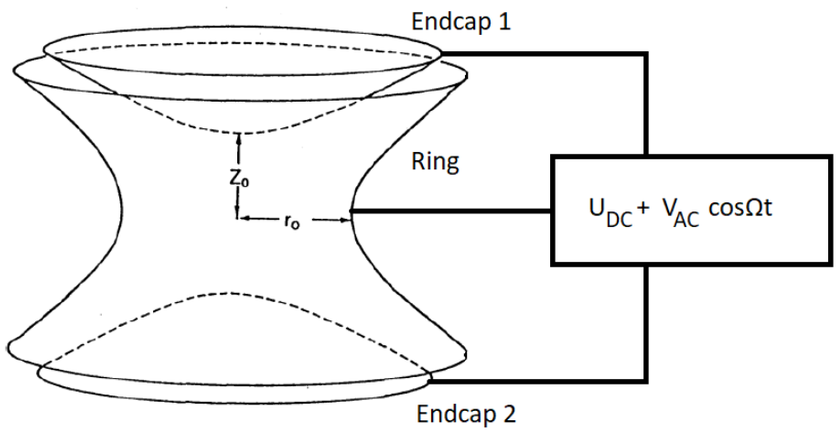

Figure 2.1: A classic representation of the Paul Trap [69]. The distance between the endcaps is $2z_0^2$ and the ring has a radius r_0. The relation between the electrodes is $r_0^2 = 2z_0^2$.

coordinates as

$$\Phi = -\frac{\Phi_0(r^2 - 2z^2)}{r_0^2 + 2z_0^2} \tag{2.2}$$

where $r^2 = x^2 + y^2$ and Φ_0 given by 2.1.

An ion of charge e and mass m in an electric field, according to Newton's second law, obeys the equations of motion given by [70]

$$\ddot{r} = \frac{eE_r}{m} = -\frac{e}{m}\frac{\partial \Phi}{\partial r} \tag{2.3}$$

$$\ddot{z} = \frac{eE_z}{m} = -\frac{e}{m}\frac{\partial \Phi}{\partial z} \tag{2.4}$$

where E_r and E_z are the radial and axial electric fields respectively. Differentiating equation 2.2, the equations of motion become

$$\ddot{r} = \frac{2e}{m(r_0^2 + 2z_0^2)}(U_{DC} + V_{AC}\cos(\Omega t))r \tag{2.5}$$

$$\ddot{z} = \frac{-4e}{m(r_0^2 + 2z_0^2)}(U_{DC} + V_{AC}\cos(\Omega t))z \tag{2.6}$$

Using the substitution $\tau = \Omega t/2$, the equations of motion in dimensionless units become

$$\frac{d^2r}{d\tau} + \frac{-8e}{m\Omega^2(r_0^2 + 2z_0^2)}(U_{DC} + V_{AC}\cos(2\tau))r = 0 \tag{2.7}$$

$$\frac{d^2z}{d\tau} + \frac{16e}{m\Omega^2(r_0^2 + 2z_0^2)}(U_{DC} + V_{AC}\cos(2\tau))z = 0 \tag{2.8}$$

These equations have the form of a Mathieu equation

$$\frac{d^2x}{d\tau} + (a - 2q \cdot cos(2\tau))x = 0 \tag{2.9}$$

By comparison, we can extract the a and q parameters of the Mathieu equation for the radial and axial equations of motion.

$$a_r = \frac{-8eU_{DC}}{m\Omega^2(r_0^2 + 2z_0^2)} \tag{2.10}$$

$$q_r = \frac{4eV_{AC}}{m\Omega^2(r_0^2 + 2z_0^2)} \tag{2.11}$$

$$a_z = -2a_r = \frac{16eU_{DC}}{m\Omega^2(r_0^2 + 2z_0^2)} \tag{2.12}$$

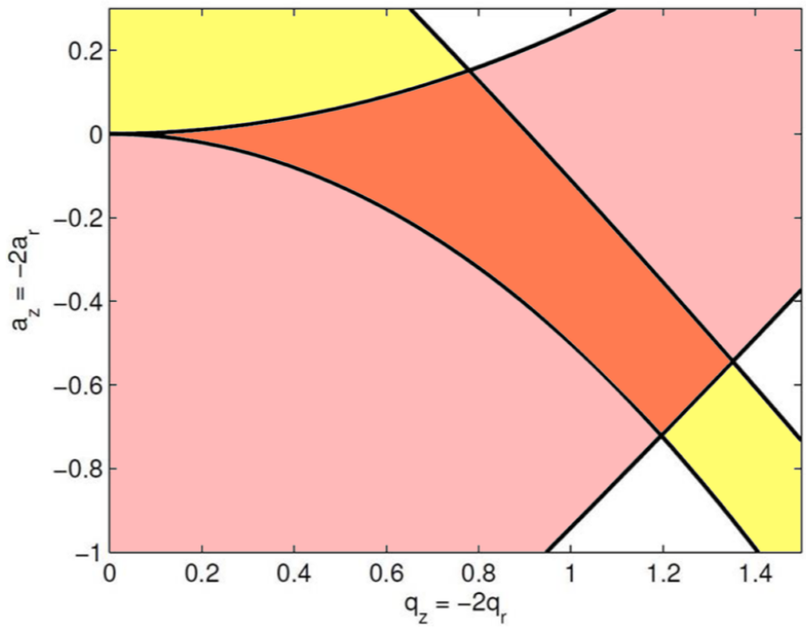

Figure 2.2: Orange area represents the lowest region of stability for the equations of motion of an ion in a quadrupole field [71].

$$q_z = -2q_r = \frac{-8eV_{AC}}{m\Omega^2(r_0^2 + 2z_0^2)} \tag{2.13}$$

There are two types of solutions for the Mathieu equation. The first one is the stable solution, where the ion oscillates with a limited amplitude and the unstable one, where the amplitude of the oscillation increases exponentially and we end up losing the ion. The stable solutions are determined by the a and q values in the radial and axial directions, since the ion must be simultaneously trapped in all dimensions. This is depicted in the stability diagram in Fig. 2.2. For practical reasons, all experimental implementations are restricted in the first stability zone.

For the lowest-order approximation of the solution of the Mathieu equation, in the case of $|a_i|, q_i \ll 1$, $i = \{r, z\}$, the solution to the equation of motion is given by [72] [73]

$$u_i = A_i \cos(\omega_{sec,\,i} t)\Big[1 + \frac{q_i}{2}\cos(\Omega t)\Big] \tag{2.14}$$

where $u_r = r$, $u_z = z$, and A_i is the amplitude of the motion. The frequency $\omega_{sec,\,i}$ is called secular frequency of the ion and it is given by

$$\omega_{sec,\,i} = \frac{1}{2}\Omega\sqrt{a_i + \frac{1}{2}q_i^2} \tag{2.15}$$

In the ion's equation of motion, eq. 2.14, the first term is a harmonic oscillation at the secular frequency which is called secular motion. The second term is smaller in amplitude (by a factor of $q_i/2$), and is modulated by a faster oscillation at the trap's drive frequency, Ω. It is called intrinsic micromotion. In addition, in the presence of a static electric field (E_{dc}) there is an additional term added to the equation of motion (eq. 2.14) [73]

$$u_i = [A_{0i} + A_i \cos(\omega_{sec,\,i} t)]\Big[1 + \frac{q_i}{2}\cos(\Omega t)\Big] \tag{2.16}$$

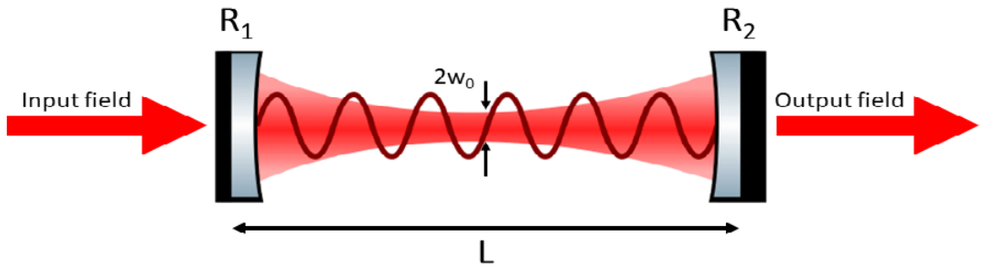

Figure 2.3: Schematic of a simple Fabry-Pérot cavity. The mirrors have radii of curvature R_1 and R_2 and are separated by length L. The cavity mode has diameter $2w_0$.

where

$$A_{0i} = \frac{eE_{dc}}{m\omega_{sec,\,i}^2} \tag{2.17}$$

This term is called excess micromotion and is an oscillation at the driving frequency of the trap, which inhibits the localisation of the ion. More information on how to compensate this micromotion in our system is provided in Chapter 3.

The trap used in our system is a modified version of the one originally designed by Paul, shown in Fig. 2.1. The main drawback of the original design, is that it offers limited optical access to the centre of the trap. Therefore, our trap is an endcap style Paul trap which is based on the one used in [74]. In this design the ring electrode has been split into four cylindrical electrodes, placed in right angles with each other along the radial plane of the trap. The two endcaps are no longer a hyperboloid shape, but hollow cylindrical tubes. While the four radial electrodes are held at RF ground, there is an in-phase RF signal applied to the two endcaps. More information on the geometry and design of the trap is given in Chapter 3.

2.2 Fabry-Pérot Cavity

Our hybrid system incorporates a Paul Trap with a Fabry-Pérot cavity. The simplest Fabry-Pérot cavity consists of two concave highly reflective mirrors with radii of curvature R_1 and R_2, placed parallel to each other at distance L apart, Figure 2.3. The electromagnetic field in the cavity must be zero at the boundaries (mirrors) [75]. Taking this boundary condition into consideration, a standing wave is formed in the cavity if the following condition is met

$$L = n\frac{\lambda}{2} = n\frac{\pi c}{\omega} \tag{2.18}$$

where λ is the wavelength, and $n \in N$ is an integer that describes the number of standing waves. The allowed frequencies of the standing wave are given by ω, and are called longitudinal modes.

$$\omega = n\frac{\pi c}{L} \tag{2.19}$$

The frequency spacing between the longitudinal modes is called free spectral range (FSR) and it is given by

$$FSR = \frac{c}{2L} \tag{2.20}$$

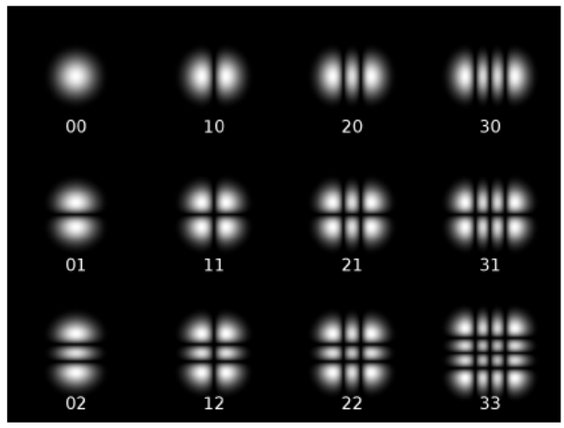

Figure 2.4: Profiles of the first twelve Hermite-Gaussian modes.

The spatial distribution of the electric field inside the cavity can be decomposed into a longitudinal mode function $\Phi(x, y, z)$ and two transverse mode functions $\Psi_n(x, z)$ and $\Psi_m(y, z)$

$$E_{nm} = E_0 \Psi_n(x, z) \Psi_m(y, z) \Phi(x, y, z) \tag{2.21}$$

where E_0 is the amplitude of the electric field and m, n are the indices of the transverse electromagnetic modes (TEM).

The transverse modes can be expressed in terms of the Hermite polynomials H_m and H_n [76], where m and n define a particular transverse electric field distribution. If the cavity axis is along the z-direction, the structure of the transverse mode is given by

$$\Psi_{m,n}(x, y, z) = \sqrt{\frac{w_0}{w(z)}} H_m\left(\frac{\sqrt{2}y}{w(z)}\right) H_n\left(\frac{\sqrt{2}x}{w(z)}\right) \exp\left(-\frac{x^2 + y^2}{w^2}\right) \tag{2.22}$$

where w_0 is the waist minimum and $w(z)$ is the waist at distance z away from the minimum

$$w(z) = w_0 \sqrt{1 + \left(\frac{z}{z_R}\right)^2} \tag{2.23}$$

The Rayleigh Range, z_R, gives the distance that one must travel along the beam, from the minimum waist, for the area of the cross-section to be doubled

$$z_R = \frac{\pi w_0}{\lambda} \tag{2.24}$$

The first Hermite polynomial is given by $H_0 = 1$ and thus the TEM_{00} mode is given by

$$\Psi_{0,0}(x, y, z) = \sqrt{\frac{w_0}{w(z)}} \exp\left(-\frac{x^2 + y^2}{w^2}\right) \tag{2.25}$$

This mode is called the fundamental mode. It has a Gaussian profile and it is highly desirable since it provides the smallest waist and highest intensity at the center of the cavity. The profiles of the first twelve Hermite-Gaussian modes are shown in Figure 2.4.

The longitudinal field mode function is given by [76]

$$\Phi(x, y, z) = \sin\left(kz - (1 + n + m) arctan\left(\frac{z}{z_R}\right) + \frac{k(x^2 + y^2)}{2R(z)}\right) \tag{2.26}$$

with

$$R(z) = \left[1 + \left(\frac{z_R}{z}\right)^2\right] \tag{2.27}$$

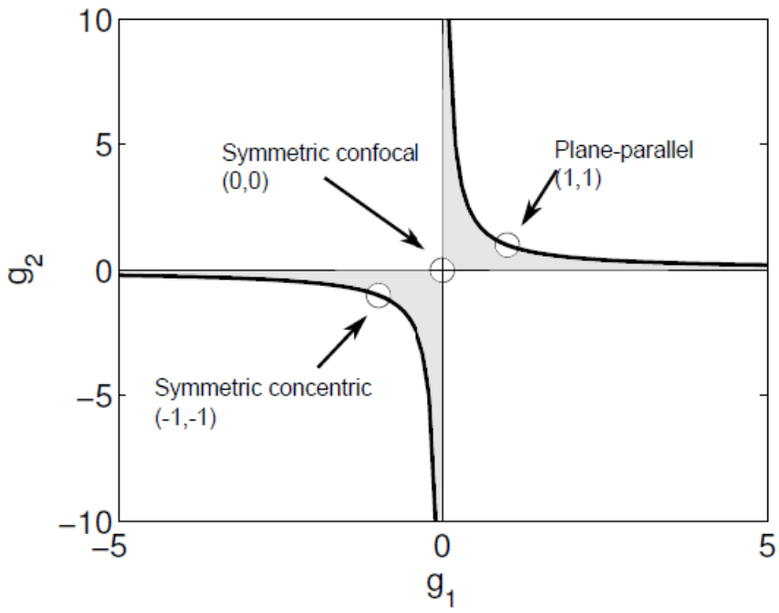

Figure 2.5: The cavity stability diagram with the position of three stable cavities [77].

$$k = \frac{2\pi}{\lambda} \tag{2.28}$$

where k is the wavenumber and $R(z)$ is the radius of curvature of the wavefront.

In equation 2.26, the second term represents the phase difference relative to a plane wave with wavevector k travelling along the z-axis. The resonance condition for a stable cavity states that, this difference in phase for a light field after a round trip of the cavity must be an integer multiple of 2π. Therefore, the resonant frequencies of the modes are given by

$$\nu_{nmq} = \nu_{FSR}\left[q + \frac{1}{\pi}(1+n+m)\arccos\left(1-\frac{L}{R_i}\right)\right] \tag{2.29}$$

where n, m are the transverse mode indices, q the longitudinal mode index and ν_{FSR} the free spectral range frequency.

2.2.1 Cavity Stability

The stability of the cavity depends on the ratio of the length of the cavity, L, to the radii of curvature of the two mirrors, R_1 and R_2. Depending on this ratio, optical cavities are classified in different types. Some of the most important ones include confocal symmetric cavities ($R_1 = R_2 = L$), plane-parallel cavities ($R_1 = R_2 = \infty$), concentric cavities ($L = R_1 + R_2$) etc.

Using ray transfer matrices to analyse the path light takes through a cavity, and imposing the condition that the beam must be the same shape after a round-trip through the cavity, the cavity stability condition is given by [78]

$$0 < \left(1-\frac{L}{R_1}\right)\left(1-\frac{L}{R_2}\right) < 1 \tag{2.30}$$

We can define the cavity stability parameters as

$$g_1 = 1 - \frac{L}{R_1} \tag{2.31}$$

$$g_2 = 1 - \frac{L}{R_2} \tag{2.32}$$

and the stability condition becomes

$$0 < g_1 g_2 < 1 \tag{2.33}$$

Figure 2.5 shows the stability diagram along with the position of three stable cavities. If a cavity lies within the shaded area in Fig. 2.5 then it is stable. If a cavity lies on the borders of a stability region, it is less robust than one that lies further inside. This is because changes in temperature or external vibrations can change the length and alignment of the cavity, thus changing the stability parameters (g_1 and g_2) and the cavity no longer lies within the stability region.

2.2.2 Finesse

When a photon enters the optical cavity it reflects off the mirrors, then bounces between them a number of times, until it decays in free space or is absorbed by the mirror substrate. This process is characterised by a value called Finesse(F). This is defined as the free spectral range divided by the full-width at half-maximum of the cavity resonances, $\delta\nu$,

$$F = \frac{FSR}{\delta\nu} \tag{2.34}$$

The cavity decay rate, κ, is expressed in terms of $\delta\nu$ as

$$\kappa = \frac{2\pi\delta\nu}{2} \tag{2.35}$$

and the finesse is now expressed in terms of cavity decay rate

$$F = \frac{\pi FSR}{\kappa} \tag{2.36}$$

The finesse depends entirely on the losses of the cavity and therefore it can be expressed as

$$F = \frac{2\pi}{L_{total}} \tag{2.37}$$

whereas L_{total} are the losses from transmission out of the cavity, scattering out of the cavity mode, and absorptive losses at the mirror interface. Finally, combining the previous equations, the cavity decay rate can be expressed as

$$\kappa = \frac{\pi}{F} = \frac{L_{total}}{2} \tag{2.38}$$

2.3 Atom-Light Interactions

In this section I present the basic theory of atom-light interactions. I will start with the simple 2-level case of the Jaynes-Cummings model, where we examine the case with and without losses. Since our system uses a calcium ion with an internal state structure similar to a Λ system, I will give the expression of the Jaynes-Cummings model for a three-level Λ system. In the presence of an external magnetic field the energy levels split due to the Zeeman effect. In our case, the 3-level model changes to an 8-level model, where the transitions between the sublevels can only be addressed by the appropriate polarised light. Finally, I will give an overview of how we use this model in our simulations, that we have used throughout our experiments and publications. It has to be noted that the following derivations were taken from [73] and [79].

2.3.1 Two-level System

We consider a system where a two level atom is coupled to a single quantised mode of an optical cavity field. The atom has a ground state $|g\rangle$ and an excited state $|e\rangle$. The optical cavity is a harmonic oscillator with Fock states given by $|n\rangle$ $(n = 0, 1, ...)$. The Hamiltonian of this system is the sum of the individual Hamiltonians of the two sub-systems, the optical cavity and the atom, as well as their interaction.

$$\hat{H} = \hat{H}_{cav} + \hat{H}_{at} + \hat{H}_{int} \tag{2.39}$$

The Hamiltonian of the quantised field of the cavity is given by

$$\hat{H}_{cav} = \hbar\omega\left(\hat{a}^\dagger\hat{a} + \frac{1}{2}\right) \tag{2.40}$$

where h is the Plank constant, ω is the frequency of the cavity and $\hat{a}^\dagger$ and $\hat{a}$ are the photon creation and annihilation operators respectively. The Hamiltonian of the atom is given by

$$\hat{H}_{at} = \sum_{i=g,e} E_i\hat{\sigma}_{ii} \tag{2.41}$$

where E_i is the eigenvalue of the state $|i\rangle$ and $\hat{\sigma}_{ii} = |i\rangle\langle i|$. The atom-cavity interaction is described by the Jaynes-Cummings interaction Hamiltonian, which in the rotating wave approximation is given by

$$\hat{H}_{int} = \hbar g(r, z)(\hat{a}\hat{\sigma}_{ge} + \hat{a}^\dagger\hat{\sigma}_{eg}) \tag{2.42}$$

where $\hat{a}$ $(\hat{a}^\dagger)$ is the photon annihilation (creation) operator and $\hat{\sigma}_{ge} = |g\rangle\langle e|$ $(\hat{\sigma}_{eg} = |e\rangle\langle g|)$ is the atomic energy level raising (lowering) operator. $g(r, z)$ is the position dependent ion-cavity coupling, and for a TEM_{00} mode of waist $w(z = 0)$ is given by

$$g(r, z) = g_0\frac{w(0)}{w(z)}\sin(kz)e^{-(r/w(z))^2} \tag{2.43}$$

where $w(z)$ is the waist of the cavity and k the field wave number. The maximum coupling, g_0, can be expressed as

$$g_0 = \sqrt{\frac{3\lambda^2 c\gamma}{3\pi V}} \tag{2.44}$$

where λ is the wavelength of the transition in the two level atom, γ is the spontaneous decay rate and V the volume of the cavity mode given by

$$V = \frac{\pi L w(0)^2}{4} \tag{2.45}$$

where L is the length of the cavity.

The eigenstates (dressed states) $|\pm, n\rangle$ and eigenvalues $\epsilon_n^\pm$ of the Jaynes-Cummings Hamiltonian are given by [73]

$$|+, n\rangle = \cos\theta_n|e, n-1\rangle + \sin\theta_n|g, n\rangle \tag{2.46}$$

$$|-, n\rangle = -\sin\theta_n|e, n-1\rangle + \cos\theta_n|g, n\rangle \tag{2.47}$$

$$\epsilon_n^\pm = \bar{\epsilon}_n \pm \frac{\Delta\epsilon_n}{2} \tag{2.48}$$

$$\bar{\epsilon}_n = n\hbar\omega \tag{2.49}$$

$$\Delta\epsilon_n = \hbar\sqrt{4ng^2 + \delta^2} \tag{2.50}$$

where δ is the detuning from the atomic transition frequency, $\delta = \omega - \omega_0$. θ_n is called the mixing angle and is given by

$$\tan(2\theta_n) = 2\frac{g\sqrt{n}}{\delta} \tag{2.51}$$

Up to this point no loss channels have been included in our system. To include the spontaneous decay of the atom and the cavity decay, we use the master equation approach [79]. The equation of motion for the density operator is called the master equation and is given by

$$\frac{\partial\hat{\rho}}{\partial t} = -\frac{i}{\hbar}[\hat{\rho}, \hat{H}_{JC}] + \mathcal{L}(\hat{\rho}) \tag{2.52}$$

$\mathcal{L}$ is called the Liouvillian and describes the losses of the system.

$$\mathcal{L}(\hat{\rho}) = -\frac{1}{2}\left(\left\{\hat{\rho}, \hat{C}_a^\dagger\hat{C}_a\right\} + \left\{\hat{\rho}, \hat{C}_{\sigma_{ge}}\hat{C}_{\sigma_{eg}}\right\}\right) + \hat{C}_a\hat{\rho}\hat{C}_a^\dagger + \hat{C}_{\sigma_{eg}}\hat{\rho}\hat{C}_{\sigma_{ge}} \tag{2.53}$$

$\hat{C}_a = \sqrt{2\kappa}\hat{a}$ is the collapse operator of the cavity and $\hat{C}_{\sigma_{ge}} = \sqrt{2\gamma}\hat{\sigma}_{ge}$, $\hat{C}_{\sigma_{eg}} = \sqrt{2\gamma}\hat{\sigma}_{eg}$ are the collapse operators of a two-level atom. In addition, the master equation can be expressed in terms of an effective Hamiltonian, where the effective Hamiltonian is the Jaynes-Cummings Hamiltonian added with a Hamiltonian that describes the losses in our system.

$$\frac{\partial\hat{\rho}}{\partial t} = -\frac{i}{\hbar}(\hat{H}_{eff}\hat{\rho} - \hat{\rho}\hat{H}_{eff}^\dagger) + 2\kappa\hat{a}\hat{\rho}\hat{a}^\dagger + 2\gamma\hat{\sigma}_{eg}\hat{\rho}\hat{\sigma}_{ge} \tag{2.54}$$

$$\hat{H}_{eff} = \hat{H}_{JC} + \hat{H}_{loss} \tag{2.55}$$

$$\hat{H}_{loss} = -\frac{i\hbar}{2}(2\gamma\hat{\sigma}_{ge}\hat{\sigma}_{eg} + 2\kappa\hat{a}^\dagger\hat{a}) \tag{2.56}$$

The general solution of the system is given by the state [73]

$$|\psi(t)\rangle = A(t)e^{-i\delta/2}|g,1\rangle + B(t)e^{i\delta/2}|e,0\rangle \tag{2.57}$$

where $A(t)$ and $B(t)$ are the probability amplitudes.

2.3.2 Three-level Λ-system

Now we consider the case of a three-level system interacting with an optical cavity. The three level system is a better approximation to the energy structure of the calcium ion that we are using in our experiment. The line structure of calcium in a weak magnetic field resembles that of a Λ-system. The system is comprised of 3 states $|S\rangle \leftrightarrow S_{1/2}$, $|P\rangle \leftrightarrow P_{1/2}$ and $|D\rangle \leftrightarrow D_{3/2}$. The cavity is tuned across the $P \leftrightarrow D$ transition, while a pump beam transfers the population from the S-state to the P-state, Figure 2.6.

In this system the Hamiltonian is given by

$$\hat{H} = \hat{H}_{ion} + \hat{H}_{cav} + \hat{H}_{int} + \hat{H}_{pump} \tag{2.58}$$

The Hamiltonians for the cavity and the interaction remain the same as the two-level model as nothing has changed in that respect.

$$\hat{H}_{cav} = \hbar\omega\left(\hat{a}^\dagger\hat{a} + \frac{1}{2}\right) \tag{2.59}$$

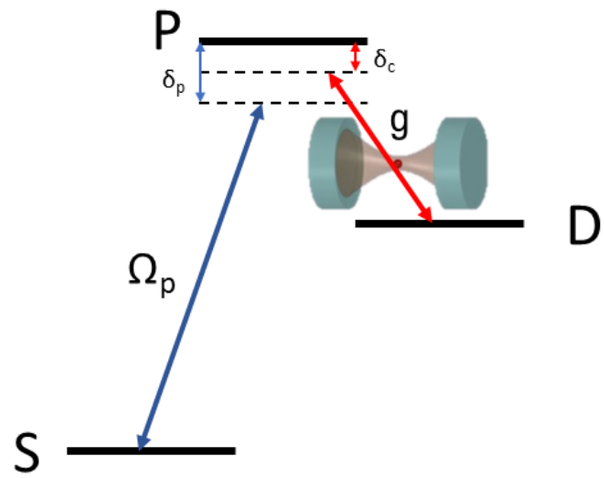

Figure 2.6: A Λ system like the one in the calcium ion. The cavity is tuned across the $P \leftrightarrow D$ transition and is detuned by δ_c. There is a pump laser to transfer the population from the S-state to the P-state which is detuned by δ_p and has a Rabi frequency Ω_P

$$\hat{H}_{int} = \hbar g(r,z)(\hat{a}\hat{\sigma}_{PD} + \hat{a}^{\dagger}\hat{\sigma}_{DP}) \tag{2.60}$$

where $\hat{\sigma}_{mn} = |m\rangle\langle n|$ for $m, n \in \{S, P, D\}$. On the other hand, the Hamiltonian of the ion now includes the extra energy state.

$$\hat{H}_{ion} = \sum_{i=S,P,D} E_i \hat{\sigma}_{ii} \tag{2.61}$$

In addition, there is a pump laser so we have to include the interaction of the pump field with the ion.

$$\hat{H}_{pump} = \frac{\hbar\Omega_p}{2}(e^{-i\omega_p t}\hat{\sigma}_{PS} + e^{i\omega_p t}\hat{\sigma}_{SP}) \tag{2.62}$$

where ω_p is the angular frequency of the pump field and Ω_p its Rabi frequency.

To include the losses of the system, we must solve the master equation for the Λ system. Having added one more state to our system, this means that the atomic decay now must include this extra loss channel as well. The atomic decay includes the decay from P to D (γ_{PD}) as well as P to S (γ_{PS}) giving as a total decay rate of $\gamma = \gamma_{PS} + \gamma_{PD}$. Therefore the loss channels are described by

$$\mathcal{L}(\hat{\rho}) = -\frac{1}{2}\Big(\{\hat{\rho}, \hat{C}_a^{\dagger}\hat{C}_a\} + \sum_{j=S,D}\{\hat{\rho}, \hat{C}_{\sigma_{Pj}}\hat{C}_{\sigma_{jP}}\}\Big) + \hat{C}_a\hat{\rho}\hat{C}_a^{\dagger} + \sum_{j=S,D}\hat{C}_{\sigma_{Pj}}\hat{\rho}\hat{C}_{\sigma_{jP}} \tag{2.63}$$

whereas

$$\hat{C}_a = \sqrt{\kappa}\hat{a} \tag{2.64}$$

$$\hat{C}_{\sigma_{Pj}} = (\gamma_{Pj}\hat{\sigma}_{Pj})^{\frac{1}{2}} \tag{2.65}$$

$$\hat{C}_{\sigma_{jP}} = (\gamma_{Pj}\hat{\sigma}_{jP})^{\frac{1}{2}} \tag{2.66}$$

In order to evaluate the master equation 2.52, we need to redefine the Hamiltonian to include the losses of the system.

$$\hat{H}'_{JC} = \hbar\Big[\delta_p\hat{\sigma}_{SS} + \delta_c\hat{\sigma}_{DD} + (\delta_c - \delta_p)\hat{a}^{\dagger}\hat{a} + \frac{\Omega_p}{2}(\hat{\sigma}_{PS} + \hat{\sigma}_{SP}) + g(\hat{\sigma}_{PD}\hat{a} + \hat{\sigma}_{DP}\hat{a}^{\dagger})\Big] \tag{2.67}$$

where δ_p is the detuning of the pump and δ_c is the detuning of the cavity. Substituting the Liouvillian 2.63 and the Jaynes-Cummings Hamiltonian 2.67 into the master equation 2.52 we can solve it numerically.

However, there are additional effects from the presence of an external magnetic field that were not included in this three-level model. For this case, we need to consider the 8-level model of the system.

2.3.3 8-level System

When an atom is placed in a magnetic field, it interacts with it and splits its energy levels due to the Zeeman effect. In addition, transitions between the energy sub-levels can be only be addressed by the appropriate polarised light.

A magnetic field, B, lifts the degeneracy of the energy level $^{2S+1}L_J$ to sub-levels $m_J = -J, -J+1...., J$. The energy splitting between the sub-levels is given

$$\Delta E_{J,m_J} = m_J g_J \mu_B B \tag{2.68}$$

where μ_B is the Bohr magnetron and g_J the Landé factor

$$g_J = 1 + \frac{J(J+J) - L(L+1) + S(S+1)}{2J(J+1)} \tag{2.69}$$

where J is the total angular momentum, L the total orbital angular momentum and S the total spin angular momentum.

In our system the calcium ion splits from 3 levels to 8 levels under the Zeeman effect. The $S_{1/2}$ level splits to 2 levels, $P_{1/2}$ to 2 levels and $D_{3/2}$ to 4 levels

$$|S\rangle \rightarrow |S,-1/2\rangle, |S,1/2\rangle$$
$$|P\rangle \rightarrow |P,-1/2\rangle, |P,1/2\rangle$$
$$|D\rangle \rightarrow |D,-3/2\rangle, |D,-1/2\rangle, |D,1/2\rangle, |D,3/2\rangle$$

The Landé factor for each level is $g_S = 2$, $g_P = 2/3$ and $g_D = 4/5$. Figure 2.7 shows the Zeeman sub-levels.

Using the 8-level model, we define again the Hamiltonian 2.58 to include the effect of the Zeeman sub-levels. The Hamiltonian of the ion must now include the contributions for each individual sub-level

$$\hat{H}_{ion} = \hat{H}_S + \hat{H}_P + \hat{H}_D \tag{2.70}$$

$$\hat{H}_S = \sum_{m_S} (\hbar\delta_p + m_S g_S \mu_B) \hat{\sigma}_{Sm_S,Sm_S}$$
$$\hat{H}_P = \sum_{m_P} m_P g_P \mu_B \hat{\sigma}_{Pm_P,Pm_P}$$
$$\hat{H}_D = \sum_{m_D} (\hbar\delta_c + m_D g_D \mu_B) \hat{\sigma}_{Dm_D,Dm_D}$$

where $\hat{\sigma}_{Km_K,Lm_L} = |K,m_K\rangle \langle L,m_L|$ is the projection operator including the Zeeman sub-levels.

The splitting of the levels, due to effect of the external magnetic field, affects the way the pump beam interacts with the ion. The strength of the allowed transitions between

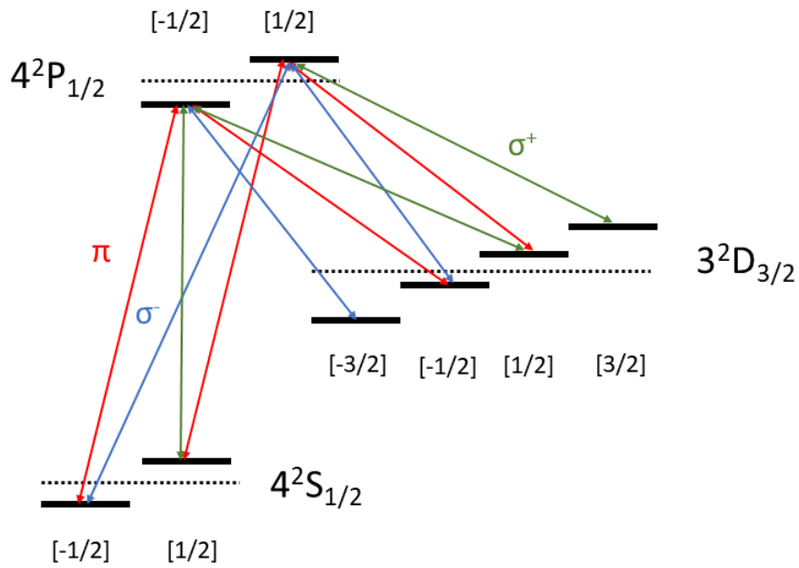

Figure 2.7: Zeeman sub-levels of our model with the appropriate polarisation of the transitions.

the sub-levels depend on the polarisation of the beam. The polarisation vectors given by $\vec{\boldsymbol{\epsilon}}_{\pm} = (\hat{\mathbf{x}} \pm i\hat{\mathbf{y}})/\sqrt{2}$ and $\vec{\boldsymbol{\epsilon}}_0 = \hat{\mathbf{z}}$ for circular polarisation ($\sigma^{\pm}$ transition) and linear polarisation (π transition) respectively. In addition, due to the Zeeman effect, the transition probability between the sub-levels is modulated by the Clebsch-Gordon coefficient C^{K,m_K}_{L,m_L} for the $|K, m_K\rangle \leftrightarrow |L, m_L\rangle$ transition. Now the pump Hamiltonian is given by

$$\hat{H}_{pump} = \frac{\hbar}{2} \sum_{m_S} \sum_{m_P} \left(\vec{\boldsymbol{\epsilon}}_p \cdot d^{Pm_P}_{Sm_S} \hat{\sigma}_{P,m_P;S,m_S} + \vec{\boldsymbol{\epsilon}}_p \cdot d^{Sm_S}_{Pm_P} \hat{\sigma}_{S,m_S;P,m_P} \right) \tag{2.71}$$

where $\vec{\boldsymbol{\epsilon}}_p$ is the polarisation vector of the pump field. The vectors decompose in terms of the Clebsch-Gordon coefficients

$$\begin{aligned} d^{Km_K}_{Lm_L} &= C^{K,m_K}_{L,m_L} \cdot \vec{\boldsymbol{\epsilon}}_+ \quad if \;\; m_K - m_L = 1 \\ d^{Km_K}_{Lm_L} &= C^{K,m_K}_{L,m_L} \cdot \vec{\boldsymbol{\epsilon}}_0 \quad if \;\; m_K - m_L = 0 \\ d^{Km_K}_{Lm_L} &= C^{K,m_K}_{L,m_L} \cdot \vec{\boldsymbol{\epsilon}}_- \quad if \;\; m_K - m_L = -1 \\ d^{Km_K}_{Lm_L} &= 0 \quad otherwise \end{aligned}$$

The external magnetic field does not affect the cavity Hamiltonian, but it does affect the interaction Hamiltonian since the cavity is tuned across the P↔D transition. The interaction Hamiltonian is given by

$$\begin{aligned} \hat{H}_{int} = \hbar g \sum_{m_D} \sum_{m_P} \left(\vec{\boldsymbol{\epsilon}}_a \cdot d^{Pm_P}_{Dm_D} \hat{\sigma}_{P,m_P;D,m_D} \hat{a} + \vec{\boldsymbol{\epsilon}}_a \cdot d^{Dm_D}_{Pm_P} \hat{\sigma}_{D,m_D;P,m_P} \hat{a}^{\dagger} \right) \\ + \hbar g \sum_{m_D} \sum_{m_P} \left(\vec{\boldsymbol{\epsilon}}_b \cdot d^{Pm_P}_{Dm_D} \hat{\sigma}_{P,m_P;D,m_D} \hat{b} + \vec{\boldsymbol{\epsilon}}_b \cdot d^{Dm_D}_{Pm_P} \hat{\sigma}_{D,m_D;P,m_P} \hat{b}^{\dagger} \right) \end{aligned} \tag{2.72}$$

where $(\hat{a}, \hat{b})$ and $(\hat{a}^{\dagger}, \hat{b}^{\dagger})$ are the annihilation and creation operators of the cavity with polarization $\vec{\boldsymbol{\epsilon}}_a$ and $\vec{\boldsymbol{\epsilon}}_b$.

Finally, when the losses of the system are considered we need to adjust the Liouvillian to incorporate the effect of the external magnetic field. The cavity does not change from this, so its collapse operator remains unaltered. On the other hand, the decay operator of the atom

changes according to the Clebsch-Gordon coefficients.

$$\gamma_{KL} \rightarrow \left|C_{L,m_L}^{K,m_K}\right|\gamma_{KL} \tag{2.73}$$

Therefore, the collapse operators for the ion in the 8-level system are redefined for the $|P\rangle \leftrightarrow |S\rangle$ transition as

$$\hat{C}_{S\sigma}^{\pm} = \sum_{m=\pm 1/2} \sqrt{2\left|C_{S,m}^{P,-m}\right|\gamma_{PS}}\hat{\sigma}_{S,m;P,-m} \ , \qquad \sigma^{\pm} \text{ transition} \tag{2.74}$$

$$\hat{C}_{S\sigma}^{0} = \sum_{m=\pm 1/2} \sqrt{2\left|C_{S,m}^{P,m}\right|\gamma_{PS}}\hat{\sigma}_{S,m;P,m} \ , \qquad \pi \text{ transition} \tag{2.75}$$

and for the $|P\rangle \leftrightarrow |D\rangle$ transition as

$$\hat{C}_{D\sigma}^{\pm} = \sum_{m=\pm 1/2} \sqrt{2\left|C_{D,m\pm 1}^{P,m}\right|\gamma_{PD}}\hat{\sigma}_{D,m\pm 1;P,m} \ , \qquad \sigma^{\pm} \text{ transition} \tag{2.76}$$

$$\hat{C}_{D\sigma}^{0} = \sum_{m=\pm 1/2} \sqrt{2\left|C_{D,m}^{P,m}\right|\gamma_{PD}}\hat{\sigma}_{D,m;P,m} \ , \qquad \pi \text{ transition} \tag{2.77}$$

Thus, the loss channels are described by

$$\mathcal{L}(\hat{\rho}) = -\frac{1}{2}\Big(\{\hat{\rho}, \hat{C}_a^{\dagger}\hat{C}_a\} + \sum_{\substack{j=S,D \\ p=\pm,0}} \{\hat{\rho}, \hat{C}_{j\sigma}^{p}(\hat{C}_{j\sigma}^{p})^{\dagger}\}\Big) + \hat{C}_a\hat{\rho}\hat{C}_a^{\dagger} + \sum_{\substack{j=S,D \\ p=\pm,0}} \hat{C}_{j\sigma}^{p}\hat{\rho}(\hat{C}_{j\sigma}^{p})^{\dagger} \tag{2.78}$$

2.4 Simulation

Using the above 8-level model we can simulate the behaviour of our system and extract useful information to compare with the experimental data that was obtained. The simulations were performed using Matlab and the Quantum Toolbox [80].

In most cases, which will be presented in the following publications, to see the full features of our system, we use the Zeeman model with a two mode cavity (the cavity in the experiment supports both σ^+ and σ^- polarisations). In addition, we also incorporate a pulsed probing beam with a realistic pulse shape. Using the Quantum Optics toolbox we set all the states for all the Zeeman sub-levels, the annihilation and creation operators for our cavity and ion, polarisations and other parameters. We then define the Hamiltonian in the simulation following the theory explained above, as well as the Liouvillian with the collapse operators. Using a routine called solvemc, we can solve the master equation and obtain the density matrix. Then, using the density matrix, we can obtain the single photons emitted in our cavity as well as the state population.

One example of how we use this routine is to calculate the number of single photons as we vary the detuning of the cavity, which is a free parameter in the simulation. In this case, we input the settings used in the experiment (pump Rabi frequency, g_0 etc) and run the simulation over the cavity detuning range we desire.

This is just one example of the basic tools we used to examine the experimental data and compare with the theory. The simulation is a strong tool that we use in our experiments and depending on the needs, we modify it to reflect the different parameters

of each experiment. More information on the specific simulations used in each experiment will follow in the next chapters.

Chapter 3

Precise positioning of an ion in an integrated Paul trap-cavity system using radiofrequency signals

Our system was designed as a successor of a previous design in our group [74] and modified accordingly to include FFPCs. The publication included in this chapter "Precise positioning of an ion in an integrated Paul trap-cavity system using radiofrequency signals" [64], gives an overview of the design and architecture of the ion trap-cavity hybrid system, as well as detailed description on how the ion's position was optimised to the centre of the cavity, in order to optimise the coupling of the ion to the cavity mode.

During the time of this publication there were mainly two competing systems that were trying to incorporate FFPC's to ion traps [61] [62]. Therefore, the aim of this system was to perform better than the other competing systems, achieve better localisation of the ion, and be the first one to achieve strong coupling of a single ion to an optical cavity. The first thing we had to address, after showing we can trap a well localised ion and couple it to the optical cavity, was to find a way to move the ion relative to the cavity mode in order to maximise the coupling.

The system consists of a 3-D Paul trap with an integrated FFPC. There are two vertical electrodes (outer electrodes) where the main RF is applied, while two radial electrodes are held at RF ground. In addition, two vertical electrodes (inner electrodes) are placed concentrically inside the main electrodes and are held at RF ground as well. For micromotion compensation, DC voltages are applied to two additional perpendicular electrodes, as well as the inner electrodes. Using a PMT to detect the fluorescence from the ion, the RF correlation technique is used to compensate micromotion [73].

The fibres, that form the cavity, are shielded inside the inner electrodes so the dielectric coating does not interact with the trapping field. The length of the cavity when stabilised, is resonant with the 866 nm transition in the ion. Using a stabilising laser (897 nm), and the Pound-Drever-Hall technique, the cavity is locked with a standard deviation lower than 500 kHz.

In the past, there have been other systems where the cavity was the one that was mechanically translated to overlap with the ion. This technique requires translation systems that are in general bulky. In addition, the translation of the cavity affects the trapping field and shifts the geometrical centre of the trap. The main reason though that we have avoided this in our system, was that it hinders the tight integration of the cavity into the electrodes. Therefore, in our system we chose to move the pseudopotential minimum of the trap. A small RF field, with the same frequency as the trapping field, is applied to the the two radial electrodes that were previously held at RF ground. This will allow us to move the ion in the radial plane relative to the cavity field.

To get the optimal coupling of the ion to the cavity, first the ion must be placed on an antinode of the cavity mode. In order to achieve that, RF signals are applied to the axial inner electrodes and by varying their amplitude, the standing wave structure of the cavity mode was mapped. Then by adjusting the RF signal the ion is placed on an antinode.

While the ion is moved radially, we make sure that the Rf signal applied to the radial electrodes is in-phase with the main RF so there is no additional micromotion [81]. An efficient way to measure the strength of the ion-cavity coupling while we move the ion radially, is to measure the cavity emission spectrum as the cavity is scanned across the Raman resonance at different positions. The spectral area under the curve for this Raman scan is proportional to the coupling of the ion to the cavity. Using this method and using an Electron Multiplying CCD camera (EMCCD) to record the position of the ion, we have located the centre of the cavity mode at $(3.9 \pm 0.1, 6.4 \pm 0.3)\ \mu m$ in the x and y directions respectively from the ion's original position. The value stated for the x direction in this publication is slightly different from the one mentioned in the next publication in Chapter 4. The reason for this is a small error in the calibration of the EMCCD when measuring the distance in this publication, that we discovered later.

During this experiment I worked on setting up the peripheral systems of the trap, including, but not limited, to the lasers used for cooling and probing, redesigning the electronics for the feedback to the cavity and the biquad filter to improve the lock quality. I contributed towards the measurements to optimise the position of the ion to the cavity, as well as the analysis of the experimental data. For the composition of the publication I assisted with the writing and the production of figures.

JOURNAL OF MODERN OPTICS, 2018
VOL. 65, NOS. 5–6, 520–528
https://doi.org/10.1080/09500340.2017.1406158

Taylor & Francis
Taylor & Francis Group

Precise positioning of an ion in an integrated Paul trap-cavity system using radiofrequency signals

Ezra Kassa, Hiroki Takahashi, Costas Christoforou and Matthias Keller

Department of Physics and Astronomy, University of Sussex, Brighton, UK

ABSTRACT

We report a novel miniature Paul ion trap design with an integrated optical fibre cavity which can serve as a building block for a fibre-linked quantum network. In such cavity quantum electrodynamic set-ups, the optimal coupling of the ions to the cavity mode is of vital importance and this is achieved by moving the ion relative to the cavity mode. The trap presented herein features an endcap-style design complemented with extra electrodes on which additional radiofrequency voltages are applied to fully control the pseudopotential minimum in three dimensions. This method lifts the need to use three-dimensional translation stages for moving the fibre cavity with respect to the ion and achieves high integrability, mechanical rigidity and scalability. Not based on modifying the capacitive load of the trap, this method leads to precise control of the pseudopotential minimum allowing the ion to be moved with precisions limited only by the ion's position spread. We demonstrate this by coupling the ion to the fibre cavity and probing the cavity mode profile.

ARTICLE HISTORY
Received 31 July 2017
Accepted 2 November 2017

KEYWORDS
Ion trap; quantum optics; cavity quantum electrodynamics (QED); quantum internet; quantum networks

1. Introduction

The field of atomic physics has advanced greatly since the advent of ion traps which confine ions for unprecedented durations without utilising the internal states of the ions. Because ion traps offer unparalleled levels of control over the ions' mechanical and internal degrees of freedom, many experiments have sought to combine them with optical cavities for enhanced atom-light interactions. As a result, there have been a number of significant experiments: single photons were generated on demand (*1*), cavity sideband cooling was performed on single ions (*2*), super-radiance was observed with the collective coupling of coulomb crystals (*3*), tunable ion-photon entanglement has been demonstrated (*4*), multiple ions have been deterministically coupled to a cavity (*5*). The combination of ion traps with optical cavities is also considered to be one of the most promising avenues for advances in quantum information processing. Whilst there has been remarkable progress in the preparation, gate operation and readout of qubits (*6*, *7*), to date, these implementations have been limited to small scales, with 14 being the largest number of qubits entangled (*8*). Presently, challenges in the physical implementations of large quantum systems pose the greatest difficulty in advancing experimental quantum information science. Among the proposed solutions to tackle the scalability problem (e.g. (*9*–*12*)), distributed quantum information processing based on photonic links is the most promising. Notably, modular approaches using trapped ions as stationary qubits have attracted significant interest. However, so far, optically heralded entanglement with remote trapped ions has only been demonstrated using high numerical aperture lenses for the collection of photons, a method which suffers from low efficiencies in the entanglement generation(*13*, *14*). Placing the ions in an optical cavity, this efficiency can be greatly enhanced. Further, by reducing the cavity mode volume, one can enhance the ion-cavity coupling and, subsequently, the efficiency of operations. To this end, fiber-based Fabry-Pérot cavities (FFPCs) have been combined with ion traps (*15*–*17*). In such ion trap-cavity systems, the optimal positioning of the ion with respect to the cavity mode is of vital importance. In the previously demonstrated designs of ion traps combining FFPCs (*15*–*17*), the FFPCs were mechanically translated to optimise the overlap between the ion and the cavity mode. In addition to the need for a three-dimensional positioning system which tends to be bulky and expensive, the movable cavities affect the trapping field and shift the geometrical center of the trap as they are moved. This adds complexity to the trapping and optimisation of the ion-cavity coupling.

In contrast, in this paper, the tuning of the ion-cavity coupling is done by moving the ion electrically instead of moving the cavity.

CONTACT Ezra Kassa Ezra.Kassa@sussex.ac.uk

In this way, we minimise the number of the movable elements in our trap and realise a highly integrated system which facilitates mechanical rigidity, compactness and scalability without sacrificing the ability to reach optimal ion-cavity coupling. Recently this trap was successfully used to demonstrate the alteration of photon emission rates of a single trapped ion due to the Purcell effect (*18*).

Moving an ion in a Paul trap using a dc voltage is often not acceptable as it causes heating of the ion through excess micromotion. An approach based on the modification of the pseudopotential has been established in (*19*) by using tunable capacitive loads attached to the trap electrodes. The authors report a micrometer precision in their ability to shift the ion's position. However the drawbacks in this method are: (1) The secular frequency of the trap may be substantially lowered by the added capacitive load. (2) Care must be taken to minimise the phase shift on the rf signal caused by the capacitors which would otherwise lead to excess micromotion. (3) Manual tuning of bulk capacitors is difficult to repeat with precision.

In contrast to the techniques employed in (*19*), our trap architecture presented here does not require the addition of capacitors to shift the pseudopotential minimum. Instead, additional rf signals are directly applied to rf-electrodes integrated within the trap. The amplitudes and phases of the additional rf signals are digitally controlled by function generators, allowing for rapid, precise and repeatable tuning. As a result, we have been able to improve the positioning of the pseudopotential minimum down to the spread of the ion position.

This paper is organised as follows. In Section 2, we introduce the core trap design featuring extra electrodes used to move the ion electrically. We numerically simulate the ion's motion with respect to the cavity mode centre. In Section 3, we describe the trap infrastructure with a focus on the integrability and mechanical rigidity of the design which is attested by the measured stability of the FFPC. In Section 4, we present the experimental methods used to compensate excess micromotion due to the additional rf fields. We show the mapping of the cavity mode by displacing the ion. We conclude with a summary and outlook in Section 5.

2. Ion trap design

We have designed a novel radio-frequency (rf) Paul trap with an integrated FFPC. The trapping structure is an endcap-style ion trap (*20*, *21*). The trapping potential is formed by a pair of electrode assemblies each consisting of two concentric stainless steel tubes separated by a ceramic spacer (see Figure 1). The assembly is bonded together by an ultra-high vacuum compatible adhesive. The key design dimensions of components near the trapping region are detailed alongside the schematic in Figure 1. By applying an rf voltage on the outer electrodes whilst holding the inner electrodes at rf-ground, a trapping potential can be formed to trap a single ion at the centre of the design. The cavity fibres are inserted into the inner electrodes such that the resulting cavity mode encompasses the trapped ion. By recessing the fibres by 5–10 μm in the inner electrodes, the dielectrics are well shielded from the trapping electric field and do not distort the trapping potential as a result.

On the radial plane are four cylindrical electrodes placed 1.0 mm from the trap centre. By applying dc voltages to two adjacent electrodes as well as the inner electrodes, the excess micromotion due to stray static electric charges can be fully compensated in three dimensions (3D) using the rf-correlation technique (*22*). By applying rf signals synchronous to the main trap drive to the other two radial electrodes as well as the inner electrodes, the pseudopotential minimum position can be fully controlled in 3D, allowing the ion-cavity coupling to be optimised both radially and axially.

Figure 2 shows a simulation (*23*) of the trap pseudopotential when an rf voltage at a frequency of 20 MHz and amplitude 200 V is applied. In this simulation, all radial electrodes are held at rf-ground. One can see that the fibres are well-shielded from electric fields. The pseudopotential at the trap centre can be well approximated by the quadratic potential of an ideal Paul trap. Although, the radial electrodes break the cylindrical symmetry, they have negligible effect near the centre. From fits to the pseudopotentials at different rf voltage amplitudes (see Figure 2(b)), we find axial and radial secular frequencies of 7.3 kHz/V and 13.6 kHz/V respectively.

The FFPC is formed by two fibres (*24*) whose facets have radii of curvature of 560 μm and are coated for high reflectivity at 866 nm wavelength with 25 ppm transmission resulting in a finesse of 48,000. At the chosen cavity length of 370 μm, the cavity mode waist is calculated to be 8.5 μm. The fibre in the upper assembly is a single mode (SM) fibre and serves as the input. The second fibre is a multimode (MM) fibre and serves as the output as the cavity mode is most efficiently coupled into this fibre. The SM and MM fibres have a protective copper coating with thicknesses of 30 and 20 μm respectively. The FFPC fibres are carefully inserted and glued to the electrode assemblies ensuring the pair are concentric. However, due to imperfections in the insertion procedure and due to thermal drifts during the curing period, the axes of symmetry of the inner electrode and the fibre may deviate from one another by a few micrometers. Facet images of the inner electrodes with the inserted fibres (see Figure 3) reveal off-concentricities of $3 \pm 1\mu$m and $9 \pm 1\mu$m for the assemblies. As a result, we cannot expect the trapped

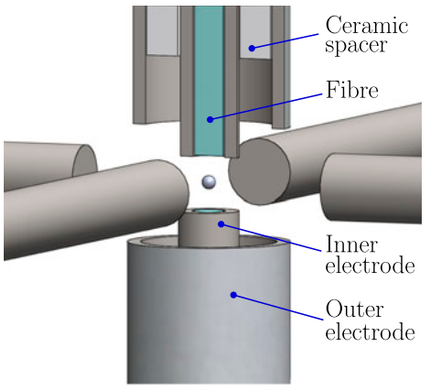

Key dimensions near the trapping region

	Diameter (μm)		Length (mm)
	Inner	Outer	
Inner electrode	300	465	6.0
Outer electrode	1000	1200	4.0
Ceramic spacer	500	950	3.0
Radial electrodes		500	16.0
Radial electrode to trap centre separation			1.0
Separation between inner electrodes			0.35
Fibre recess from inner electrodes			0.01
Outer electrode recess from inner electrodes			0.23

Figure 1. A drawing of the trapping region. A pair of electrode assemblies face one another in the axial direction, surrounded by four electrodes on the radial plane. Only a cross section of the upper assembly is shown to reveal the inner structure. The ion is symbolised by a small sphere in the centre. The main pseudopotential is generated by applying an rf voltage to the outer electrodes whilst the other electrodes are held at rf-ground.

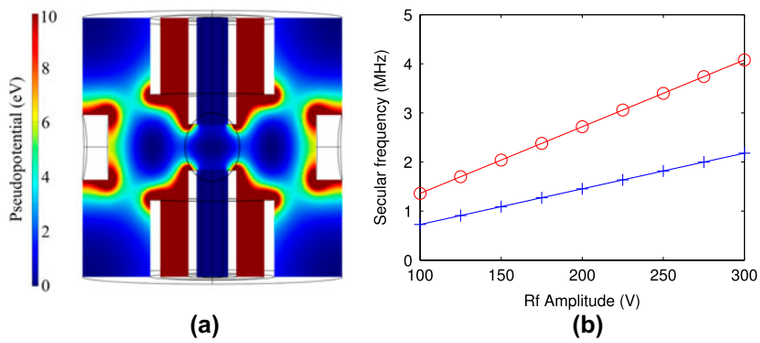

Figure 2. (a) The resulting pseudopotential when the applied field is alternating at 20MHz. The plotted pseudopotential is capped at 10 eV to emphasise its structure near the trapping region. (b) Secular frequencies for different drive amplitudes are simulated for the radial (red circles) and axial (blue crosses) directions and fitted (lines).

ion to optimally overlap with the cavity mode therefore highlighting the need for the radial electrodes on which rf voltages can be applied to shift the ion's radial position.

Figure 4(a) shows a cross section of the pseudopotential when an rf voltage of 200 V is applied to one of the radial electrodes. At a typical main drive amplitude of 200 V, we find that the ion can be shifted radially by more than 15μm. From the pseudopotential minimum positions, $y_{\min}$, at various rf amplitudes, V_y^{rf}, on the radial electrode (see Figure 4(b)), we find the pseudopotential minimum position can be fitted with the second order polynomial $y_{min} = (6.1 \times 10^{-5}\,\mu\mathrm{m}/V^2)V_y^{\mathrm{rf}2} - (0.1\mu\mathrm{m}/V)V_y^{\mathrm{rf}}$.

To precisely control the ion's position in the standing wave of the cavity mode, a differential rf voltage, $V_{z_u}^{\mathrm{rf}}$, can be applied on the inner electrodes in an anti-symmetric manner (i.e. $V_z^{\mathrm{rf}}/2$ on the upper electrode and $-V_z^{\mathrm{rf}}/2$ on the lower electrode). With simulations we find that we can move the ion by more than 2 μm (corresponding to more than two full wavelengths in the standing wave of the cavity more) with as little as 1 V of synchronous differential rf on the inner electrodes.

3. Trap infrastructure

Figure 5 shows a cross section of the design supporting the trap electrodes. The main rf signal is supplied to the outer electrodes via bored cylindrical stainless-steel mounts to which the electrode assemblies are secured using grub screws. The lower assembly is attached to a piezoelectric translational stage (*25*) for precise radial alignment with respect to the upper assembly. The radial alignment is done such that the cavity transmission signal is optimised. Electrical isolation for both electrode assemblies is provided by Macor platforms inserted between the bored stainless steel mounts and the rest of the supporting architecture. The inner electrodes are accessible through the Macor platforms and the bored openings for delivering electrical signals to them.

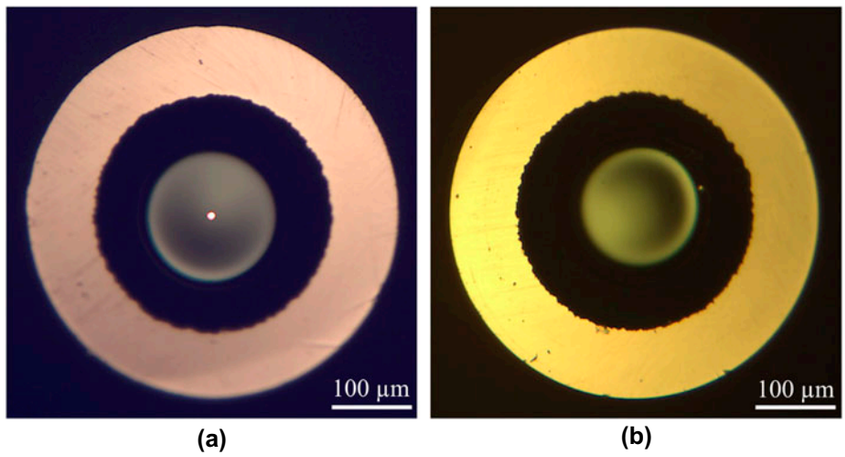

Figure 3. (a) A facet image of the SM fibre inside the upper inner electrode. The core of the fibre is illuminated by a laser beam injected into the fibre. (b) The MM fibre inside the inner electrode of the lower assembly.

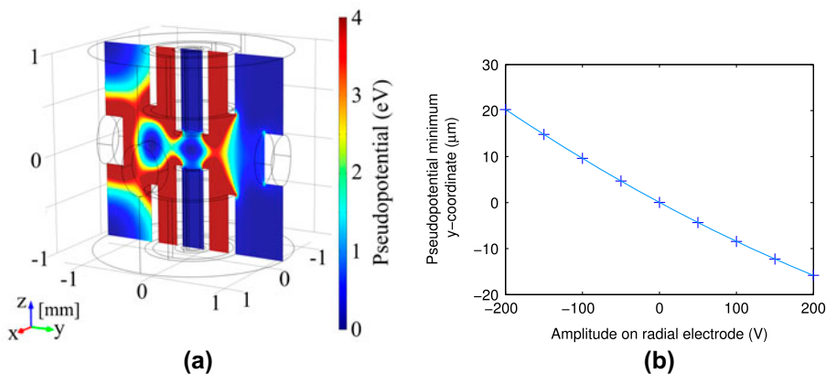

Figure 4. (a) The pseudopotential when an additional rf voltage of amplitude 200V synchronous to the main drive is applied to the radial electrode in the positive y-direction. (b) The pseudopotential minimum position vs. the rf-amplitude applied on the radial electrode. In dark blue crosses are the simulated data points. The light blue line is a second order polynomial fit.

Atop the Macor platform suspending the upper assembly are a pair of ring piezoelectric actuators used to scan and stabilise the cavity length. One is a multilayer piezo (*26*) with stroke 1.5 nm/V whilst the other is a monolayer piezo (*27*) with a stoke of 0.45 nm/V. The combination allows for versatile feedback to the cavity. The scanning and stabilisation of the cavity length is facilitated by a Viton ring (VACOM) (see inset of Figure 5) which compresses in response to change in pressure from the piezos. An additional Macor ring provides electrical isolation between the piezos. To aid the locking of the cavity length, the system is isolated from surrounding mechanical vibrations by placing it on a set of stainless steel stacks separated by Viton rubber parts which inhibit the propagation of mechanical vibrations (not shown in the figure). Furthermore, the fibres are clamped immediately outside the structure to provide strain relief.

A laser at 897 nm is used for stabilising the cavity length using the Pound-Drever Hall technique. The cavity linewidth with this laser is 22 MHz. For a stable cavity lock, the system should ideally have a flat response in gain and in phase for different feedback frequencies. This is however not the case in practice as the electrical as well as mechanical responses of system constituents (piezos, amplifiers, etc.) cause non-uniformity in the system's transfer function. As such, we first measured the transfer function of the system and found it to exhibit a derivative-like profile in gain accompanied by a sharp drop in phase at two distinct frequencies: 900 Hz and 9 kHz. This non-uniformity can be compensated by combining a low-pass filter, a band-pass filter and a high-pass filter. After introducing this custom filter, we are able to stably lock the cavity to the 897 nm laser to within a standard deviation of one thirteenth of the cavity linewidth. We find it is

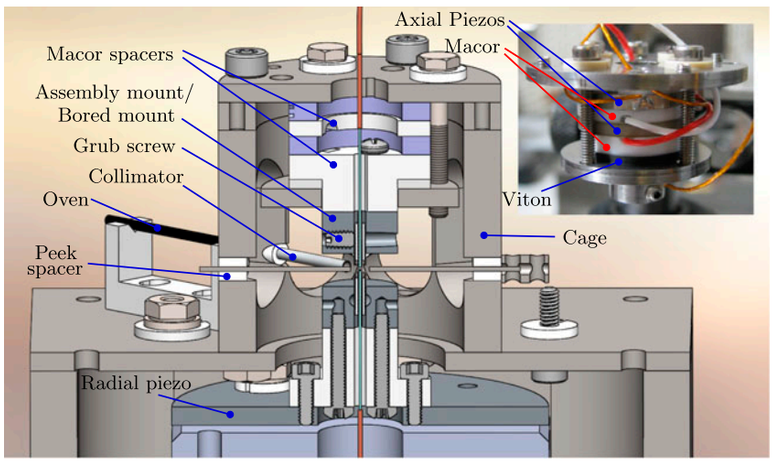

Figure 5. A cross-sectional view of the surrounding architecture. An atomic oven is placed outside the *cage* for thermal isolation. When resistively heated, an effusive beam is collimated by an electrode directing the atomic beam to pass between the electrode assemblies (where it gets ionised by lasers). Inset: A photograph of the upper assembly used in the experiment showing the stack of piezos. The upper(lower) piezo is the multilayer(monolayer) piezo. See main body for further discussion of the design.

sufficient to use the multilayer piezo alone to stabilise the cavity.

To trap ions, the oven is resistively heated expelling an effusive atomic beam which is collimated to propagate between the electrode assemblies. The atomic beam is ionised by ionisation lasers at the trap centre in the trapping region which is optically accessible via the eight windows of the cage.

This design has been demonstrated to trap ions for several hours in the presence of the FFPC. The cavity finesse of has not degraded over the course of 2 years.

4. Experiment

4.1. Set up

The ionic species used in this experiment is $^{40}Ca^{+}$. Figure 6(a) shows the relevant energy level scheme of the ion. The ion is Doppler cooled on the $S_{1/2} \leftrightarrow P_{1/2}$ transition. Repumper beams at 850 and 854 nm beams are used to depopulate the metastable $D_{3/2}$ and $D_{5/2}$ states respectively. Part of the ion's fluorescence is collected by a photomultiplier tube, the count rate of which is used to compensate excess micromotion using the rf-correlation technique as well as to perform spectroscopic measurements. The ion's fluorescence is also focused onto an Electron Multiplying CCD camera (EMCCD) by a set of objective lenses (OL) (Figure 6(b)). The EMCCD image is used to monitor the ion's position.

The fibre cavity is tuned to the $P_{1/2} \leftrightarrow D_{3/2}$ transition. The detection set up for the cavity emission is shown in Figure 6(b). An 897 nm beam is injected at the input of the single mode cavity fibre; the cavity transmission is used to stabilise the cavity length using the Pound-Drever Hall technique. The frequency of the 897 nm beam is finely tuned such that the cavity satisfies a double resonance condition for both the stabilising beam and the $P_{1/2} \leftrightarrow D_{3/2}$ transition at 866 nm. To separate the cavity emission signal at 866 nm from the stabilising beam (897 nm) a dichroic mirror and band pass optical filters are employed. The cavity emission at 866 nm is detected by a single photon counting module (SPCM) whilst the stabilising beam is transmitted toward a photo-detector (PD) whose signal is fed to the piezo-electric transducers (PZT) via feedback electronics to stabilise the cavity length.

The schematic in Figure 7 shows the electrical set-up of the system. For simplicity, we only show one radial electrode and the dc connections are not included. A helical resonator is used to amplify the main rf drive delivered to the outer electrodes of the upper electrode assembly (UEA) and the lower electrode assembly (LEA). Function generators FG2, FG3, FG4 and FG5, which are synchronised to FG1, independently apply rf signals to the radial rf electrodes and the inner electrodes of the LEA and UEA respectively. FG4 and FG5 are out of phase by 180°. The amplitudes and phases of the function generators are digitally controlled by a PC. The schemes and results are detailed in the following subsections.

4.2. Matching the phases of the additional rf signals

The additional rf signals need to be applied in-phase with the main rf drive at the trap. Otherwise they would cause

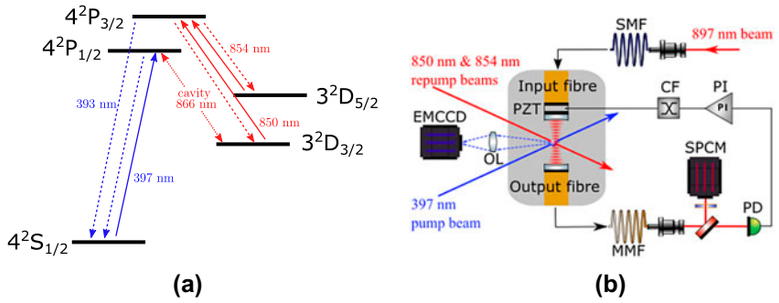

Figure 6. (a)The energy level scheme of $^{40}Ca^{+}$. The wavelengths are given alongside relevant transitions marked. The solid arrows show transitions where lasers are employed. The dashed arrows show the spontaneous decay transitions. The cavity is tuned to the $P_{1/2} \leftrightarrow D_{3/2}$ transition (dotted arrows). (b) A simplified schematic of the optical set up. An objective lens (OL) focuses the ion's fluorescence onto an Electron Multiplying CCD camera (EMCCD) used to monitor the ion's position. An 897 nm laser is injected into the input fibre cavity via the singe mode fibre (SMF). The multimode fibre (MMF) collects the cavity output. A dichroic mirror is used to filter the 866 nm photons from the stabilising 897 nm beam which is transmitted to a photodetector (PD). To stabilise the cavity length, the signal from the PD is fed back to the piezos (PZT) via a proportional and integral (PI) circuit and a custom filter (CM). A single photon counting module (SPCM) is employed to count the cavity's 866 nm photon emission.

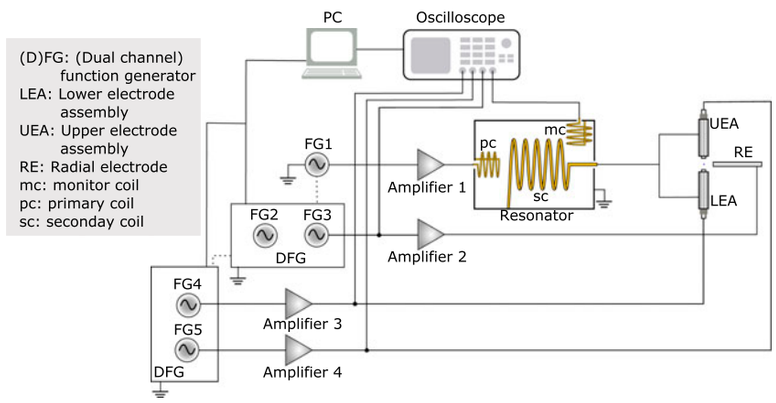

Figure 7. A simplified schematic of the electrical set up. Function Generator 1 (FG1) is used to drive the main electrodes via an amplifier (Amplifier 1) and a helical resonator. The phase at the output of the resonator can be gauged using the monitor coil (mc). The two channels of a dual function generator (DFG) are used to apply additional rf voltages to the two rf radial electrodes. Only one radial electrode (RE) is shown for simplicity. Another dual function generator is used to apply a differential rf signal to the inner electrodes of the electrode assemblies. An oscilloscope monitors the phase of the various signals. FG2, FG3, FG4 and FG5 are clock-synchronised to FG1. See the main text for further description.

the ion to have excess micromotion due to the phase mismatch (*22*). This means that the phase mismatch can be detected through the ion's micromotion, which allows an in situ optimisation of the phases regardless of various phase delays on the transmission lines. Having compensated the micromotion from stray dc fields, the excess micromotion caused by the phase mismatch, δ, of an additional rf field is described by (*22*)

$$\Delta z = -\frac{1}{4} qR\alpha\delta \sin \omega t, \tag{1}$$

when $\delta \ll 1$ and where q is the trap's q-parameter, R the ion-electrode distance, α the dipole moment of the trap and ω the drive frequency used. Therefore the induced micromotion is proportional to the mismatch δ and notably the polarity of the oscillation changes around $\delta = 0$. This can be clearly seen in Figure 8(a), where the micromotion amplitude is measured with the rf-correlation technique using the ion's UV fluorescence as the phase of FG3 is scanned.

The same procedure can be repeated for the other radial and axial directions. In the case of the axial direction, however, we use the ion's cavity emission signal instead of the free-space fluorescence because it has a greater sensitivity to the axial micromotion. In the presence of induced micromotion along the cavity axis, the ion's coupling strength to the cavity mode is modulated at the trap drive frequency (*28*) and so is the count rate of the cavity emission detected at the SPCM. In order

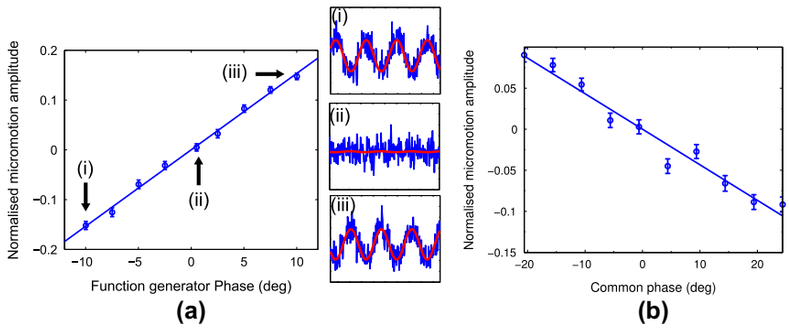

Figure 8. (a) Normalised micromotion amplitude as a function of the phase of FG3. The solid line is a linear fit to the data. Also shown in the right column are the correlated fluorescence counts at the individual points (i), (ii) and (iii). The micromotion amplitude is deduced by the sinusoidal fit at the trap frequency as shown in the red lines. The change of the polarity is clearly visible between (i) and (iii). (b) Normalised micromotion amplitude as a function of the common phase of FG4 and FG5, detected with the cavity emission counts at the SPCM. The error bars are the sinusoidal fitting errors of the correlated fluorescence counts.

to generate a continuous stream of photon emission, the cavity is locked to the 866 nm transition to satisfy a cavity-assisted Raman resonance condition while the ion is continuously cooled with the 397, 850 and 854 nm beams. The ion is placed at the position with the highest ion-cavity coupling gradient to maximise the sensitivity to micromotion. Figure 8(b) shows the micromotion amplitude as a function of the FG4 and FG5 common phase (i.e. the phases of FG4 and FG5 are changed whilst keeping the phase difference between them constant). The results in Figure 8(a) and (b) show that the phases of the additional rf signals can be unambiguously optimised with the crossing points at the zero amplitude, which ensures minimised micromotion in all three dimensions.

4.3. *Mapping the cavity mode*

Using the method discussed in the preceding subsection, the ion can be spatially displaced without inducing excess micromotion by changing the amplitudes of the additional rf signals. Furthermore, the spatial structure of the cavity mode can be probed with the change of the cavity emission counts as the ion is translated along one of the axes. This provides a means to identify the ion's position with respect to the centre of the cavity mode and optimise the coupling between the ion and cavity.

To probe the standing wave structure of the cavity mode, the differential rf voltages of FG4 and FG5 are varied to scan the ion's position along the axial direction (see Figure 7). The cavity emission is generated by the cavity-assisted Raman transition as described in the last section and monitored at the SPCM. The result is illustrated in Figure 9 which clearly shows a trace of cavity's standing wave, the periodicity of which corresponds to the spatial separation of half the wavelength of 866 nm. There is a

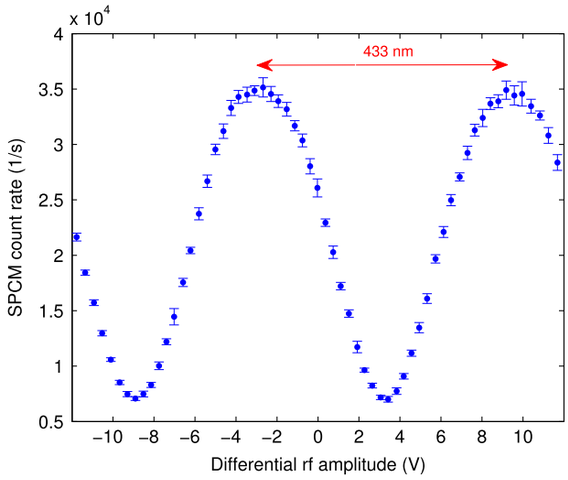

Figure 9. The cavity emission as the ion is being moved along the standing wave of the cavity mode. The *x*-axis is the differential voltage applied to the upper and lower inner electrodes as probed by the oscilloscope (see Figure 7 The error bars are standard deviations from 10 measurements. The separation of the two anti-nodes correspond to a spatial separation of 433 nm as indicated by the red arrow.

background contribution count rate of 4,200 counts from the stabilising beam. We compute a visibility of 83 ± 3%. From the data we can infer that the spatial resolution for the average position of the ion is better than 10 nm.

As in the case for the axial direction, the radial profile of the cavity mode can be similarly probed by scanning the amplitude of the rf signal applied to one of the radial electrodes. Due to the relatively large spatial structure of the cavity mode along the radial direction, we can gauge the physical dimension of the profile via the actual displacement of the ion's image on the EMCCD camera (Figure 6). Using the known distance between the UEA

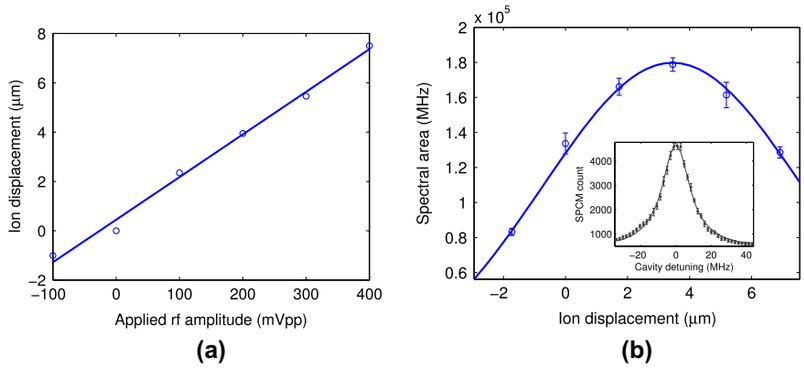

Figure 10. (a)The ion's displacement as a function of the rf voltage setting on Function Generator 3 (FG3). The data points are the relative positions of the ion obtained by fitting a Gaussian function to the EMCCD image data. The fitting errors are small for representation here. The line is a fit with a gradient of 17.3 μm/Vpp. (b) The radial cavity mode profile obtained by plotting the spectral area of the cavity length scans at different FG3 amplitude settings. The inset figure shows the cavity emission as the cavity length is scanned across the Raman resonance for an ion displacement of 0 μm. The data is fitted with a Voigt function which is then used compute the spectral area.

and LEA, the camera image is calibrated to 2.0 μm per pixel. Fitting the fluorescence image on the camera with a Gaussian function, the ion's mean position is obtained. Figure 10(a) shows the ion's position as a function of the rf voltage of FG3 (before the amplifier). For each rf voltage setting, we place the ion at an anti-node of the cavity mode. Subsequently we scan the cavity frequency across the Raman resonance and record the cavity emission spectrum as shown in the inset of Figure 10(b). The spectral area is computed as an indicator for the relative coupling between the ion and cavity. The spectral area is used since it is immune to potential inhomogeneous broadening and therefore gives more reliable insight than the SPCM count rate at any given detuning. Figure 10(b) shows the spectral area as a function of the ion's radial position. A Gaussian fit gives a waist of $(8.4 \pm 0.1)\mu$m which agrees well with the calculated value of 8.5 μm for the expected waist of the TEM00 mode. When no additional rf is applied, the ion is trapped 3.9 μm from the cavity mode centre in this direction.

5. Conclusion

We have designed and built a novel ion trap with an integrated FFPC. By shielding the fibres inside tubular electrodes the detrimental effects on the trapping capabilities by the proximity of the fibres to the trapped ion have been mitigated.

By integrating additional electrodes into the design, we have succeeded in full control of the ion's position relative to the cavity mode solely by using radiofrequency signals. We have demonstrated that the excess micromotion induced by the phase mismatch of the additional rf signals can be explicitly minimised in all three spatial dimensions.

Furthermore, by probing the spatial structure of the cavity mode with the ion's cavity emission, it has been shown that the ion can be positioned with precisions on the order of 10 nm, which enables precise tuning of the ion-cavity coupling.

This state of the art design offers a promising solution to advancement in the implementation of large scale quantum networks using fibre-linked modular ion traps, an implementation considered key to advancing experimental quantum information science. Future experiments will look at incorporating FFPCs with mode matching optics (*29*) into this type of ion trap to facilitate highly efficient ion-ion coupling between fibre linked traps.

Data availability

The data used in this publication can be accessed at https://doi.org/10.25377/sussex.5515045.

Acknowledgements

E.K. would like to thank late Danny Segal for his wisdom and generosity during the short period he spent under Danny's tutelage.

Disclosure statement

No potential conflict of interest was reported by the authors.

Funding

We gratefully acknowledge support from EPSRC through the UK Quantum Technology Hub: Networked Quantum Information Technologies [EP/M013243/1], [EP/J003670/1].

References

(1) Keller, M.; Lange, B.; Hayasaka, K.; Lange, W.; Walther, H. Continuous generation of single photons with controlled waveform in an ion-trap cavity system. *Nature* **2004,** *431* (7012), 1075–1078. DOI: 10.1038/nature02961

(2) Leibrandt, D.R.; Labaziewicz, J.; Vuletić, V.; Chuang, I.L. Cavity Sideband Cooling of a Single Trapped Ion. *Phys. Rev. Lett.* **2009,** *103,* 103001. DOI: 10.1103/PhysRevLett.103.103001

(3) Herskind, P.F.; Dantan, A.; Marler, J.P.; Albert, M.; Drewsen, M. Realization of collective strong coupling with ion Coulomb crystals in an optical cavity. *Nat Phys* **2009,** *5* (7), 494–498. DOI: 10.1038/nphys1302

(4) Stute, A.; Casabone, B.; Schindler, P.; Monz, T.; Schmidt, P.O.; Brandstatter, B.; Northup, T.E.; Blatt, R. Tunable ion-photon entanglement in an optical cavity. *Nature* **2012,** *485* (7399), 482–485. DOI: 10.1038/nature11120

(5) Begley, S.; Vogt, M.; Gulati, G.K.; Takahashi, H.; Keller, M. Optimized Multi-ion Cavity Coupling. *Phys. Rev. Lett.* **2016,** *116,* 223001. DOI: 10.1103/PhysRevLett.116.223001

(6) Harty, T.P.; Allcock, D.T.C.; Ballance, C.J.; Guidoni, L.; Janacek, H.A.; Linke, N.M.; Stacey, D.N.; Lucas, D.M. High-fidelity Preparation, Gates, Memory, and Readout of a Trapped-ion Quantum Bit. *Phys. Rev. Lett.* **2014,** *113,* 220501. DOI: 10.1103/PhysRevLett.113.220501

(7) Harty, T.P.; Sepiol, M.A.; Allcock, D.T.C.; Ballance, C.J.; Tarlton, J.E.; Lucas, D.M. High-Fidelity Trapped-Ion Quantum Logic Using Near-field Microwaves. *Phys. Rev. Lett.* **2016,** *117,* 140501. DOI: 10.1103/PhysRevLett.117.140501

(8) Monz, T.; Schindler, P.; Barreiro, J.T.; Chwalla, M.; Nigg, D.; Coish, W.A.; Harlander, M.; Hänsel, W.; Hennrich, M.; Blatt, R. 14-qubit Entanglement: Creation and Coherence. *Phys. Rev. Lett.* **2011,** *106,* 130506. DOI: 10.1103/PhysRevLett.106.130506

(9) Lekitsch, B.; Weidt, S.; Fowler, A.G.; Mølmer, K.; Devitt, S.J.; Wunderlich, C.; Hensinger, W.K. Blueprint for a Microwave Trapped Ion Quantum Computer. *Science Advances* **2017,** *3* (2). Available from: http://advances.sciencemag.org/content/3/2/e1601540

(10) Crick, D.R.; Donnellan, S.; Ananthamurthy, S.; Thompson, R.C.; Segal, D.M. Fast Shuttling of Ions in a Scalable Penning Trap Array. *Review of Scientific Instruments* **2010,** *81* (1), 013111. DOI: 10.1063/1.3276699

(11) You, J.Q.; Tsai, J.S.; Nori, F. Scalable Quantum Computing with Josephson Charge Qubits. *Phys. Rev. Lett.* **2002,** *89,* 197902. DOI: 10.1103/PhysRevLett.89.197902.

(12) Cirac, J.I.; Zoller, P.; Kimble, H.J.; Mabuchi, H. Quantum State Transfer and Entanglement Distribution among Distant Nodes in a Quantum Network. *Phys. Rev. Lett.* **1997,** *78,* 3221–3224. DOI: 10.1103/PhysRevLett.78.3221

(13) Hucul, D.; Inlek, I.V.; Vittorini, G.; Crocker, C.; Debnath, S.; Clark, S.M.; Monroe, C. Modular Entanglement of Atomic Qubits Using Photons and Phonons. *Nat. Phys.* **2015,** *11* (1), 37–42. DOI: 10.1038/nphys3150

(14) Moehring, D.L.; Maunz, P.; Olmschenk, S.; Younge, K.C.; Matsukevich, D.N.; Duan, L.M.; Monroe, C. Entanglement of single-atom quantum bits at a distance. *Nature* **2007,** *449* (7158), 68–71. DOI: 10.1038/nature06118

(15) Steiner, M.; Meyer, H.M.; Deutsch, C.; Reichel, J.; Köhl, M. Single Ion Coupled to an Optical Fiber Cavity. *Phys. Rev. Lett.* **2013,** *110,* 043003. DOI: 10.1103/PhysRevLett.110.043003

(16) Ballance, T.G.; Meyer, H.M.; Kobel, P.; Ott, K.; Reichel, J.; Köhl, M. Cavity-induced Backaction in Purcell-enhanced Photon Emission of a Single Ion in an Ultraviolet Fiber Cavity. *Phys. Rev. A* **2017,** *95,* 033812. DOI: 10.1103/PhysRevA.95.033812

(17) Brandsttter, B.; McClung, A.; Schppert, K.; Casabone, B.; Friebe, K.; Stute, A.; Schmidt, P.O.; Deutsch, C.; Reichel, J.; Blatt, R.; et al. Integrated Fiber-mirror Ion Trap for Strong Ion-cavity Coupling. *Rev. Sci. Instrum.* **2013,** *84* (12), 123104. DOI: 10.1063/1.4838696

(18) Takahashi, H.; Kassa, E.; Christoforou, C.; Keller, M. Cavity-induced Anticorrelated Photon-emission Rates of a Single Ion. *Phys. Rev. A* **2017,** *96,* 023824. DOI: 10.1103/PhysRevA.96.023824

(19) Herskind, P.F.; Dantan, A.; Albert, M.; Marler, J.P.; Drewsen, M. Positioning of the rf Potential Minimum Line of a Linear Paul Trap with Micrometer Precision. *J. Phys. B: At Mol Opt Phys.* **2009,** *42* (15), 154008. Available from: http://stacks.iop.org/0953-4075/42/i=15/a=154008

(20) Takahashi, H.; Wilson, A.; Riley-Watson, A.; Oruevi, F.; Seymour-Smith, N.; Keller, M.; Lange, W. An Integrated Fiber Trap for Single-ion Photonics. *J. Phys.* **2013,** *15* (5), 053011. Available from: http://stacks.iop.org/1367-2630/15/i=5/a=053011

(21) Kassa, E. Single Ion Coupled to a High Finesse Optical Fibre Cavity for cQED in the Strong Coupling Regime [Ph.D. Thesis], University of Sussex.

(22) Berkeland, D.J.; Miller, J.D.; Bergquist, J.C.; Itano, W.M.; Wineland, D.J. Minimization of Ion Micromotion in a Paul Trap. *J. Appl. Phys.* **1998,** *83* (10), 5025–5033. DOI: 10.1063/1.367318

(23) Simulated on COMSOL Multiphysics 4.4

(24) Takahashi, H.; Morphew, J.; Oručević, F.; Noguchi, A.; Kassa, E.; Keller, M. Novel Laser Machining of Optical Fibers for Long Cavities with Low Birefringence. *Opt. Express* **2014,** *22* (25), 31317–31328. Available from: http://www.opticsexpress.org/abstract.cfm?URI=oe-22-25-31317

(25) PXY100, Piezojena Systems

(26) Noliac Multilayer NAC2124-C04

(27) Noliac Monolayer NCE51-Ring-OD15-I9-TH2

(28) Chuah, B.L.; Lewty, N.C.; Cazan, R.; Barrett, M.D. Detection of Ion Micromotion in a Linear Paul Trap with a High Finesse Cavity. *Opt. Express* **2013,** *21* (9), 10632–10641.

(29) Gulati, G.K.; Takahashi, H.; Podoliak, N.; Horak, P.; Keller, M. Fiber Cavities with Integrated Mode Matching Optics. *Sci. Rep.* **2017,** *7* (1). DOI: 10.1038/s41598-017-05729-8

Chapter 4

Strong coupling of a single ion to an optical cavity

The trap structure and the process on how to move the ion and optimise its position, was analysed in the previous chapter/publication. After moving the ion to the centre of the cavity mode, the next step was to measure the coupling of the ion to the cavity and show that it lies in the strong coupling regime. In this chapter, I include our publication "Strong coupling of a single ion to an optical cavity" [65]. In this publication we cover how we measured the ion-cavity coupling, as well as the vacuum Rabi splitting in the three-level bimodal system. In most cases the coupling can be extracted from the separation of the peaks in the Rabi splitting spectrum but as we will see, this was not possible in our system and we had to come up with another way of measuring the coupling strength.

For the purpose of this experiment we made a couple of changes to the experimental setup. An additional beam at 393 nm was added to assist with Doppler cooling. During the measurement when the cavity is resonant on the $P \leftrightarrow D$ transition, the 397 nm beam offers inefficient cooling due to the fact that the 397 nm ($S \leftrightarrow P$) transition, being part of the 3-level system, is affected by the Purcell effect [67]. In addition, there are now three 866 nm laser beams entering the system with individual polarisation control. One of them, as before, is a free space beam, and the other two are injected through the single mode fibre of the cavity. These beams are used for the optical pumping and probing of the ion.

To extract the ion-cavity coupling of our system, we use the single photon emission spectrum of the system through a vacuum stimulated Raman transition from $S_{1/2}$ to $D_{3/2}$. The pump laser at 397 nm is tuned with a detuning of Δ_p from the $S_{1/2} \leftrightarrow P_{1/2}$ transition, while the cavity detuning Δ_c from the $P_{1/2} \leftrightarrow D_{3/2}$ transition is scanned across the Raman resonance. From this Raman spectroscopy we obtain a single photon spectrum with a Lorentzian shape, where the linecentre is shifted by an amount δ. This shift δ depends on the Rabi frequency but more importantly, on the coupling g_0. By keeping the Rabi frequency constant we take a Raman spectroscopy for different pump detunings Δ_p and record the shift for each case. We run a simulation of this process with only free parameter g_0. By fitting the plot of the shift δ versus the pump detuning Δ_p from our experimental data, and comparing

it with the simulations, we can extract the coherent coupling, g_0. The coherent ion-cavity coupling extracted is $g_0 = 2\pi \times (15.1 \pm 0.1)$ MHz. Multiplying the coherent coupling by the Clebsh-Gordan coefficients for the σ^+ and σ^- transitions, we obtain $g = 2\pi \times (12.3 \pm 0.1)$ MHz. The measured ion-cavity coupling is bigger than the atomic decay rate, $\gamma = 2\pi \times 11.5$ MHz, and the cavity decay rate, $\kappa = 2\pi \times (4.1 \pm 0.1)$ MHz, which places our system in the strong coupling regime ($g > \gamma, \kappa$).

A small magnetic field is applied along the cavity axis, in order to align the quantisation axis to the cavity axis. Therefore, the cavity supports two polarisations σ^- and σ^+. The system forms a closed three-level lambda system, interconnected via a bimodal cavity. As we saw in the theory section, for a two level atom there are two dressed states. In this configuration there are three dressed states. The extra state is a dark state, and its emergence is similar to the effect of electromagnetically induced transparency.

In the following publication, we measure the vacuum Rabi splitting for the three-level bimodal system. Figure 4, of the following publication, shows the contribution from the excitations to all three dressed states. Due to the effect of the dark state, it is hard to distinguish the two outer peaks (therefore hard to obtain g using this measurement), which appear as little bumps at the wings of the spectrum. Nevertheless, the spectrum obtained from the experimental data agrees with the numerical simulations.

This publication has a big significance as it is the first reported measurement of strong coupling of a single ion to an optical cavity.

Attached to the publication, there is a supplementary document where more details on the publication and its importance are given. In the supplementary material we give more information on the cavity parameters, the theoretical model, and how we estimated the uncertainty on the coherent coupling. There is also an estimation for the cavity driving amplitude which is present in the transmission spectroscopy for the vacuum Rabi splitting, and how it is incorporated in the system's Hamiltonian. Finally we give some information on the potential applications for strongly coupled ion-cavity systems, and how it can be used to generate entanglement between remotely trapped ions.

For this experiment, I contributed into setting up the peripheral systems, like the lasers for the state preparation and their control (especially the control of polarisation). I assisted in the data acquisition and analysis. Finally, I contributed in the writing of the publication and the production of the figures.

Editors' Suggestion

Strong Coupling of a Single Ion to an Optical Cavity

Hiroki Takahashi,* Ezra Kassa, Costas Christoforou, and Matthias Keller
Department of Physics and Astronomy, University of Sussex, Brighton BN1 9QH, United Kingdom

(Received 15 April 2019; published 2 January 2020)

Strong coupling between an atom and an electromagnetic resonator is an important condition in cavity quantum electrodynamics. While strong coupling in various physical systems has been achieved so far, it remained elusive for single atomic ions. Here, we achieve a coupling strength of $2\pi \times (12.3 \pm 0.1)$ MHz between a single $^{40}Ca^{+}$ ion and an optical cavity, exceeding both atomic and cavity decay rates which are $2\pi \times 11.5$ and $2\pi \times (4.1 \pm 0.1)$ MHz, respectively. We use cavity assisted Raman spectroscopy to precisely characterize the ion-cavity coupling strength and observe a spectrum featuring the normal mode splitting in the cavity transmission due to the ion-cavity interaction. Our work paves the way towards new applications of cavity quantum electrodynamics utilizing single trapped ions in the strong coupling regime for quantum optics and quantum technologies.

DOI: 10.1103/PhysRevLett.124.013602

Coupling between atoms and electromagnetic fields is a ubiquitous physical process that underlies a plenitude of electromagnetic phenomena. In cavity quantum electrodynamics (CQED), this interaction is studied in its simplest form where a single atomic emitter is coupled to well-defined electromagnetic modes of a resonator [1,2]. In many applications of CQED, the coherent atom-photon interaction rate needs to exceed the decoherence rates of the system. This so-called strong coupling regime has been attained in many physical systems including neutral atoms [3,4], solid state systems [5–8], and an ensemble of trapped ions [9]. Strongly coupled light-matter systems resulted in remarkable applications such as a one-atom optical switch [10] and a quantum optical circulator [11]. However, despite decade-long attempts [9,12–20] strong coupling has remained elusive for single trapped ions until now.

Because of their outstanding properties such as long coherence times [21] and high-fidelity quantum controls [22], trapped ions are a leading system for optical atomic clocks [23,24], quantum metrology [25,26], and quantum computation [27,28]. The setting of CQED brings about exciting possibilities to connect individual quantum devices by providing efficient quantum interfaces with optical photons [29]. Compared to single ions in free space [30,31], the entanglement generation efficiency of remote ions based on strongly coupled ion-cavity systems is enhanced by orders of magnitude [32]. This enables the distributed architecture for large-scale quantum information processing using photonic networks [33]. Here, by coupling a single ion to an optical cavity in the strong coupling regime for the first time, we demonstrate a key milestone for this enabling technology.

In the past, Fabry-Perot cavities with macroscopic mirrors were successfully combined with ion traps [14,17,18]. In these experiments, however, the ion-cavity coupling was in the weak coupling regime. Since the emitter-cavity coupling scales as $\propto 1/\sqrt{V_m}$ where V_m is the cavity's mode volume, it is essential to reduce V_m to achieve strong coupling. The main challenge in ion-cavity systems is to achieve small mode volume without disturbing the trapping field when incorporating dielectric mirrors near the trapping region. Employing laser machined fiber-based Fabry-Perot cavities (FFPCs) has proven to be a viable solution for this purpose and resulted in several successful implementations recently [19,20,34]. However, none of these experiments achieved a coupling strength which exceeds the atomic and cavity decay rates simultaneously. Based on the ion trap with an integrated FFPC presented in [34] and the technique to precisely position the ion in the cavity field [35], in this work we achieve a coherent ion-cavity coupling of $g = 2\pi \times (12.3 \pm 0.1)$ MHz greater than both the atomic decay rate of the $P_{1/2}$ state of $\gamma = 2\pi \times 11.5$ MHz [36] and the cavity decay rate of $\kappa = 2\pi \times (4.1 \pm 0.1)$ MHz [32]. This gives us a cooperativity ($=g^2/\gamma\kappa$) of 3.2, on a par with the highest value achieved for an ion-cavity system [17] but with a considerably higher photon extraction rate.

Our experimental apparatus is an endcap-style Paul trap for $^{40}Ca^{+}$ ions with an integrated FFPC [see Fig. 1(a) and [32,34,35] for more details]. The FFPC is coupled to the electronic transition between the $P_{1/2}$ and $D_{3/2}$ states at 866 nm [see Fig. 1(b)]. The cavity field decay rate κ is measured to be $2\pi \times (4.1 \pm 0.1)$ MHz [32]. Two radial electrodes (RE3 and RE4) are used to displace the rf potential minimum by applying signals synchronous and in phase to the main drive [35] (RE1 and RE2 are used for micromotion compensation). In this way the ion is translated radially without incurring excess micromotion. Using a trapped ion as a probe for the cavity field [35], we

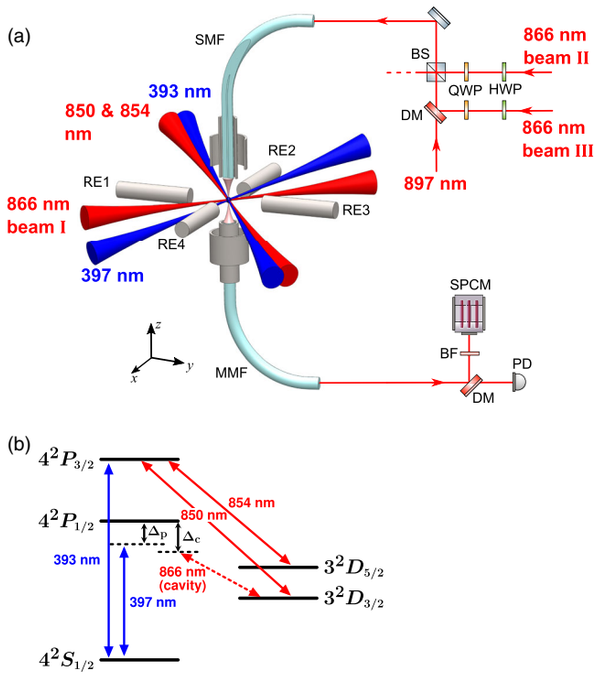

FIG. 1. (a) A schematic of the experimental setup. BF, bandpass filter; BS, beam splitter; DM, dichroic mirror; HWP, half-wave plate; MMF, multimode fiber; PD, photodiode; QWP, quarter-wave plate; RE, radial electrode; SMF, single-mode fiber; SPCM, single-photon counting module. (b) Energy levels of $^{40}Ca^{+}$ ion with driving lasers and the cavity on the relevant transitions.

determine that the center of the TEM_{00} cavity mode is located at $(3.4 \pm 0.1, 6.4 \pm 0.3)$ μm in the x and y directions, respectively, from the ion's original position when RE3 and RE4 are grounded. The ion is Doppler cooled on the $S_{1/2} - P_{3/2}$ transition with a laser at 393 nm to circumvent inefficient cooling on the $S_{1/2} - P_{1/2}$ transition caused by the strong Purcell effect when the cavity is near resonant on the $P_{1/2} - D_{3/2}$ transition [34]. Lasers at 850 and 854 nm repump the ion from the metastable D states into the $S_{1/2}$ state. Three laser beams at 866 nm (beams I, II, and III) with individual polarization controls are used for optical pumping and probing of the ion. Two of them (beams II and III) are injected into the input SM fiber to drive the FFPC. A laser beam at 897 nm is also sent into the FFPC through the SM fiber with its transmission used to stabilize the length of the FFPC.

Having moved the ion to the radial center of the FFPC, we now characterize g_0 with the optimized overlap at the antinode of the cavity. The ion-cavity coupling is quantified by analyzing the single-photon emission spectra of the ion-cavity system. Figure 2(a) shows the pulse sequences of the lasers for this measurement. In combination with the cavity locked close to the $P_{1/2} - D_{3/2}$ transition with a detuning Δ_c, a short pulse of the 397 nm laser with a detuning Δ_p results in a single photon in the cavity via a vacuum-stimulated Raman transition from the $S_{1/2}$ to the $D_{3/2}$ state [14]. Normally the Raman resonance condition dictates $\Delta_p = \Delta_c$. However, due to the dressing of the ion's states by the cavity photons, the resonance frequency of the $P_{1/2} - D_{3/2}$ transition and therefore the Raman resonance are shifted [37]. Figure 2(b) shows a spectrum of single-photon emission as a function of Δ_c while Δ_p is fixed at -10 MHz. It can be clearly seen that the peak frequency of the spectrum is shifted by an amount δ from the expected $\Delta_p = \Delta_c$ condition. We repeat this Raman spectroscopy for different Δ_p as shown in Fig. 2(c) to measure the dependence of δ on Δ_p. The frequency shift δ exhibits a dispersionlike profile whose amplitude and gradient depend on the magnitude of g_0. Because δ also depends on the Rabi frequency Ω_{397} of the 397 nm laser through its own ac Stark shift, we independently measure Ω_{397} to be $2\pi \times (11.9 \pm 0.4)$ MHz by the electron shelving method employed in [34]. Given Ω_{397} and other known experimental parameters such as the beam detunings, beam polarizations, and the magnetic field, the single-photon emission spectrum and hence δ can be precisely simulated by solving time-dependent master equations with g_0 as the only free parameter [see the inset of Fig. 2(d) and [32]]. Utilizing the dependence of δ on g_0 and fitting this numerical model to the experimental data as shown in Fig. 2(d), we obtain the coherent ion-cavity coupling $g_0 = 2\pi \times (15.1 \pm 0.1)$ MHz [32].

A small magnetic field (= 0.9 G) is applied to align the quantization axis to the cavity axis such that the cavity supports two distinct polarizations σ_+ and σ_-. As shown in Fig. 3(a), the ion is simultaneously coupled to these two polarization modes on the transitions connecting the Zeeman sublevels in the $P_{1/2}$ and $D_{3/2}$ state manifolds. This configuration effectively realizes a closed three-level lambda system interconnected via a bimodal cavity. When a two-level atom is coupled to a single optical mode, there are two dressed states $(|g,1\rangle + |e,0\rangle)/\sqrt{2}$ and $(|g,1\rangle - |e,0\rangle)/\sqrt{2}$ with an energy gap $2g$ ($\hbar = 1$) in the subspace for the first excitation from the ground state $(= |g,0\rangle)$ [see Fig. 3(b)]. Here, g and e denote the ground and excited states of the atom, respectively, and 0 and 1 denote the intracavity photon number. As a result, a coherent oscillation between $|g,1\rangle$ and $|e,0\rangle$ occurs at the vacuum Rabi frequency of $2g$. Similarly, for the bimodal system with three atomic levels, the subspace for the first excitation includes three originally degenerate states $|a,1,0\rangle$, $|b,0,1\rangle$, and $|c,0,0\rangle$. Here, the notation indicates a product of the atomic state and the photon number states of the two cavity modes [see Fig. 3(c)]. Because of the atom-cavity coupling, the system now has three dressed states $|u_+\rangle$, $|u_-\rangle$, and $|u_0\rangle$:

$$|u_\pm\rangle = \frac{g_1|a,1,0\rangle + g_2|b,0,1\rangle \pm \lambda|c,0,0\rangle}{\sqrt{2}\lambda}, \qquad (1)$$

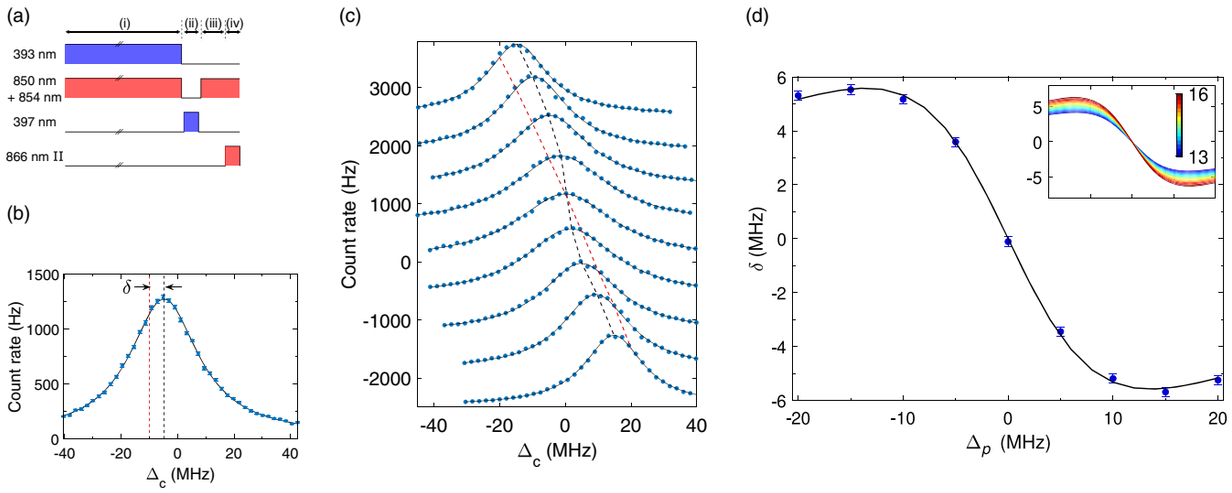

FIG. 2. (a) The pulse sequences for the single-photon generation: (i) Doppler cooling for 6 μs. (ii) 300 ns-long pulse of the 397 nm laser to generate a single photon in the cavity. (iii) Recycling the ion's population back to the $S_{1/2}$ state for 500 ns. (iv) A pulse of the 866 nm laser is injected to the cavity. The 866 nm laser is frequency locked to the resonance to the $P_{1/2} - D_{3/2}$ transition. Therefore, its transmission peak provides an absolute frequency reference for Δ_c. (b) Single-photon emission spectrum as a function of Δ_c with Δ_p at -10 MHz. The solid line is a Lorentzian fit. The vertical dashed lines indicate the center frequency of the peak (black) and the frequency expected from the condition $\Delta_p = \Delta_c$ (red). The same applies to the dashed lines in (c). (c) Single-photon emission spectra with different Δ_p. From the top to the bottom traces, Δ_p varies from -20 to $+20$ MHz with an interval of 5 MHz. The traces are vertically offset to avoid overlapping. (d) The shift of the Raman resonance δ as a function of Δ_p from the data set in (c). The solid line is a fit by the numerical simulation. The inset figure shows superimposed traces of δ from numerical simulations with $g_0/(2\pi)$ varying from 13 to 16 MHz.

$$|u_0\rangle = \frac{g_2|a,1,0\rangle - g_1|b,0,1\rangle}{\lambda}, \tag{2}$$

where $\lambda = \sqrt{g_1^2 + g_2^2}$. Note that $|u_0\rangle$ is a dark state which is decoupled from the atomic upper state $|c\rangle$. The emergence of this state is very similar to the effect of electromagnetically induced transparency [38]. The difference here is that the quantized cavity fields, instead of classical lasers, interconnect the three atomic levels. On the other hand, a *bright state* can also be constructed as $|v\rangle = (g_1|a,1,0\rangle + g_2|b,0,1\rangle)/\lambda$ in which the excitation amplitudes to $|c,0,0\rangle$ from the constituent states interfere constructively. $|u_+\rangle$ and $|u_-\rangle$ can be expressed as

$$|u_\pm\rangle = \frac{|v\rangle \pm |c,0,0\rangle}{\sqrt{2}}, \tag{3}$$

with an energy gap of 2λ [Fig. 3(c)]. Consequently, in the same way as between $|g,1\rangle$ and $|e,0\rangle$ in the two-level case, the coherent oscillation occurs between $|v\rangle$ and $|c,0,0\rangle$ at a frequency of 2λ. This oscillation corresponds to the characteristic emission (and absorption) of a single photon into (and from) the two optical modes simultaneously in a superposition. Hence, the vacuum Rabi frequency—the frequency at which a single excitation is exchanged between the atomic and optical degrees of freedom—is given by $2g = 2\lambda$.

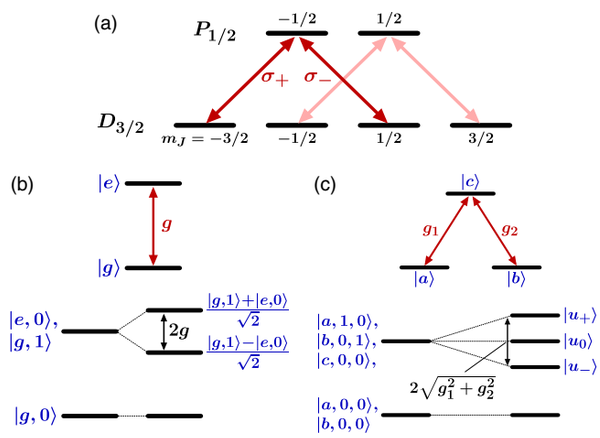

FIG. 3. (a) The Zeeman sublevels in the $P_{1/2}$ and $D_{3/2}$ state manifolds interacting with a bimodal cavity. (b) Top: A two-level atom coupled to a single optical mode with a coupling strength g. Bottom: The level diagram of the total energy of the system with (without) the atom-cavity coupling [right (left)]. (c) Top: A three-level atom coupled to two optical modes simultaneously with coupling strength g_1 and g_2, respectively. Bottom: The level diagram of the three-level bimodal system with (without) the atom-cavity coupling [right (left)]. The energy levels of the first excited states split into three levels with corresponding dressed states.

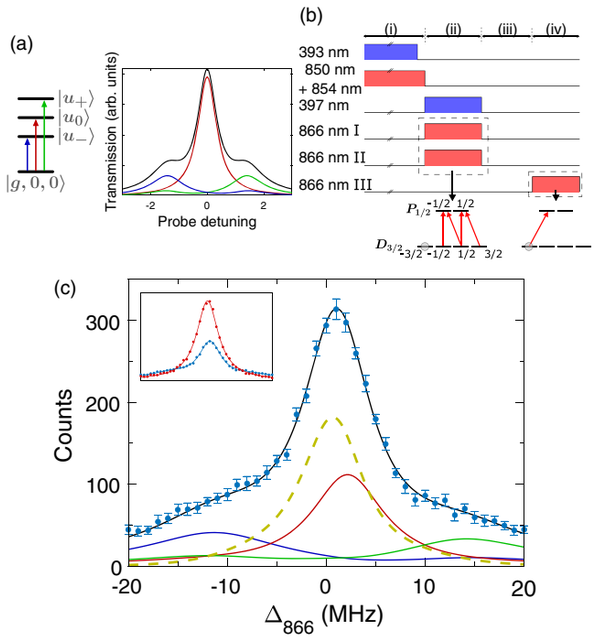

FIG. 4. (a) A model calculation for the ideal three-level system. The solid line shows the expected spectrum of transmitted photons as a function of the probe detuning. Here, $g_1 = g_2 = g$ and the probe frequency is normalized by g. The underlying contributions of the individual dressed states are shown in the same colors as the corresponding excitations in the level diagram on the left. (b) Laser pulse sequences: (i) 5 μs-long Doppler cooling. The duration of the repumping beams is longer than that of the 393 nm beam in order to prepare the ion in the $S_{1/2}$ state. (ii) Optical pumping for 3 μs. (iii) An interval to wait for the intensities of the optical pumping lasers to sufficiently diminish. (iv) Probing with beam III. (c) The counts of the transmitted photons of beam III as a function of its detuning. The background counts (~90) from stray light are subtracted. The solid black line is the result of numerical calculation (see the main text). The underlying contributions are also shown. In addition the contribution from nondressed states is shown in the yellow dashed line. The inset also shows a spectrum taken without the ion (red) superposed with the spectrum with the ion (blue).

Applying this picture to the actual energy levels of $^{40}Ca^+$ in Fig. 3(a), g_1 and g_2 are derived from g_0 by multiplication with the Clebsh-Gordan coefficients for the σ_+ and σ_- transitions, which are $1/\sqrt{2}$ and $1/\sqrt{6}$, respectively. With $g_0 = 2\pi \times (15.1 \pm 0.1)$ MHz, $g = 2\pi \times (12.3 \pm 0.1)$ MHz is obtained. Therefore, the coupling of the single ion to the cavity g exceeds both the atomic decay rate of the $P_{1/2}$ level γ ($=2\pi \times 11.5$ MHz) [36] and the cavity decay rate κ [$=2\pi \times (4.1 \pm 0.1)$ MHz], placing our system in the strong coupling regime ($g > \gamma, \kappa$).

The characteristic vacuum Rabi splitting in the three-level bimodal system as shown in Fig. 3(c) can be probed by weakly driving the cavity and detecting the transmission. Figure 4(a) shows the expected spectrum of the transmitted photons when the ideal three-level bimodal system is probed with a near-resonant coherent light. There are three underlying resonant peaks corresponding to the three distinct excitations from the ground state. Figure 4(b) shows the laser pulse sequences used to probe this in the experiment. Beams I and II of the 866 nm laser are applied with π and σ_- polarizations, respectively, in order to optically pump the ion into the $D_{3/2}$ $m_J = -3/2$ state. Subsequently, a pulse of beam III in the σ_+ polarization is injected and its transmission through the FFPC is measured. The FFPC is locked to the atomic resonance ($\Delta_c = 0$). The intensity of beam III in the cavity is estimated in terms of the displacement amplitude to the intracavity field [32]. Figure 4(c) shows the resulting spectrum of the transmitted photons as the detuning of beam III from the atomic resonance ($\equiv \Delta_{866}$) is scanned. The spectrum is significantly modified by the ion-cavity coupling [see the inset of Fig. 4(c)]. The data show good agreement with the numerical simulation shown as the black solid line in Fig. 4(c). Only the vertical scaling and a small horizontal offset (~0.47 MHz) are adjusted to fit the simulated curve to the measured data. The horizontal offset is likely to have resulted from an error in the calibration of the frequency of the 866 nm laser. The figure also shows the simulated contributions of the excitations to the individual dressed states and contribution from other states. There is a finite probability that the probing laser excites the ion and incoherently distributes its population via spontaneous decays from the $P_{1/2}$ state. This results in the transmission of subsequent photons without interacting with the ion and creates the central peak in a dashed yellow line in the figure. Note that this probability increases as g increases and hence progressively fewer photons are required to probe the system, whereas in practice a certain number of photons are required at the detector to ensure a decent signal-to-noise ratio. Despite this noise, the wings of the observed spectrum indicate the deviation from a single-peaked structure and the presence of the dressed states $|u_\pm\rangle$ with an expected separation of $2g$.

In conclusion, we have achieved the strong coupling regime for the first time with a single ion, where the vacuum Rabi frequency exceeds both atomic and cavity decoherence rates. Moreover, the characteristic energy structure of the dressed states inherent to our coupled ion-cavity system has been successfully probed by spectroscopic means. The key milestones that have led to this work are the overcoming of practical limitations that have limited the successful integration of an ion trap with a miniature cavity for decades and the ability to precisely control the ion's position in the cavity mode. Strong coupling between a single ion and an optical cavity facilitates novel opportunities to combine the unparalleled capabilities of trapped ions with quantum photonics. It enables applications such as highly efficient single-photon sources and high-fidelity ion-photon quantum interfaces, key components in quantum networks and

quantum computing. Without further optimization, a numerical study shows that a heralded entanglement efficiency of 1.7% at a rate of 8.5 kHz between two remote ions can be achieved, a factor of ∼1900 improvement over previous work [30]. Moreover, our FFPC can be readily modified to further enhance the single-photon generation efficiency by simply increasing the external coupling of one of the cavity mirrors or optimizing the mirror geometry [32,39].

We gratefully acknowledge support from EPSRC through EP/J003670/1 and the U.K. Quantum Technology Hub: NQIT-Networked Quantum Information Technologies (EP/M013243/1).

Note added in the proof.—Recently, we became aware of a work [40] that reports an enhanced entanglement generation rate between remotely trapped ions using fluorescence collection. Our cavity-based approach enables a further improvement by two orders of magnitude over the rate achieved in [40].

*takahashi@qiqb.otri.osaka-u.ac.jp

[1] H. J. Kimble, Phys. Scr. **T76**, 127 (1998).
[2] S. Girvin, M. Devoret, and R. Schoelkopf, Phys. Scr. **T137**, 014012 (2009).
[3] A. Boca, R. Miller, K. M. Birnbaum, A. D. Boozer, J. McKeever, and H. J. Kimble, Phys. Rev. Lett. **93**, 233603 (2004).
[4] P. Maunz, T. Puppe, I. Schuster, N. Syassen, P. W. H. Pinkse, and G. Rempe, Phys. Rev. Lett. **94**, 033002 (2005).
[5] J. P. Reithmaier, G. Sek, A. Löffler, C. Hofmann, S. Kuhn, S. Reitzenstein, L. V. Keldysh, V. D. Kulakovskii, T. L. Reinecke, and A. Forchel, Nature (London) **432**, 197 (2004).
[6] T. Yoshie, A. Scherer, J. Hendrickson, G. Khitrova, H. Gibbs, G. Rupper, C. Ell, O. Shchekin, and D. Deppe, Nature (London) **432**, 200 (2004).
[7] A. Wallraff, D. I. Schuster, A. Blais, L. Frunzio, J. Majer, S. Kumar, S. M. Girvin, and R. J. Schoelkopf, Nature (London) **431**, 162 (2004).
[8] I. Chiorescu, P. Bertet, K. Semba, Y. Nakamura, C. Harmans, and J. Mooij, Nature (London) **431**, 159 (2004).
[9] P. F. Herskind, A. Dantan, J. P. Marler, M. Albert, and M. Drewsen, Nat. Phys. **5**, 494 (2009).
[10] I. Shomroni, S. Rosenblum, Y. Lovsky, O. Bechler, G. Guendelman, and B. Dayan, Science **345**, 903 (2014).
[11] M. Scheucher, A. Hilico, E. Will, J. Volz, and A. Rauschenbeutel, Science **354**, 1577 (2016).
[12] G. R. Guthöhrlein, M. Keller, K. Hayasaka, W. Lange, and H. Walther, Nature (London) **414**, 49 (2001).
[13] A. B. Mundt, A. Kreuter, C. Becher, D. Leibfried, J. Eschner, F. Schmidt-Kaler, and R. Blatt, Phys. Rev. Lett. **89**, 103001 (2002).
[14] M. Keller, B. Lange, K. Hayasaka, W. Lange, and H. Walther, Nature (London) **431**, 1075 (2004).
[15] D. R. Leibrandt, J. Labaziewicz, V. Vuletić, and I. L. Chuang, Phys. Rev. Lett. **103**, 103001 (2009).
[16] J. D. Sterk, L. Luo, T. A. Manning, P. Maunz, and C. Monroe, Phys. Rev. A **85**, 062308 (2012).
[17] A. Stute, B. Casabone, P. Schindler, T. Monz, P. Schmidt, B. Brandstätter, T. Northup, and R. Blatt, Nature (London) **485**, 482 (2012).
[18] A. Stute, B. Casabone, B. Brandstätter, K. Friebe, T. Northup, and R. Blatt, Nat. Photonics **7**, 219 (2013).
[19] M. Steiner, H. M. Meyer, C. Deutsch, J. Reichel, and M. Köhl, Phys. Rev. Lett. **110**, 043003 (2013).
[20] T. G. Ballance, H. M. Meyer, P. Kobel, K. Ott, J. Reichel, and M. Köhl, Phys. Rev. A **95**, 033812 (2017).
[21] T. P. Harty, D. T. C. Allcock, C. J. Ballance, L. Guidoni, H. A. Janacek, N. M. Linke, D. N. Stacey, and D. M. Lucas, Phys. Rev. Lett. **113**, 220501 (2014).
[22] C. J. Ballance, T. P. Harty, N. M. Linke, M. A. Sepiol, and D. M. Lucas, Phys. Rev. Lett. **117**, 060504 (2016).
[23] C. W. Chou, D. B. Hume, J. C. J. Koelemeij, D. J. Wineland, and T. Rosenband, Phys. Rev. Lett. **104**, 070802 (2010).
[24] N. Huntemann, C. Sanner, B. Lipphardt, C. Tamm, and E. Peik, Phys. Rev. Lett. **116**, 063001 (2016).
[25] S. Kotler, N. Akerman, Y. Glickman, A. Keselman, and R. Ozeri, Nature (London) **473**, 61 (2011).
[26] I. Baumgart, J.-M. Cai, A. Retzker, M. B. Plenio, and C. Wunderlich, Phys. Rev. Lett. **116**, 240801 (2016).
[27] S. Debnath, N. M. Linke, C. Figgatt, K. A. Landsman, K. Wright, and C. Monroe, Nature (London) **536**, 63 (2016).
[28] T. Monz, D. Nigg, E. A. Martinez, M. F. Brandl, P. Schindler, R. Rines, S. X. Wang, I. L. Chuang, and R. Blatt, Science **351**, 1068 (2016).
[29] H. J. Kimble, Nature (London) **453**, 1023 (2008).
[30] D. Hucul, I. Inlek, G. Vittorini, C. Crocker, S. Debnath, S. Clark, and C. Monroe, Nat. Phys. **11**, 37 (2015).
[31] C. Crocker, M. Lichtman, K. Sosnova, A. Carter, S. Scarano, and C. Monroe, Opt. Express **27**, 28143 (2019).
[32] See Supplemental Material at http://link.aps.org/supplemental/10.1103/PhysRevLett.124.013602 for experimental details and numerical simulations.
[33] C. Monroe, R. Raussendorf, A. Ruthven, K. R. Brown, P. Maunz, L.-M. Duan, and J. Kim, Phys. Rev. A **89**, 022317 (2014).
[34] H. Takahashi, E. Kassa, C. Christoforou, and M. Keller, Phys. Rev. A **96**, 023824 (2017).
[35] E. Kassa, H. Takahashi, C. Christoforou, and M. Keller, J. Mod. Opt. **65**, 520 (2018).
[36] M. Hettrich, T. Ruster, H. Kaufmann, C. F. Roos, C. T. Schmiegelow, F. Schmidt-Kaler, and U. G. Poschinger, Phys. Rev. Lett. **115**, 143003 (2015).
[37] M. Albert, J. P. Marler, P. F. Herskind, A. Dantan, and M. Drewsen, Phys. Rev. A **85**, 023818 (2012).
[38] M. Fleischhauer, A. Imamoglu, and J. P. Marangos, Rev. Mod. Phys. **77**, 633 (2005).
[39] K. Ott, S. Garcia, R. Kohlhaas, K. Schüppert, P. Rosenbusch, R. Long, and J. Reichel, Opt. Express **24**, 9839 (2016).
[40] D. P. Nadlinger, B. C. Nichol, S. An, P. Drmota, T. G. Ballance, K. Thirumalai, J. F. Goodwin, D. M. Lucas, and C. J. Ballance, arXiv:1911.10841.

Supplemental Material

Hiroki Takahashi,[1] Ezra Kassa,[1] Costas Christoforou,[1] and Matthias Keller[1]
[1]*Department of Physics and Astronomy, University of Sussex, Brighton, BN1 9QH, United Kingdom*

TRAP ELECTRODES AND INTEGRATION OF A FFPC

The main part of the trap is a pair of electrode assemblies, each consisting of two concentric electrodes separated by a ceramic spacer (see Fig.1). A radio-frequency (rf) voltage at 19.8 MHz is applied to the outer electrodes while the inner electrodes are held at rf-ground to create a trapping quadrupole electric field in between the assemblies. Two optical fibers whose end facets act as cavity mirrors are inserted inside the inner electrodes. As a result, a Fabry-Perot cavity is formed in the gap between the assemblies. This design enables effective shielding of the dielectric surfaces of the fibers, and thus achieves robust trapping of a single ion inside an optical cavity with a small mode volume. One of the fibers is a single-mode fiber (SMF) to serve as a cavity input whereas the other one is a multimode fiber (MMF) to collect the cavity output.

CAVITY PARAMETERS

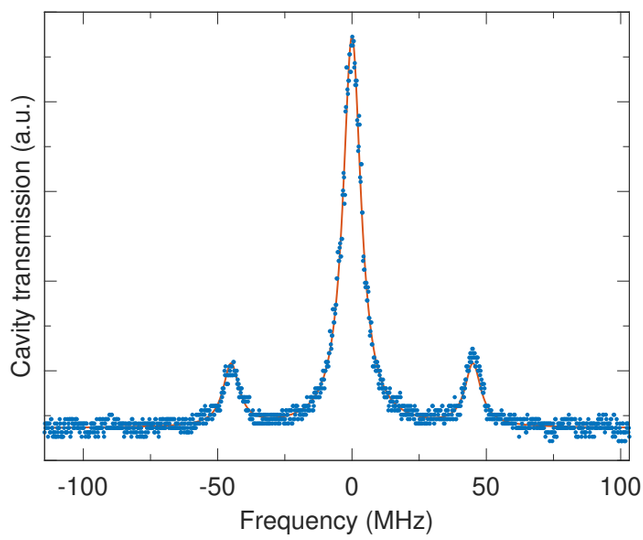

FIG. S1: Transmission signal as the FFPC is scanned over resonance. The horizontal axis is calibrated in frequency by the sideband peaks at ±45 MHz. The solid line is a fit with Lorentz functions.

Fig. S1 shows a transmission signal when a laser at 866 nm is injected to the FFPC and the cavity length is scanned over a resonance. The laser is modulated at 45 MHz such that the sidebands on the transmission signal serve as a frequency reference. From the fit, the half-width-half-maximum of the central peak ($=\kappa/(2\pi)$) is deduced. Repeating this measurement 20 times, we obtained $\kappa = 2\pi \times (4.1 \pm 0.1)$ MHz. The cavity length($= L_{\mathrm{cav}}$) of 369.5 μm was obtained by scanning the frequency of 897 nm laser injected in the FFPC by one free spectral range (FSR) while monitoring the laser's wavelength with a calibrated wavelength meter at the same time, and using the relation $L_{\mathrm{cav}} = c/(2\,\mathrm{FSR})$ where c is the speed of light. From these, we computed a cavity finesse of ∼50000. The transmission of each mirror is 25 ppm from which we estimate the residual absorption/scatter loss of the cavity to be 75 ppm. The radii of curvature (ROC) of the two fiber mirrors were determined by using white light interferometry [1] prior to the installation of the FFPC into the ion trap. They are 561 μm and 558 μm respectively. From L_{cav} and ROC, the ideal ion-cavity coupling without the ion's motion taken into account is calculated to be $(2\pi) \times 17.3$ MHz.

THEORETICAL MODEL

The system Hamiltonian in the Raman spectroscopy in the interaction picture is described as follows:

$$H = H_0 + H_B + H_{\text{pump}} + H_{\text{ion-cav}}, \tag{S1}$$

with the atomic detuning term

$$H_0 = \hbar\Delta_p \sum_{m_S} |S, m_S\rangle\langle S, m_S| + \Delta_c \sum_{m_D} |D, m_D\rangle\langle D, m_D|\,, \tag{S2}$$

the Zeeman term

$$H_B = \hbar B \sum_{L=S,P,D} \sum_{m_J} g_L \mu_B m_J \,|L, m_J\rangle\langle L, m_J|\,, \tag{S3}$$

the pump term describing the interaction of the ion with the pump laser at the $S_{1/2} \to P_{1/2}$ transition,

$$H_{\text{pump}} = \frac{\hbar\Omega_{397}}{2} f(t) \sum_q \sum_{m_S, m_P} \left[\varepsilon_q C(J_S m_S, 1q; J_P m_P)\,|P, m_P\rangle\langle S, m_S| + \text{H.c.}\right], \tag{S4}$$

and the ion-cavity interaction,

$$H_{\text{ion-cav}} = \hbar g_0 \sum_{m_P, m_D} \left[C(J_D m_D, 11; J_P m_P) a_+ \,|P, m_P\rangle\langle D, m_D| + C(J_D m_D, 1-1; J_P m_P) a_- \,|P, m_P\rangle\langle D, m_D| + \text{H.c.}\right]. \tag{S5}$$

The ionic state is described by the Zeeman states $\{|S, m_S\rangle, |P, m_P\rangle, |D, m_D\rangle\}$. B is the amplitude of the applied magnetic field, $g_L (L = S, P, D)$ is the Landé g-factor, μ_B is the Bohr magneton, ϵ_q is the polarization component of the pump beam in the spherical basis, and $C(J_U m_U, 1q; J_V m_V)$ is the Clebsch-Gordan coefficient given by a Wigner 3-j symbol:

$$C(J_U m_U, 1q; J_V m_V) = (-1)^{J_U - 1 + m_V} \sqrt{2J_V + 1} \begin{pmatrix} J_U & 1 & J_V \\ m_U & q & -m_V \end{pmatrix}. \tag{S6}$$

a_+ and a_- are the annihilation operators for the σ_+ and σ_- polarization modes of the cavity. $f(t)$ represents the pulse shape of the pump beam. Numerical simulation are carried out by solving master equations given by,

$$\begin{aligned} \frac{\partial\rho}{\partial t} = -i[H, \rho] + \kappa\mathcal{L}(\rho, a_+) + \kappa\mathcal{L}(\rho, a_-) + \gamma_S \sum_{m_S, m_P, q} \mathcal{L}(\rho, C(J_S m_S, 1q; J_P m_P)\,|S, m_S\rangle\langle P, m_P|) \\ + \gamma_D \sum_{m_D, m_P, q} \mathcal{L}(\rho, C(J_D m_D, 1q; J_P m_P)\,|D, m_D\rangle\langle P, m_P|), \end{aligned} \tag{S7}$$

where $\mathcal{L}(\rho, \mathcal{O}) \equiv 2\mathcal{O}\rho\mathcal{O}^\dagger - \mathcal{O}^\dagger\mathcal{O}\rho - \rho\mathcal{O}^\dagger\mathcal{O}$, and γ_S and γ_D are the atomic decay rates from the P state to the S and D states respectively. All the numerical simulations are carried out using the Quantum Optics toolbox for MATLAB [2].

UNCERTAINTY OF g_0

The fit shown in Fig. 3 is obtained by fitting the solution of Eq.(S7) to the data with g_0 as a fitting parameter. However uncertainties in other physical parameters such as Ω_{397} affect the resultant uncertainty of g_0. Therefore, we study the effects of the model parameters by varying their values and refitting the model to obtain the deviated g_0 and find out a change from the original value of g_0. We validate that the dependence of g_0 on the parameters is linear in the region of our interest (e.g. see Fig. S2). Through this variational analysis, we propagate the error of each parameter to that of g_0 as listed in TABLE S1. Combining all the error budgets, the uncertainty of g_0 from the uncertainties of the model parameters is determined to be 0.07 MHz. As a result, together with the fitting error of 0.07 MHz in Fig. 3, we get $g_0 = 2\pi \times (15.1 \pm 0.1)$ MHz.

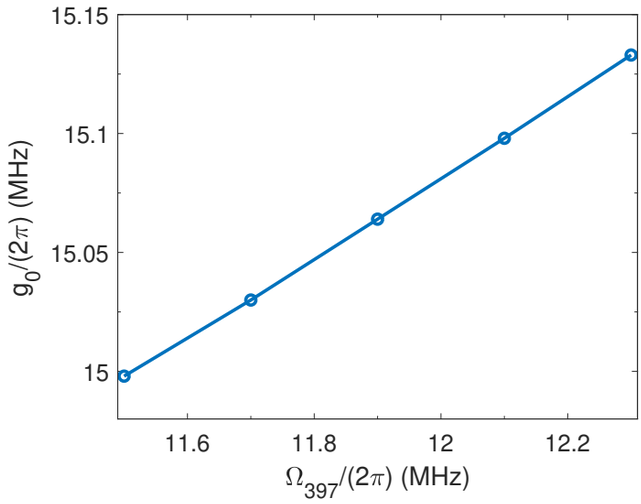

FIG. S2: Numerically obtained dependence of g_0 on Ω_{397} around $\Omega_{397} = 2\pi \times 11.9\,\mathrm{MHz}$. From the gradient, we obtain the sensitivity of g_0 on the model parameter Ω_{397}.

Parameter	Error of param.	Gradient	Error budget for g_0
Ω_{397}	$(2\pi)0.4$ MHz	0.17	(2π) 0.07 MHz
B	$\sim$0.1 Gauss	0.18 MHz/Gauss	$\sim$ (2π) 0.02 MHz
κ	$(2\pi)0.1$ MHz	0.07	(2π) 0.01 MHz

TABLE S1: Estimated errors of the model parameters in the numerical simulation and their contributions to the error of g_0 obtained through the variational analysis.

EXPECTED VALUE OF g_0 AT THE DOPPLER COOLING LIMIT

From the geometry of the cavity, the ideal value of $g_0^{(\mathrm{ideal})}$ is calculated to be $(2\pi) \times 17.3\,\mathrm{MHz}$ when the ion's positional spread is taken to be zero. In reality the ion has a finite positional spread according to the temperature, the secular frequency of the trap and the beam angle of the 393 nm laser [3]. At the Doppler cooling temperature, the positional spread along the direction of the cavity axis is calculated to be $\Delta z = 94\,\mathrm{nm}$ which corresponds to temperature of 4 mK. Note that the spread along other two directions are neglected since the spatial variations of the cavity field in these directions are negligible compared to the axial direction. From this, the expected ion-cavity coupling is deduced to be $g_0 = g_0^{(\mathrm{ideal})}\sqrt{\frac{1+\mathrm{e}^{-k^2\Delta z^2}}{2}} = 2\pi \times 15.6\,\mathrm{MHz}$ which compares well with the experimentally obtained value of $2\pi \times 15.1\,\mathrm{MHz}$.

ESTIMATION OF THE CAVITY DRIVING AMPLITUDE

For the transmission spectroscopy of Fig.4, the system Hamiltonian is modified in order to incorporate the cavity driving term:

$$H = H_0' + H_B + H_{\mathrm{drive}} + H_{\mathrm{ion-cav}}, \tag{S8}$$

with

$$H_0' = \Delta_{866} \sum_{m_D} |D, m_D\rangle\langle D, m_D| - \Delta_{866}(a_+^\dagger a_+ + a_-^\dagger a_-), \tag{S9}$$

and

$$H_{\mathrm{drive}} = E(a_+ + a_+^\dagger). \tag{S10}$$

Here we assume $\Delta_{\rm cav} = 0$.

In order to estimate the magnitude of E in (S10), we use the transmission spectra of the cavity with and without an ion. The transmission without ion serves as a reference (red trace in the inset of Fig.5). For measurements with ion, the ion is prepared in the $D_{3/2}, m_J = -3/2$ state. The presence of the ion in the cavity reduces the cavity transmission as described in detail in the main text. For the low intra-cavity photon numbers used in this publication, the main effect of the intra-cavity light is the pumping of the ion into the S-state due to incoherent scattering and thus diminishing the interaction between ion and the cavity. As E increases, the probability of incoherent scattering increases and cavity transmission asymptotically approaches to the one without the ion.

Consequently the ratio between the peak heights of the spectra with and without the ion depends on the magnitude of E as shown in Fig. S3. Using this dependence, we obtain $E = 0.032$ from the experimental data shown in Fig. 4(c).

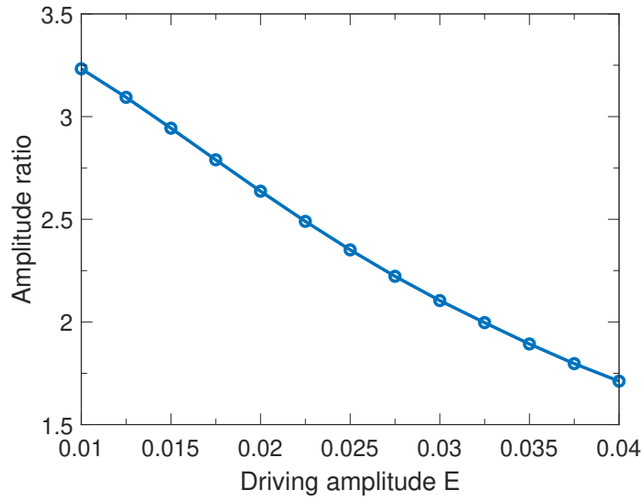

FIG. S3: The ratio of the peak heights with and without an ion in the cavity transmission spectroscopy is numerically calculated for different driving field amplitude.

PROSPECT FOR ENTANGLEMENT GENERATION BETWEEN REMOTELY TRAPPED IONS

Here we discuss one of potential applications using our strongly coupled ion-cavity system. Efficient generation of entanglement between ions held in remote traps is vital for distributed quantum computation and quantum networks [4, 5]. We consider a probabilistic scheme to create entanglement between two remote ions as depicted in Fig. S4a. Each ion is coupled to a local optical cavity and an entangled state between the ion and the cavity photon is generated:

$$|v_i\rangle = \frac{g_1|\uparrow_i\rangle|\mathrm{H}_i\rangle + g_2|\downarrow_i\rangle|\mathrm{V}_i\rangle}{\lambda}, \quad (i = 1, 2) \tag{S11}$$

where $i\,(= 1, 2)$ denotes the two different ion-cavity systems, $|\uparrow_i\rangle$ and $|\downarrow_i\rangle$ are the ion's internal states, $|\mathrm{H}_i\rangle$ and $|\mathrm{V}_i\rangle$ are the orthogonal polarization states of the cavity photon, and $\lambda = \sqrt{g_1^2 + g_2^2}$ is the normalization constant. Note that (S11) is in the same form as the *bright state* introduced in the main text and can be generated by harnessing the ion's simultaneous coupling to the degenerate polarization modes of the cavity (see Fig. S4b). The single photons generated in this way are extracted from both cavities and propagate to a non-polarizing beam splitter (NPBS). Then the outputs of the NPBS are detected in a way that different polarization components are distinguished with polarizing beam splitters and four single photon detectors (see Fig. S4a). As there are only up to two photons in the entire system, at most two of the four detectors can register photon arrivals. When the detected two photons are of different polarizations, the ionic state is projected to the following maximally entangled Bell state [6]:

$$|\Psi_{12}^{(\pm)}\rangle = \frac{1}{\sqrt{2}}(|\uparrow_1\rangle|\downarrow_2\rangle \pm |\downarrow_1\rangle|\uparrow_2\rangle). \tag{S12}$$

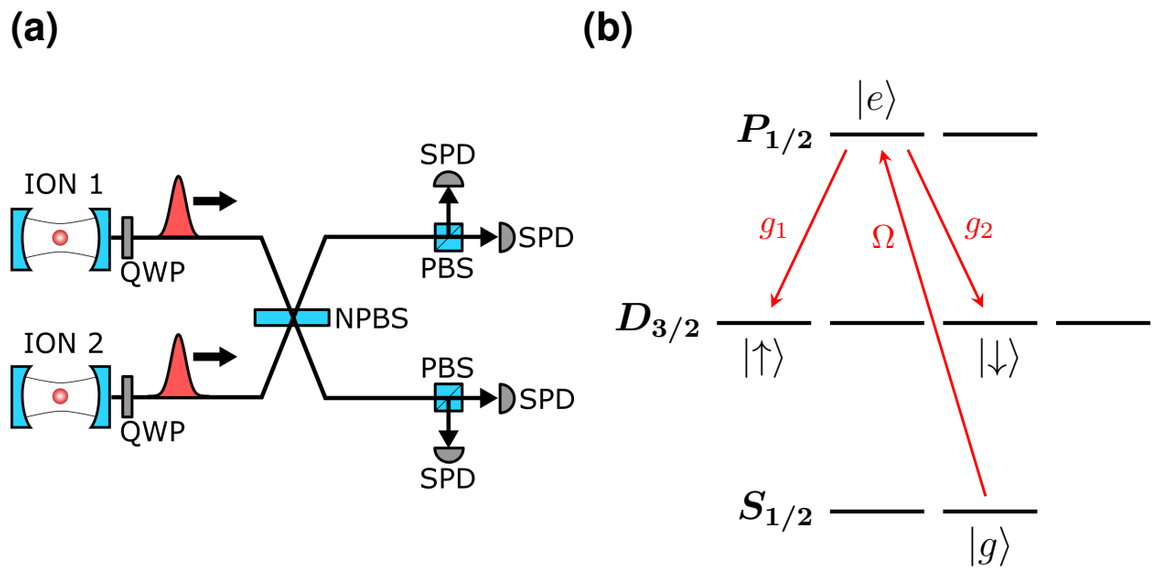

FIG. S4: (a) Schematic of a set up for heralded entanglement generation based on ion-cavity single photon sources. QWP: quarter wave plate to convert circular polarizations to linear polarizations. NPBS: non-polarizing beam splitter. PBS: polarizing beam splitter. SPD: single photon detector. (b) The energy levels and transitions used to generate the ion-photon entangled state (S11). Note that the ion in $|e\rangle$ can decay to states other than $|g\rangle$. However in those cases the ion cannot get repumped and hence such processes only contribute to the efficiency but not to the infideligy of the entanglement generation.

The probability for such detection to happen for the given input state (S11) is

$$P_{\text{Bell}} = 2\left(\frac{g_1 g_2}{g_1^2 + g_2^2}\right)^2. \tag{S13}$$

The maximally entangled states (S12) are obtained only when the photons from the two sources are identical and perfectly indistinguishable. However, in the real ion-cavity systems, the temporal waveforms of the generated single photons statistically fluctuate due to the ion's spontaneous emission during the single photon generation. Consequently the photons arriving at the NPBS can have different waveforms, leading to reduced indistinguishability. In general the resultant state heralded by photon detection is a mixed state with some non-unity fidelity ($=F_{\text{ent}}$) with the corresponding maximally entangled state (S12). This fidelity can be calculated for the given system parameters by solving a series of trace non-preserving master equations [7]. The details of the calculation can be found elsewhere [8].

We employ the energy levels of $^{40}Ca^{+}$ as shown in Fig. S4b. The ion is initialized in $|g\rangle$ and a laser pulse to drive $|g\rangle \rightarrow |e\rangle$ is applied in a certain temporal waveform. The numerical simulation is carried out using the experimentally obtained parameters: ion-cavity coupling $g = \sqrt{g_1^2 + g_2^2} = 2\pi \times 12$ MHz and $\kappa = 2\pi \times 4$ MHz. Even though the coherent dynamics between the ion and the cavity is dominant in the strong coupling regime, it is noteworthy that the ion can spontaneously decay from the excited state $|e\rangle$ back to $|g\rangle$ while the driving pulse is still present. In this case, the ion can get repumped to $|e\rangle$ and subsequently either emits a single photon into the cavity successfully, or spontaneously decays to $|g\rangle$ again to potentially initiate another repumping cycle. This process introduces ambiguity as to the timing at which the single photon is generated, comprising a main source of infidelity in the entanglement generation. As a result we need to consider an ensemble of photon waveforms impinging on the NPBS which are partially distinguishable. Fig. S5 shows the simulated waveforms of single photons. Among all the cavity emission, 87% happens without spontaneous decay (solid line), 11% happens while having spontaneous decay once (dotted line), and 2% having twice (dash-dotted line). Taking these statistics and the explicit photon waveforms into account, we calculate the fidelity of the heralded ionic state with the maximally entangled state to be 0.95 with an intra-cavity emission efficiency $\eta_{\text{emi}} = 0.82$, well suited to be a resource in distributed quantum computation [9].

In order to estimate the actual heralding rate of entanglement, not only the efficiency of the intra-cavity single photon generation but other efficiencies, such as the propagation and detection efficiencies, need to be taken into account. We estimate the relevant efficiencies as follows: The escaping efficiency of a photon out of the cavity

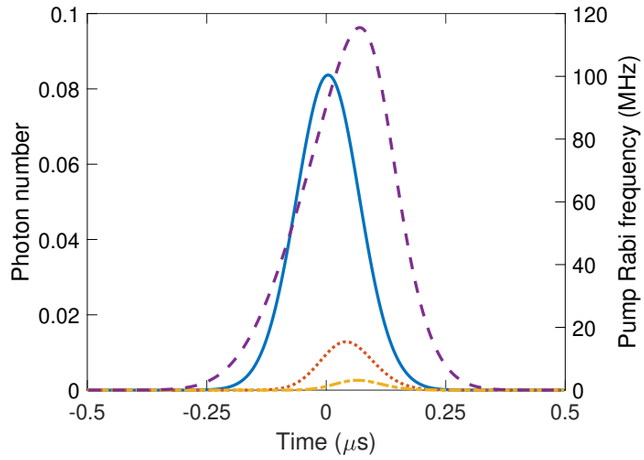

FIG. S5: The solid blue line is the simulated waveform of a single photon when the ion does not suffer spontaneous decay from $|e\rangle$ to $|g\rangle$ at all. The dotted red line is the averaged waveform of a single photon emitted after the ion decays from $|e\rangle$ to $|g\rangle$ once. The dash-dotted yellow line is the averaged waveform when the spontaneous decay happens twice before the emission of the single photon. Their pulse areas represent relative probabilities for their occurrences. The dashed purple line is the waveform of the driving pulse which is derived such that the single photon waveform becomes Gaussian which is known to minimize the effects of mode-mismatch between interfering single photons [10].

$\eta_{\rm esc} = 0.4$ where we assume total mirror transmissivity of 50 ppm and scattering/absorption loss of 75 ppm, same as the current experimental cavity. The mode matching efficiency between the cavity mode and the optical fiber mode $\eta_{\rm mm} = 0.9$, which was demonstrated in [11]. The propagation efficiency from the cavity to the detector $\eta_{\rm prop} = 0.8$ and the detector's quantum efficiency $\eta_{\rm det} = 0.9$ based on commercially available superconducting nanowire single photon detectors. Note that here we focus on entanglement of remote traps at a short distance ($\sim$ a few meters) and thus the propagation losses in the fibers are negligible. We only take the insertion loss to the beam splitters into account. Therefore the total efficiency is $\eta_{\rm tot} = \eta_{\rm emi}\eta_{\rm esc}\eta_{\rm mm}\eta_{\rm prop}\eta_{\rm det} = 0.21$. The heralding rate is given by $R_h = P_{\rm Bell}\eta_{\rm tot}^2 R_{\rm rep}$ where $R_{\rm rep}$ is the rate at which the generation of single photons is synchronously repeated at both traps. As can be seen in Fig. S5, the waveform of the single photon is contained well within 500 ns. Therefore, we conservatively estimate that $R_{\rm rep} = 500$ kHz is possible including the time needed for initializing the ion in $|g\rangle$. This is also the repetition rate used in [6]. From these figures, $R_h = 8.5$ kHz is obtained, more than three orders of magnitude improvement over the result ($= 4.5\,$Hz) demonstrated in the current state of the art in entanglment generation between remote atoms [6].

Ion-cavity systems with similar cooperativity (e.g. [12]) but lower coherent ion-cavity coupling and lower cavity decay rates can achieve similar single photon efficiencies but can only have significantly lower repetition rates ($\sim$ kHz). On the other hand ion-cavity systems with lower cooperativity (e.g.[13] ,[14]) have a significantly lower single photon efficiency. Furthermore, UV optical cavities such as [13] have high absorption/scattering losses further reducing the total efficiency. Therefore, an ion-cavity system with high cooperativity and large coherent ion-cavity coupling at an infrared wavelentgh, as presented in this paper, is best suited for entangling remote ions for quantum computing and networking. Further potential improvements on the FFPC can be foreseen as follows: In [15], a cavity finesse compatible with scattering/absorption losses of 11 ppm per fiber mirror is demonstrated. Assuming the internal losses of our cavity reduced to the same level, the escaping efficiency is increased to $\eta_{\rm esc} = 0.7$. The radius of curvature ($=R_c$) of the fiber mirror can be reduced without increasing diffraction losses by employing the technique introduced in [16]. With $R_c = 300\,\mu$m and the cavity length of $300\,\mu$m, $g = 2\pi \times 20$ MHz can be obtained. It results in a single photon emission efficiency $\eta_{\rm emi} = 0.9$ and entanglement fidelity $F_{\rm ent} = 0.98$. Combining these improvements we foresee the heralding entanglment rate to become 30 kHz at $R_{\rm rep} = 500$ kHz.

[1] H. Takahashi, J. Morphew, F. Oručević, A. Noguchi, E. Kassa, and M. Keller, Opt. Express **22**, 31317 (2014).
[2] S. M. Tan, Journal of Optics B: Quantum and Semiclassical Optics **1**, 424 (1999).
[3] W. M. Itano and D. Wineland, Physical Review A **25**, 35 (1982).

[4] C. Monroe, R. Raussendorf, A. Ruthven, K. R. Brown, P. Maunz, L.-M. Duan, and J. Kim, Phys. Rev. A **89**, 022317 (2014).
[5] H. Briegel, W. Dür, J. Cirac, and P. Zoller, Physical Review Letters **81**, 5932 (1998).
[6] D. Hucul, I. Inlek, G. Vittorini, C. Crocker, S. Debnath, S. Clark, and C. Monroe, Nature Physics **11**, 37 (2015).
[7] H. Goto, S. Mizukami, Y. Tokunaga, and T. Aoki, Phys. Rev. A **99**, 053843 (2019).
[8] H. Takahashi *et. al.*, to be published.
[9] W. Dür and H. J. Briegel, Physical Review Letters **90**, 4 (2003), 0210069 .
[10] G. S. Vasilev, D. Ljunggren, and A. Kuhn, New Journal of Physics **12**, 063024 (2010).
[11] G. K. Gulati, H. Takahashi, N. Podoliak, P. Horak, and M. Keller, Scientific Reports **7**, 5556 (2017).
[12] A. Stute, B. Casabone, P. Schindler, T. Monz, P. Schmidt, B. Brandstätter, T. Northup, and R. Blatt, Nature **485**, 482 (2012).
[13] T. Ballance, H. Meyer, P. Kobel, K. Ott, J. Reichel, and M. Köhl, Physical Review A **95**, 033812 (2017).
[14] T. Walker, K. Miyanishi, R. Ikuta, H. Takahashi, S. V. Kashanian, Y. Tsujimoto, K. Hayasaka, T. Yamamoto, N. Imoto, and M. Keller, Physical Review Letters **120**, 203601 (2018).
[15] D. Hunger, C. Deutsch, R. J. Barbour, R. J. Warburton, and J. Reichel, AIP Advances **2**, 012119 (2012).
[16] K. Ott, S. Garcia, R. Kohlhaas, K. Schüppert, P. Rosenbusch, R. Long, and J. Reichel, Optics Express **24**, 9839 (2016).

Chapter 5

Enhanced ion-cavity coupling through cavity cooling in the strong coupling regime

Up until this point, all the cooling of the ion was done through Doppler cooling. In the supplementary material in the previous publication we calculated that the coherent coupling at the Doppler cooling limit is 15.6 MHz. There is a discrepancy between this value and the experimentally obtained value from the previous chapter, 15.1 MHz. The main reason for that is that the ion is not being optimally cooled along the cavity axis. The cooling beams enter the trap with about 8 degree angle with the horizontal plane of the trap (perpendicular to the cavity axis). Therefore, the component of Doppler cooling along the cavity axis is small compared to the other directions. This means that the temperature of the ion and thus its localisation along the cavity axis is worse than the other directions. Thus, the coherent coupling measured is less than the optimal because of the averaging of the coupling along the cavity axis due to the delocalisation of the ion. In this chapter/publication we show how we can use a cavity induced cooling technique to increase the localisation of the ion. Using this technique we measure the coherent coupling again and we show that it is higher from the one measured using just Doppler cooling.

To understand how cavity cooling works I will give a brief summary of the theory, which is explained in more detail in [82]. We consider a two-level ion (ground state given by $|g\rangle$ and excited state given $|e\rangle$) with transition frequency ω_0, that interacts with a cavity mode of frequency ω. This system is described by the master equation

$$\left(\frac{d}{dt}\right)\hat{\rho} = -i[\hat{H}_{mot} + \hat{H}_i + \hat{H}_{int}, \hat{\rho}] + \mathcal{L}_f(\hat{\rho}) + \mathcal{L}_a(\hat{\rho}) \tag{5.1}$$

In the master equation, $\hat{H}_{mot}$ is the Hamiltonian for the centre-of-mass motion of the ion, and it is given by

$$\hat{H}_{mot} = \frac{\hat{P}^2}{2m} + \frac{1}{2}m\omega_{sec}^2\hat{R}^2 \tag{5.2}$$

with $\hat{R}$ being the position operator, $\hat{P}$ the momentum operator, m the mass of the ion and ω_{Sec} the secular frequency. The internal energy Hamiltonian of the ion is given by:

$$\hat{H}_i = \delta\hat{\sigma}_{ee} \tag{5.3}$$

where $\delta = \omega - \omega_0$ and $\hat{\sigma}_{ee} = |e\rangle\langle e|$. The ion-cavity dipole interaction Hamiltonian is given by

$$\hat{H}_{int} = g \cdot \cos\Big(k\hat{R} + \psi\Big)(\hat{\sigma}_{ge}\hat{a} + \hat{a}^{\dagger}\hat{\sigma}_{eg}) \tag{5.4}$$

where $\hat{a}^{\dagger}$ and $\hat{a}$ are the creation and annihilation operators of the cavity, $\hat{\sigma}_{ge/eg}$ the projection operators, g the ion-cavity coupling, k the wavevector of the cavity and ψ the relative position of the ion in the cavity mode standing wave. The last two terms in 5.1 are the losses of the system. $\mathcal{L}_f(\hat{\rho})$ corresponds to the cavity decay losses

$$\mathcal{L}_f(\hat{\rho}) = \kappa(N+1)(2\hat{a}\hat{\rho}\hat{a}^{\dagger} - \hat{a}^{\dagger}\hat{a}\hat{\rho} - \hat{\rho}\hat{a}^{\dagger}\hat{a}) + \kappa N(2\hat{a}^{\dagger}\hat{\rho}\hat{a} - \hat{a}\hat{a}^{\dagger}\hat{\rho} - \hat{\rho}\hat{a}\hat{a}^{\dagger}) \tag{5.5}$$

where κ is the cavity decay rate and N the mean photon number. $\mathcal{L}_a(\hat{\rho})$ corresponds to the spontaneous emission losses

$$\mathcal{L}_a(\hat{\rho}) = \left(\frac{\Gamma}{2}\right)(2\hat{\sigma}_{eg}\tilde{\rho}\hat{\sigma}_{ge} - \hat{\sigma}_{ge}\hat{\sigma}_{eg}\hat{\rho} - \hat{\rho}\hat{\sigma}_{ge}\hat{\sigma}_{eg}) \tag{5.6}$$

where Γ is the linewidth of the atomic transition and $\tilde{\rho}$ includes the momentum transfer associated with the emission of a photon with momentum $\hbar k$.

From the above definitions, we observe that the internal dynamics of the system are coupled with the external dynamics, motion of the ion, through the interaction Hamiltonian and the spontaneous emission term. Assuming that we operate in the Lamb-Dicke limit and the rate of cooling is slower than the internal dynamics, we can derive a master equation for the reduced density operator $\hat{\mu} = \mathrm{Tr}_{int}(\hat{\rho})$. The reduced density operator $\hat{\mu}$ corresponds to the external degrees of freedom only, and is produced by taking the trace over the internal degrees of freedom.

$$\left(\frac{d}{dt}\right)\hat{\mu} = -i\omega_{sec}[\hat{b}^{\dagger}\hat{b}, \hat{\mu}] + \{\{[S(\omega_{sec}) + D](\hat{b}\hat{\mu}\hat{b}^{\dagger} - \hat{b}^{\dagger}\hat{b}\hat{\mu}) + [S(-\omega_{sec}) + D](\hat{b}^{\dagger}\hat{\mu}\hat{b} - \hat{b}\hat{b}^{\dagger}\hat{\mu})\} + h.c\} \tag{5.7}$$

The creation and annihilation operators $\hat{b}^{\dagger}$ and $\hat{b}$ of the harmonic oscillator are defined from $\hat{R}$ and $\hat{P}$.

$$\hat{R} = \frac{1}{\sqrt{2m\omega_{sec}}}(\hat{b}^{\dagger} + \hat{b}) \tag{5.8}$$

$$\hat{P} = i\sqrt{\frac{m\omega_{sec}}{2}}(\hat{b}^{\dagger} - \hat{b}) \tag{5.9}$$

The function $\mathcal{D}$ is the diffusion coefficient due to spontaneous emission from the excited atomic level. $S(\omega_{sec})$ is the gradient of the dipole interaction at $R = 0$

$$\mathcal{D} = \frac{1}{5}\eta^2\Gamma\langle\hat{\sigma}_{ge}\hat{\sigma}_{eg}\rangle_{ss} \tag{5.10}$$

$$S(\omega_{sec}) = \eta^2[g\sin(\psi)]\int_0^{\infty} dt\,\exp(i\omega_{sec}t)\langle[\hat{\sigma}_{ge}(t)\hat{a}(t) + \hat{a}^{\dagger}(t)\hat{\sigma}_{eg}(t)] \times [\hat{\sigma}_{ge}(0)\hat{a}(0) + \hat{a}^{\dagger}(0)\hat{\sigma}_{eg}(0)]\rangle_{ss} \tag{5.11}$$

where η is the Lamb-Dicke parameter. These quantities are calculated from the internal master equation, for an ion at rest at the trap centre (see [82] for more details).

$$\left(\frac{d}{dt}\right)\hat{\rho}_{int} = -i[\hat{H}_{JC}, \hat{\rho}_{int}] + \mathcal{L}_f(\hat{\rho}_{int}) + \mathcal{L}_a(\hat{\rho}_{int}) \tag{5.12}$$

where $\hat{H}_{JC}$ is the well known Jaynes-Cummings Hamiltonian. From the master equation above, we observe that the Jaynes-Cummings energy structure enters the cooling dynamics through the $S(\omega_{sec})$ function.

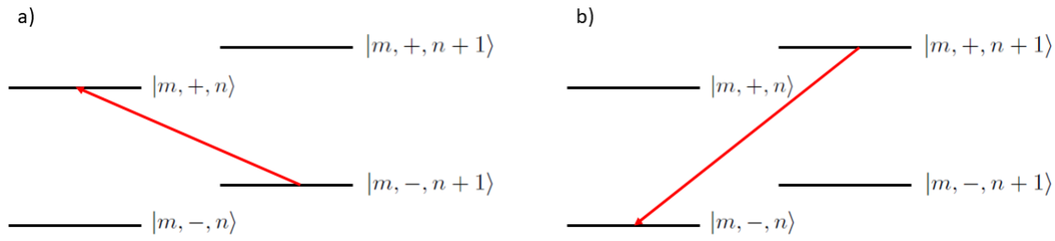

Figure 5.1: Diagrammatic representation of the cooling processes.

From the master equation 5.7, we can derive the rate equation for the populations $p_n = \langle n| \mu |n\rangle_b$, where $|n\rangle_b$ are the state basis of the harmonic oscillatory motion.

$$\left(\frac{d}{dt}\right)p_n = (n+1)A_- p_{n+1} - [(n+1)A_+ + nA_-]p_n + nA_+ p_{n-1} \tag{5.13}$$

$A_\pm$ are the transition rates given by $A_\pm = 2Re[S(\mp\omega_{sec}) + \mathcal{D}]$. The equation of motion for the mean value $\langle n\rangle_b$ is given by

$$\left(\frac{d}{dt}\right)\langle n\rangle_b = -(A_- - A_+)\langle n\rangle_b + A_+ \tag{5.14}$$

where $W = A_- - A_+$ is the cooling rate. The steady state vibrational energy is given by

$$E_{ss} = \omega_{sec}(\langle n\rangle_b^{ss} + 1/2) = \omega_{sec}\left(\frac{A_+}{A_- - A_+} + \frac{1}{2}\right) \tag{5.15}$$

The basis states of the whole system includes both the internal and external degrees of freedom. They consist of the tensor product of the dressed states ($|m,\pm\rangle$, see Theory section for derivation) with the Fock state $|n\rangle_b$ of the atomic motion in the harmonic potential.

$$|m,\pm,n\rangle = |m,\pm\rangle \otimes |n\rangle_b\,, \qquad (n = 0,1,...) \tag{5.16}$$

The master equation 5.13 for the vibrational level populations shows how the trap dynamics work for processes where the oscillator quantum number n increases or decreases by one. To fully understand the cavity cooling mechanism, we need to combine this master equation with specific examples of cooling processes. These are depicted in Figure 5.1. In these processes the system makes a transition from $|m,\pm,n+1\rangle$ to $|m,\mp,n\rangle$. Afterwards, the population gets redistributed between dressed states with fixed $|n\rangle_b$, through a combination of spontaneous decay or cavity losses.

In the strong coupling limit ($g\cos(\psi) \gg \kappa,\Gamma$) we can obtain an approximate solution for the internal master equation. Using this solution we can show that the temperature of the steady state for the cooling process is given by [82]

$$\langle n\rangle_b^{ss} = \frac{P_m^+}{P_m^- - P_m^+} \tag{5.17}$$

where P_m^- and P_m^+ are the populations of the dressed states $|m,-\rangle$ and $|m,+\rangle$ respectively. Here the steady temperature is given in terms of the mean number $\langle n\rangle_b^{ss} = \langle \hat{b}^\dagger \hat{b}\rangle_{ss}$. From the steady temperature equation, the maximum cooling is expected when $P_m^- > P_m^+$. The spontaneous emission out of the sides of the cavity increases the population of the dressed state $|m,-\rangle$ relative to $|m,+\rangle$, leading to cavity cooling ($P_m^- > P_m^+$). In addition, from

the numerical solutions of the internal master equation in [82], we observe that for strong coupling, cavity cooling appears for blue detunings of the cavity frequency from the transition frequency. This feature is similar to that of a trapped ion in a laser standing wave for large Rabi frequencies [83] [84].

Since we trap a calcium ion in our system, we need to examine cavity cooling in a three level model. We consider a three-level system with states S, P, D, as presented in Figure 2.6 in Chapter 2. The reduced density operator $\hat{\mu}$ remains the same in the three-level model, since it corresponds to the external degrees of freedom only. The function $S(\omega_{sec})$ has the same form as 5.11, with the only difference being that the cavity is now tuned across the $P \leftrightarrow D$ transition, so the atomic raising and lowering operators are given by $\hat{\sigma}_{PD} = |P\rangle \langle D|$ and $\hat{\sigma}_{DP} = |D\rangle \langle P|$ respectively. The function $\mathcal{D}$ is defined as

$$\mathcal{D} = \frac{1}{5}\eta^2(\gamma_{PS}\hat{\sigma}_{PP} + 2\gamma_{eff}\hat{\sigma}_{DD}) \tag{5.18}$$

where $\gamma_{eff} = \gamma_{PS} + \gamma_{PD}$ and we made the assumption $\eta_P = \eta_D = \eta$. The extra term in the function comes from repumping the population from the D-state to the S-state. As stated before, these functions are calculated using the master equation 5.12. Therefore, we need to redefine it for the three-level model. The Jaynes-Cummings Hamiltonian for the three level model was derived in Chapter 2. The cavity decay loss term $\mathcal{L}_f(\hat{\rho}_{int})$ is the same as the one for the two-level system (eq.5.5). The spontaneous decay loss term is given by

$$\mathcal{L}_a(\hat{\rho}) = \left(\frac{\gamma_{PS}}{2}\right)(2\hat{\sigma}_{SP}\tilde{\rho}\hat{\sigma}_{PS} - \hat{\sigma}_{PP}\hat{\rho} - \hat{\rho}\hat{\sigma}_{PP}) + \gamma_{eff}(2\hat{\sigma}_{SD}\tilde{\rho}\hat{\sigma}_{DS} - \hat{\sigma}_{DD}\hat{\rho} - \hat{\rho}\hat{\sigma}_{DD}) \tag{5.19}$$

Having showed $S(\omega_{sec})$ and $\mathcal{D}$ for the three-level model, calculating the transition rates A_-, A_+ and steady state temperature follows the same method as the two-level model.

One thing to note, is that we have not included in the model the interaction with the Doppler cooling field. The reason for this is, that in our system the Doppler cooling beam enters almost perpendicular to the cavity axis, so its effect is insignificant.

Using the cavity cooling scheme, our aim was to implement it experimentally in our system to increase the localisation of the ion. To optimise the parameters in our system for maximal cavity cooling, we need an indication of the localisation of the ion, as we vary the parameters (like cavity detuning). For this reason, we measure the standing wave pattern using the cavity emission from the ion. The ion was shifted using a voltage applied to the inner electrode between the node, where cavity cooling was maximum, to the points along the standing wave, where we collected single photons through a Raman transition. The visibility of this pattern gives us an indication on the increase of localisation of the ion. By measuring the visibility we optimised the parameters for cavity cooling, like the cavity detuning, the pulse length of the beams and the Rabi frequency of the cooling and probing beams. To fit the visibility scans we used a simulation based on the theory explained in [82].

After optimising the cavity cooling parameters, we set to measure the coupling with and without cavity cooling. We have repeated the method explained in the previous chapter and measured the coherent coupling to be $2\pi \times (15.2 \pm 0.1)$ MHz with Doppler cooling. Next we incorporated a cavity cooling window in the pulse sequence, where the ion was cavity

cooled in the node and then transferred adiabatically to the antinode, where the ion-cavity coupling is maximal. Using the same method as the one for Doppler cooling, we extracted a coherent coupling of $2\pi \times (16.7 \pm 0.1)$ MHz. The maximum theoretical value for coherent coupling in our system is $2\pi \times (17.3 \pm 0.1)$ MHz, meaning we have increased the measured ion-cavity coupling from 87% of the theoretically possible ion-cavity coupling with Doppler cooling, to 97% with the introduction of cavity cooling. Furthermore, with the addition of cavity cooling the localisation of the ion decreased from 110 nm to 55 nm and the temperature from 8.5 mK to 2.1 mK.

One of the main reasons why the coherent coupling is less than the theoretical value, is due to the fact that during the cavity cooling step the ion is transposed to the node of the standing wave, which is about 200 nm away from the minimum micromotion point. Therefore, there is a significant amount of micromotion during cavity cooling, which leads to delocalisation of the ion.

In this publication I have contributed in designing the experiment, setting up the electronics and software for the transpose of the ion between node and antinode. I have taken part in the acquisition and analysis of the data, as well as helping setting up the simulations for the fitting of the visibility scans. Finally, I have contributed in the writing of the publication and the production of graphs and figures.

Enhanced ion-cavity coupling through cavity cooling in the strong coupling regime

Costas Christoforou*[1], Corentin Pignot[1], Ezra Kassa[2], Hiroki Takahashi[3,4], and Matthias Keller[1]

[1] Department of Physics and Astronomy, University of Sussex, Brighton, BN1 9QH, United Kingdom
[2] Clarendon Laboratory, University of Oxford, Parks Road, Oxford OX1 3PU, United Kingdom
[3]Quantum Information and Quantum Biology Division, Institute for Open and Transdisciplinary Research Initiatives, Osaka University, 1-3 Machikaneyama, Toyonaka, Osaka 560-8531, Japan
[4]Experimental Quantum Information Physics Unit, Okinawa Institute of Science and Technology Graduate University, 1919-1 Tancha, Onna, Kunigami, Okinawa 904-0495, Japan

March 4, 2020

Abstract

Incorporating optical cavities in ion traps is becoming increasingly important in the development of photonic quantum networks. However, the presence of the cavity can hamper efficient laser cooling of ions because of geometric constraints that the cavity imposes and an unfavourable Purcell effect that can modify the cooling dynamics substantially. On the other hand the coupling of the ion to the cavity can also be exploited to provide a mechanism to efficiently cool the ion. In this paper we demonstrate experimentally how cavity cooling can be implemented to improve the localisation of the ion and thus its coupling to the cavity. By using cavity cooling we obtain an enhanced ion-cavity coupling of $2\pi \times (16.7 \pm 0.1)$ MHz, compared with $2\pi \times (15.2 \pm 0.1)$ MHz when using only Doppler cooling.

1 Introduction

Incorporating optical cavities into ion traps merges the outstanding properties of ions such as long coherence times [1] and high-fidelity quantum control [2] with the means to deterministically transfer the quantum state between ions and light at the single quantum level. Exploiting this superior control, cavity induced transparency [3], the mapping of the quantum state between ions and photons [4], ion-photon entanglement [5] and heralded ion-ion entanglement [6] have been demonstrated. Ion-cavity systems enable distributed architectures for large-scale quantum information processing as well as device-independent quantum key distribution. Instrumental to these applications is the ability to localise ions in optical cavities [7–10] and to strongly couple single ions to an optical cavity [3].

While the optical cavity is crucial to facilitate the ion-light interaction, its presence can interfere with the manipulation of the ion. In particular laser cooling can be hindered by the Purcell effect [11]. This can be circumvented by choosing cooling transitions within the ion that are not affected by the cavity [3]. Alternatively, the ion-cavity interaction can be exploited to improve the cooling process.

*Email: C.Christoforou@sussex.ac.uk

Cooling of trapped ions by using their interaction with an optical cavity has been theoretically studied extensively in the weak binding regime [12–16], where the transition linewidth is larger than the secular frequencies. Cavity sideband cooling in the strong binding regime has been studied both theoretically [17] and experimentally [18, 19].

Here we demonstrate that cavity cooling in the weak binding regime can be employed to improve the localisation of a single ion in an optical cavity and to enhance the ion-cavity coupling. This paper is structured as follows. In section 2 we present the setup of our experiment. Section 3 describes the implementation of cavity cooling and finally section 4 presents the measurement of the improved ion-cavity coupling.

2 Setup

The trap used in this experiment is an endcap-style radio frequency (rf) Paul trap with an integrated fibre Fabry-Pérot cavity (FFPC) as described in [11]. The trapping structure consists of two electrode assemblies made from concentric cylindrical stainless steel tubes (Figure 1(a)). An rf voltage at 19.55 MHz is applied to the outer electrodes whilst the inner electrodes are held at rf ground. This generates a trapping pseudopotential with a global minimum between the two electrode assemblies. In addition, the trap has four radial electrodes as shown in Figure 1(a). Two of them deliver dc voltages to compensate excess micromotion in the radial plane whilst the other two radial electrodes carry rf voltages synchronous with the trap drive to move the potential minimum and optimize the ion-cavity coupling [10]. The axial micromotion component is compensated by dc voltages applied to the inner electrodes of the endcap trap. The axial secular frequency for these measurements is measured to be $2\pi \times 2.73$ MHz.

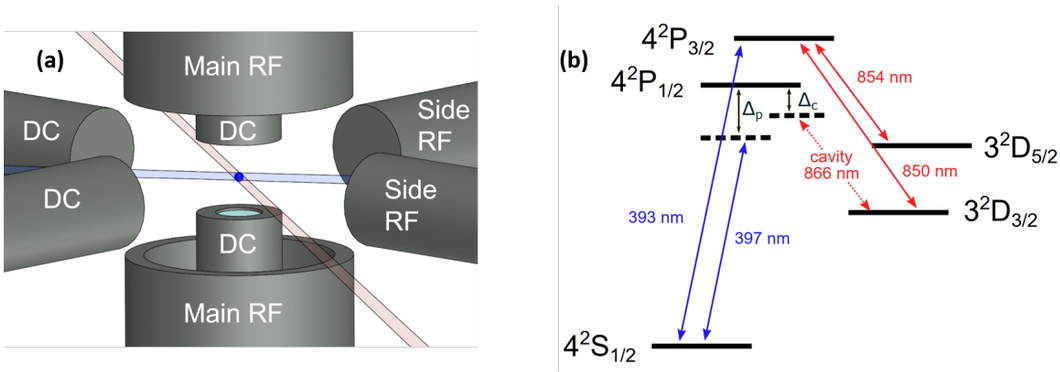

Figure 1: (a) A drawing of the ion trap. Outer axial electrodes provide the main rf signal. Two axial and two radial dc electrodes are used for micromotion compensation. Additionally, two electrodes in the radial plane carry rf signals to optimise the ion's position overlap with the cavity mode. The cavity fibres are inserted into the inner electrodes. (b) Relevant energy levels of $^{40}Ca^+$ in the form of a lambda-type system where single photons are generated at a wavelength of 866 nm via a cavity-assisted Raman transition from the $S_{1/2}$ to the $D_{3/2}$ state. The ion is Doppler cooled on the $S_{1/2} \leftrightarrow P_{1/2}$ and $S_{1/2} \leftrightarrow P_{3/2}$ transitions. Lasers at 850 nm and 854 nm are necessary to repump from the metastable D states. The fibre cavity is tuned to the $P_{1/2} \leftrightarrow D_{3/2}$ transition.

The fibres that carry the cavity mirrors are inserted into the inner electrodes. The end facets of the fibres were machined using a laser ablation technique [20] and coated with high reflective coatings. An FFPC is then formed along the axis of the trap. The input of the cavity is a single-mode fibre whilst the output is a multi-mode fibre for high collection efficiency of the cavity emission. The length of the cavity is stabilised using the Pound-Drever-Hall technique with a laser at a wavelength of 897 nm,

which does not interact with the ion. This laser is injected into the cavity through the single-mode input fiber and is, in turn, stabilised to a reference laser via a transfer cavity [21]. The cavity length is 370 μm, providing a small cavity mode volume, with a theoretical maximum ion-cavity coupling of $2\pi\times$ 17.3 MHz. We measure a cavity linewidth at the ion's transition wavelength at 866 nm of $2\pi \times (8.2 \pm 0.1)$ MHz and a cavity finesse of 50000.

Figure 1 (b) shows the relevant energy levels of the $^{40}Ca^{+}$ ion used in the experiment. The ion is Doppler cooled on the $S_{1/2} \leftrightarrow P_{1/2}$ and $S_{1/2} \leftrightarrow P_{3/2}$ transitions and the population in the $D_{3/2}$ and $D_{5/2}$ states is repumped with lasers resonant with the $D_{3/2} \leftrightarrow P_{3/2}$ and $D_{5/2} \leftrightarrow P_{3/2}$ transitions. The cavity length is tuned such that the cavity frequency is detuned by Δ_c from the $P_{1/2} \leftrightarrow D_{3/2}$ transition. Single photons are generated by a cavity-assisted Raman transition from the $S_{1/2}$ to the $D_{3/2}$ state. The decay rate of the $P_{1/2}$ state is $\gamma = 2\pi \times 11.5$ MHz.

In order to optimise the ion's axial overlap with the standing wave pattern of the longitudinal cavity mode, the ion is translated by applying a small dc voltage on the inner axial electrodes. Although applying an rf-potential to the inner electrodes instead would be preferable [10], it is difficult to rapidly modulate the axial rf voltages on the inner electrodes while simultaneously taking into account their interference with the rf potentials on the radial electrodes due to their mutual capacitive couplings. The ion is translated by applying a positive voltage to one electrode and the corresponding negative voltage to the opposite electrode.

While the coherent coupling is optimal at the antinode of the cavity field, the emission of the ion into the mode results in heating of the ion's motion along the cavity axis. For optimal axial cavity cooling, the ion's position must be moved to the node of the cavity field [22]. To probe the ion when it is maximally coupled to the cavity while still benefiting from efficient cavity cooling, the ion must be moved from the node, where it is cooled, to the antinode where it is probed. For this purpose, a dual channel arbitrary function generator (DAFG) provides voltages to the upper and lower electrodes to shuttle the ion. In this case we avoid introducing a static quadrupole by applying the same signal to the two inner electrodes but with an opposite sign. The ion is transferred adiabatically in order to avoid motional excitation. To this end, the signal applied to the rf ground electrodes follows a Blackman-Nuttal window (BNW) shape, the amplitude of which can be tuned to precisely shuttle the ion from a node to any desired point in the standing wave (Figure 2). The shuttling voltage is summed with the dc micromotion compensation voltage and applied to the inner electrodes. Low pass filters are used to reduce electrical noise from the summing amplifier and block the rf signal coming from the trap. An example of the shape of the shuttling signal can be seen in Figure 3.

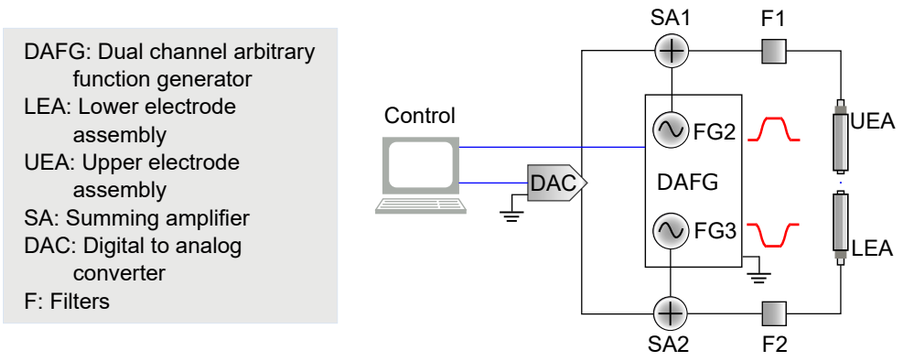

Figure 2: Schematic of the electrical setup. A DAFG provides the necessary voltages to shuttle the ion from the node to the antinode. These voltages are summed to dc voltages provided by a DAC used for the excess micromotion compensation. The total voltages are applied to the inner electrodes, shuttling the ion along the cavity axis.

3 Cavity Cooling Implementation

For cavity cooling, a laser on the $S_{1/2} \leftrightarrow P_{1/2}$ transition (pump laser) is tuned close to Raman resonance with the cavity on the $P_{1/2} \leftrightarrow D_{3/2}$ transition. Simultaneously applying lasers on the $D_{3/2} \leftrightarrow P_{3/2}$ and $D_{5/2} \leftrightarrow P_{3/2}$ transitions provides re-pumping of the ion back into the $S_{1/2}$ state, completing the cycle for continuous emission of photons into the cavity. The laser on the $S_{1/2} \leftrightarrow P_{1/2}$ transition is red-detuned with respect to the atomic resonance and hence provides Doppler cooling. However, due to the almost perpendicular alignment of the laser with respect to the cavity axis, Doppler cooling along the cavity axis is inefficient.

The cavity, together with the pump laser, forms a Raman transition between the $S_{1/2}$ and the $D_{3/2}$ states. When the ion is moved to a node of the cavity field, this Raman transition couples not only the internal state of the ion but also to the ion's axial motion [22]. Tuning the cavity blue with respect to the Raman resonance leads to a net reduction of the motional excitation of the ion, similar to Raman sideband cooling. Hence, the emission of a cavity photon leads to a reduction in the motional state excitation of the ion [12]. In order to measure the improvement of the ion's localisation due to the cavity cooling process we use the standing wave pattern measured by the cavity emission from the ion, similarly to [7]. Increase in the visibility indicates an increase in the ion's localisation.

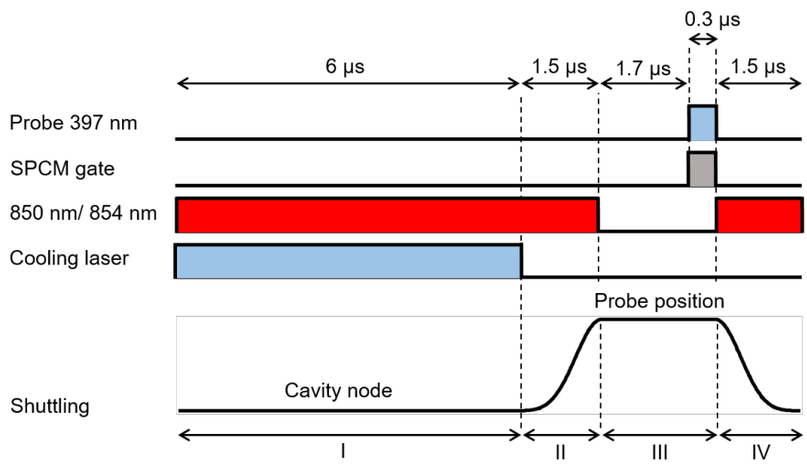

Figure 3: Laser pulses and shuttling voltage pulse of the experimental sequence. (I) Cavity cooling of the ion at the node. (II) Adiabatic shuttling of the ion to the new position and state preparation to the $4^2S_{1/2}$ state. (III) Single photon emission in the cavity by driving the Raman transition. Photons are detected by a single-photon counting module (SPCM) connected to the output of the fibre cavity. (IV) Adiabatic return of the ion to the node.

To map the standing wave pattern the following experimental sequence is applied (Figure 3). The ion is initially placed at the node of the cavity mode and the lasers on the $S_{1/2} \leftrightarrow P_{1/2}$, $D_{3/2} \leftrightarrow P_{3/2}$ and $D_{5/2} \leftrightarrow P_{3/2}$ transitions are applied. The cavity is blue-detuned relative to the nominal Raman resonance to facilitate cavity cooling. After the cooling period the laser on the $S_{1/2} \leftrightarrow P_{1/2}$ transition is extinguished to prepare the ion in the $S_{1/2}$ state, and then the ion is adiabatically shuttled to the new position. At the new position a probe laser produces a single photon in the cavity using a cavity-assisted Raman resonance. The cavity emission is recorded with a single-photon detector that is gated during the probe laser pulse. There is a 1.7 μs delay before the single photon detection in order to eliminate the effect of transient voltages in the shuttling process. The ion is probed for 300 ns. The sequence is concluded by adiabatically shuttling the ion back to the node of the cavity field while repumping with the lasers on the $D_{3/2} \leftrightarrow P_{3/2}$ and $D_{5/2} \leftrightarrow P_{3/2}$ transitions. This sequence operates

at a rate of 91 kHz. Scanning the final position of the ion after cooling, by varying the amplitude of the shuttling pulse, provides the position-dependent photon emission probability. The sequence was repeated 180000 times at each final position and the errors were extracted from the variations between the measurements.

In order to optimise the cavity cooling process, the relevant parameters (cavity detuning, length of periods I - IV (see Figure 3), cooling beam and probing beam Rabi frequencies) are individually varied. We use the standing wave scans as an indicator for the cavity cooling efficiency. The higher the visibility the more efficient the cavity cooling is. Figure 4 shows the fitted final standing wave scan (blue trace), after all the parameters were optimised. The best periods for cooling, shuttling and probing the ion can be seen in Figure 3. The Rabi frequencies are $2\pi\times14.0$ MHz for the cooling 397 nm beam and $2\pi\times11.8$ MHz for the probing 397 nm beam. In addition, for optimal cavity cooling the cavity is blue-detuned 7.0 MHz from the nominal Raman resonance (Δ_p). In the same figure we plot a fitted standing wave scan (red trace) where, instead of cavity cooling, during the same period the ion is Doppler cooled on the $S_{1/2} \leftrightarrow P_{3/2}$ transition, so the cavity does not influence the Doppler cooling process. The 393 nm laser on the $S_{1/2} \leftrightarrow P_{3/2}$ transition has the same angle to the cavity axis as the 397 nm cooling laser and has a similar Doppler cooling efficiency. From Figure 4 we can see the improvement that cavity cooling has on the visibility and thus the localisation of the ion. The standing wave pattern measurements are normalised to the maximum emission rate. For Doppler cooling (red trace) the signal to noise ratio was low, because of the delocalisation of the ion due to inefficient cooling, which resulted in big error bars.

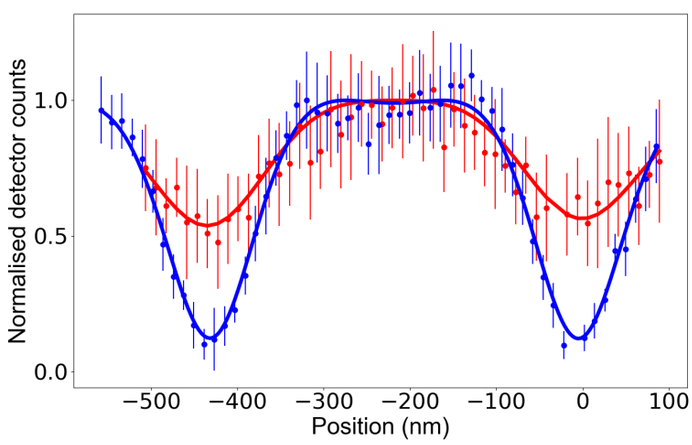

Figure 4: Cavity emission for different ion positions with and without cavity cooling. The solid lines are fits to the measured data. The red line is a trace with Doppler cooling (no cavity cooling) and the blue scan a trace with cavity cooling. The 397 nm cooling laser is detuned -10 MHz from the atomic resonance. The distance between two adjacent nodes is 433 nm. The error bars represent the statistical mean standard errors.

In contrast to [7], the pattern is not sinusoidal but consists of wide plateau-like structures at the antinodes. This structure is a result of the strong ion-cavity coupling in the setup. For weak ion-cavity coupling the single photon emission efficiency increases quadratically with coupling [23]. However, for strong coupling, the emission probability saturates as the maximal efficiency is reached for given pump laser parameters. This is clearly visible in Fig 4 (blue trace). If the ion is delocalised due to its thermal motion and hence the effective coherent coupling is reduced, the plateau structure is less pronounced (see red trace in Fig 4).

To fit the measurement, we first convert the position of the ion to the local coherent coupling using

the sinusoidal longitudinal mode pattern. We then convert the local coherent coupling into the expected cavity emission, by numerically solving a master equation of the ion coupled to a bimodal cavity for the given laser parameters. The simulation includes all relevant eight Zeeman sub-levels. We fit the scaling on the x-axis (position) and y-axis (counts), and also keep the localisation due to thermal motion and micromotion minimum offset (x_0) as free parameters, where x_0 is the ion's distance from the rf centre of the trap. The effect of the thermal motion is well described by a Gaussian position distribution (see [7]). To approximate the effect of micromotion, we use a Gaussian position distribution with a width given by $\Delta x = \frac{q}{2}x_0$ with q being the trapping q-parameter. Even though this is a coarse approximation and generally underestimates the delocalisation due to micromotion, the agreement with the measurement is good.

4 Cavity Coupling Strength Measurement

With cavity cooling we can improve the localisation of the ion along the cavity axis, which means that a stronger ion-cavity coupling can be achieved. To quantify the increase of the ion-cavity coupling, we measure it with and without cavity cooling using the method described in [3]. The coupling of the ion to the cavity has the effect of shifting the Raman resonance condition by an amount dependent on the coupling. An example of this effect is shown in Figure 5. In this case the cavity emission is measured as the cavity is scanned across the Raman resonance while the probe detuning is fixed at Δ_p = -10 MHz. The Raman resonance is expected at the condition where the cavity detuning is the same as the probe detuning $\Delta_p = \Delta_c$, but instead it has been shifted by an amount δ, as can be seen in Figure 5.

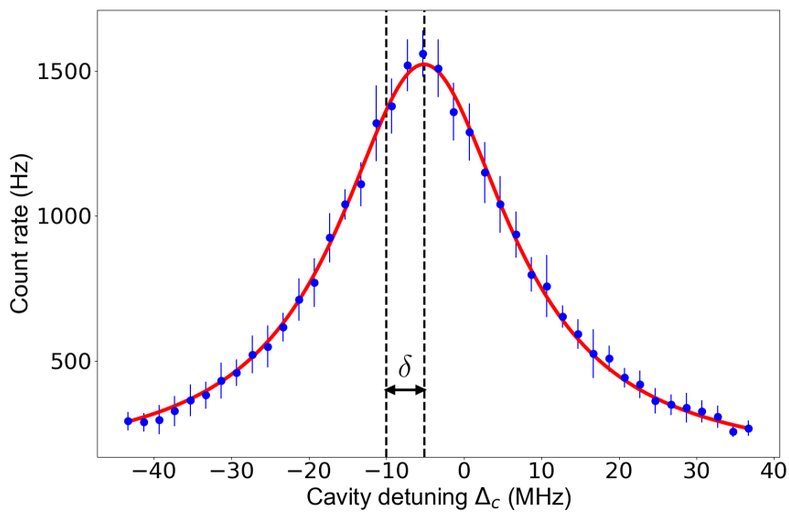

Figure 5: Measured cavity emission vs cavity detuning for a fixed probe detuning of -10 MHz. The red line is a Lorentzian fit to the data. The Raman resonance is shifted by δ from the expected value.

To scan the cavity across the Raman resonance while using the cavity cooling technique we use the pulse sequence displayed in Figure 6. Initially, the ion is prepared in the $S_{1/2}$ state, which decouples the ion from the cavity. The cavity transmission is then measured with an 866 nm laser that is tuned to the atomic transition. In this way the reference point of the cavity detuning ($\Delta_c = 0$) is determined. This is followed by a cavity cooling period, where the cavity is blue detuned by 7 MHz from the nominal Raman resonance (this is the optimal cavity detuning for maximising cavity cooling efficiency). The ion is then shuttled adiabatically from the node to the antinode whilst simultaneously preparing the ion in the ground state. This is followed by the single photon generation and detection of the cavity

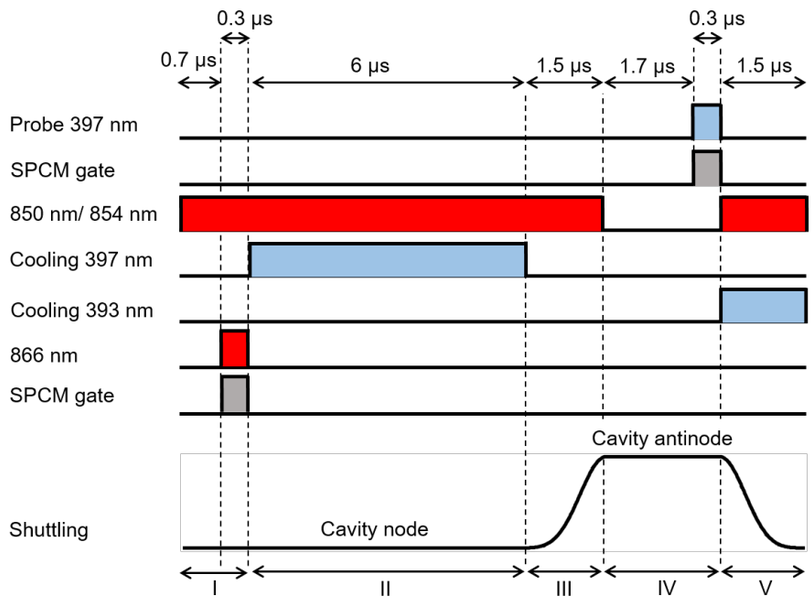

Figure 6: Laser pulses and shuttling voltage pulse during one cycle. (I) State preparation to the $4^2S_{1/2}$ state followed by measurement of the cavity transmission of a laser beam tuned on resonance with the 866 nm atomic transition for reference. Photons are collected by a gated SPCM. (II) Cavity cooling for 6 μs with the cavity detuned from the nominal Raman resonance by +7 MHz. (III) Adiabatic shuttling of the ion to the antinode and state preparation. (IV) Generation of a single photon and collection of photons by a gated SPCM. (V) Adiabatic return of the ion to the node with additional Doppler cooling with a 393 nm laser.

emission via a gated single-photon counting module. Finally, the ion is moved back to the node while simultaneously being Doppler cooled on the $S_{1/2} \leftrightarrow P_{3/2}$ transition. This pulse sequence is repeated as the cavity is scanned across the Raman resonance . As the cavity is scanned during this measurement the cooling beam frequency is varied to keep the detuning of the cavity from the nominal Raman resonance with the cooling beam constant.

We repeat this Raman spectroscopy for different probe detunings, to measure how δ changes. Plotting the shift δ against the probe detuning exhibits a dispersion-like profile. The spectrum is simulated using an 8-level model of $^{40}Ca^+$ and a bimodal cavity and used to extract the shift δ for each probe detuning. In this simulation, the only free parameter is the coherent ion-cavity coupling g_0. In Figure 7 we plot the traces of the simulation for different g_0 values. Using this model as a map we fit to our experimental data and extract the coherent ion-cavity coupling. The measured coupling without cavity cooling is $2\pi \times (15.2 \pm 0.1)$ MHz (see Figure 7). When including a period of cavity cooling in the sequence (Figure 6), the coherent ion-cavity coupling increases to $2\pi \times (16.7 \pm 0.1)$ MHz. With the expected ion-cavity coupling for a perfectly localised ion of $2\pi \times 17.3$ MHz, we calculated that the addition of the cavity cooling step reduces the spread of the ion's position from 110 nm to 55 nm, and the corresponding temperature from 8.5 mK to 2.1 mK. We have increased the measured ion-cavity coupling from 87% of the theoretically possible ion-cavity coupling with Doppler cooling to 97% with the introduction of cavity cooling.

While there is a significant improvement in the localisation of the ion through cavity cooling, the effect is significantly smaller than what is expected from a numerical simulation of the cavity cooling process. As the micromotion minimum is 17 nm away from the cavity antinode, the effect of

micromotion during measurement of the coupling strength is negligible. However, micromotion may have a significant impact during the cooling phase of the sequence, limiting cooling efficiency, since the micromotion minimum is 200 nm away from the node. The micromotion leads to a reduced effective ion-cavity coupling and subsequently a lowered cooling efficiency. In addition, the driven periodic motion induces spectral sidebands at the trap drive frequency which can further deteriorate the cavity cooling efficiency.

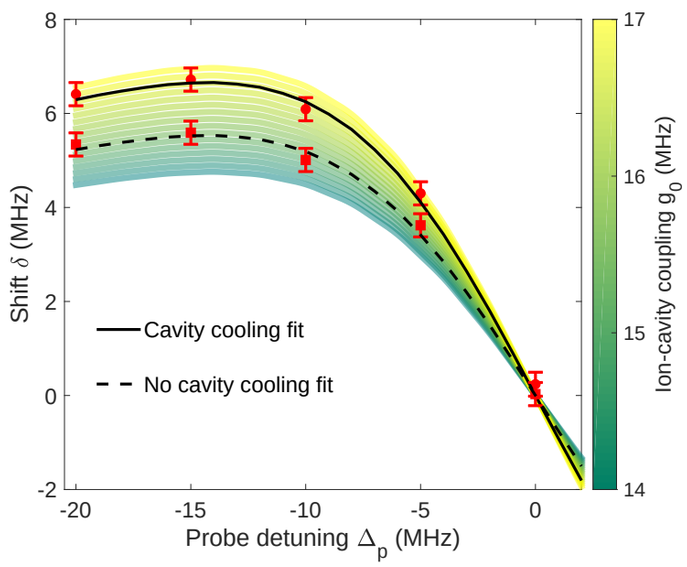

Figure 7: Plots of the shift of the Raman resonance δ versus the detuning of the probe beam Δ_p. The colour coded map shows the results of the simulation (in units of 2π) that we use to fit the data and extract the coherent coupling. The dashed line shows the fit and the data when there is no cavity cooling and the solid line when there is. The ion-cavity coupling is $2\pi \times (15.2 \pm 0.1)$ MHz without cavity cooling and $2\pi \times (16.7 \pm 0.1)$ MHz with cavity cooling.

5 Summary

In conclusion, we have demonstrated that an optical cavity can be used to significantly improve the localisation of the ion. By exploiting the strong ion-cavity coupling for cavity cooling instead of circumventing its effect on the laser cooling, we have been able to improve the localisation of the ion in the cavity and thus the effective ion-cavity coupling. While the ion-cavity coupling in our system is limited to $2\pi \times (15.2 \pm 0.1)$ MHz by Doppler cooling, we can achieve $2\pi \times (16.7 \pm 0.1)$ MHz when employing cavity cooling. This corresponds to 97% of the maximally achievable coupling in our system. Notably, this is the highest ion-cavity coupling achieved for a single ion in the strong coupling regime.

6 Acknowledgment

This project has received funding from the European Union's Horizon 2020 research and innovation program under the Marie Sklodowska-Curie grant agreement No 765075.

We gratefully acknowledge support from EPSRC through the UK Quantum Technology Hub: NQIT - Networked Quantum Information Technologies (EP/M013243/1).

References

[1] T. P. Harty, D. T. C. Allcock, C. J. Ballance, .L Guidoni, H. A. Janacek, N. M. Linke, D. N. Stacey, and D. M. Lucas. High-fidelity preparation, gates, memory, and readout of a trapped-ion quantum bit. *Physical review letters*, 113(22):220501, 2014.

[2] C. J. Ballance, T. P. Harty, N. M. Linke, M. A. Sepiol, and D. M. Lucas. High-fidelity quantum logic gates using trapped-ion hyperfine qubits. *Physical review letters*, 117(6):060504, 2016.

[3] H. Takahashi, E. Kassa, C. Christoforou, and M. Keller. Strong coupling of a single ion to an optical cavity. *Physical Review Letters*, 124(1):013602, 2020.

[4] A. Stute, B. Casabone, P. Schindler, T. Monz, P. O. Schmidt, B. Brandstätter, T. E. Northup, and R. Blatt. Tunable ion–photon entanglement in an optical cavity. *Nature*, 485(7399):482–485, 2012.

[5] A. Stute, B. Casabone, B. Brandstätter, K. Friebe, T. E. Northup, and R. Blatt. Quantum-state transfer from an ion to a photon. *Nature photonics*, 7(3):219, 2013.

[6] B. Casabone, A. Stute, K. Friebe, B. Brandstätter, K. Schüppert, R. Blatt, and T. E. Northup. Heralded entanglement of two ions in an optical cavity. *Physical review letters*, 111(10):100505, 2013.

[7] G. R. Guthöhrlein, M. Keller, K. Hayasaka, W. Lange, and H. Walther. A single ion as a nanoscopic probe of an optical field. *Nature*, 414(6859):49–51, 2001.

[8] A. B. Mundt, A. Kreuter, C. Becher, D. Leibfried, J. Eschner, F. Schmidt-Kaler, and R. Blatt. Coupling a single atomic quantum bit to a high finesse optical cavity. *Physical review letters*, 89(10):103001, 2002.

[9] S. Begley, M. Vogt, G. K. Gulati, H. Takahashi, and M. Keller. Optimized multi-ion cavity coupling. *Physical review letters*, 116(22):223001, 2016.

[10] E. Kassa, H. Takahashi, C. Christoforou, and M. Keller. Precise positioning of an ion in an integrated paul trap-cavity system using radiofrequency signals. *Journal of Modern Optics*, 65(5-6):520–528, 2018.

[11] H. Takahashi, E. Kassa, C. Christoforou, and M. Keller. Cavity-induced anticorrelated photon-emission rates of a single ion. *Physical Review A*, 96(2):023824, 2017.

[12] J. I. Cirac, A. S. Parkins, R. Blatt, and P. Zoller. Cooling of a trapped ion coupled strongly to a quantized cavity mode. *Optics communications*, 97(5-6):353–359, 1993.

[13] P. Horak, G. Hechenblaikner, K. M. Gheri, H. Stecher, and H. Ritsch. Cavity-induced atom cooling in the strong coupling regime. *Physical review letters*, 79(25):4974, 1997.

[14] G. Hechenblaikner, M. Gangl, P. Horak, and H. Ritsch. Cooling an atom in a weakly driven high-q cavity. *Physical Review A*, 58(4):3030, 1998.

[15] S. Zippilli and G. Morigi. Cooling trapped atoms in optical resonators. *Physical review letters*, 95(14):143001, 2005.

[16] M. Bienert and G. Morigi. Cavity cooling of a trapped atom using electromagnetically induced transparency. *New Journal of Physics*, 14(2):023002, 2012.

[17] V. Vuletić, H. W. Chan, and A. T. Black. Three-dimensional cavity doppler cooling and cavity sideband cooling by coherent scattering. *Physical Review A*, 64(3):033405, 2001.

[18] D. R. Leibrandt, J. Labaziewicz, V. Vuletić, and I. L. Chuang. Cavity sideband cooling of a single trapped ion. *Physical review letters*, 103(10):103001, 2009.

[19] M. H. Schleier-Smith, I. D. Leroux, H. Zhang, M. A. Van Camp, and V. Vuletić. Optomechanical cavity cooling of an atomic ensemble. *Physical review letters*, 107(14):143005, 2011.

[20] H. Takahashi, J. Morphew, F. Oručević, A. Noguchi, E. Kassa, and M. Keller. Novel laser machining of optical fibers for long cavities with low birefringence. *Optics express*, 22(25):31317–31328, 2014.

[21] N. Seymour-Smith, P. Blythe, M. Keller, and W. Lange. Fast scanning cavity offset lock for laser frequency drift stabilization. *Review of Scientific Instruments*, 81(7):075109, 2010.

[22] P. Maunz, T. Puppe, I. Schuster, N. Syassen, P. W. H. Pinkse, and G. Rempe. Cavity cooling of a single atom. *Nature*, 428(6978):50–52, 2004.

[23] M. Keller, B. Lange, K. Hayasaka, W. Lange, and H. Walther. Stable long-term coupling of a single ion to a cavity mode. *Journal of Modern Optics*, 54(11):1607–1617, 2007.

Chapter 6

Conclusion and Outlook

The purpose of this experiment from the start, was to build a hybrid ion-cavity system that operates in the strong coupling regime, and measure the ion-cavity coupling. We have showed how to incorporate a FFPC with a 3-D Paul trap, and how to overcome the distortion of the trapping field by the dielectric material of the cavity. Then, we showed how to shift the ion's position using additional RF signals, to optimise the overlap of the ion with the cavity mode. After placing the ion at the centre of the cavity, we measured the coherent coupling of the ion to the cavity, which we found to be $g_0 = 2\pi \times (15.1 \pm 0.1)$ MHz. This gives a coupling of $g = 2\pi \times (12.3 \pm 0.1)$ MHz, which is greater than the losses in our system ($g > \gamma, \kappa$), where $\gamma = 2\pi \times 11.5$ MHz and $\kappa = 2\pi \times (4.1 \pm 0.1)$ MHz. This places the coupling of our system in the strong coupling regime. This is the first ever measured strong coupling for a single ion to an optical cavity. In addition, we measured the vacuum Rabi splitting, and showed it is effected by having a bimodal cavity coupled to a three-level system. Having confirmed that the system is in the strong coupling regime, we improved the axial localisation of the ion through cavity cooling. Using this technique we managed to increase the localisation, and measure an even larger coherent coupling of $g_0 = 2\pi \times (16.7 \pm 0.1)$ MHz, out of a maximal theoretical value of $g_0 = 2\pi \times (17.3 \pm 0.1)$ MHz.

The work reported in this thesis is a breakthrough in the field of cavity-QED with trapped atomic ions. It is the very first demonstration of strong coupling of a single ion to a single mode of an optical cavity. This achievement will have many applications in science and technology such as, quantum interfaces and quantum networks, quantum computing and quantum non-destructive measurements [85] [86]. There has been a growing interest in physical hybrid systems consisting of well controlled single emitters and a single optical mode. In the publications in this thesis we have established a new ground in this new research field. This was made possible by the unprecedented degree of control over the interaction between the emitter and the mode of an optical cavity. We have shown in the supplementary material in Chapter 4 that heralded entanglement for quantum networks using trapped ions can benefit from a strongly coupled ion-cavity system. Then we showed experimentally how cavity cooling can be used for a system in the strong coupling regime, to improve the localisation of the ion. This is beneficial for many systems where the optical access to the centre of the trap is limited, and Doppler cooling is not efficient.

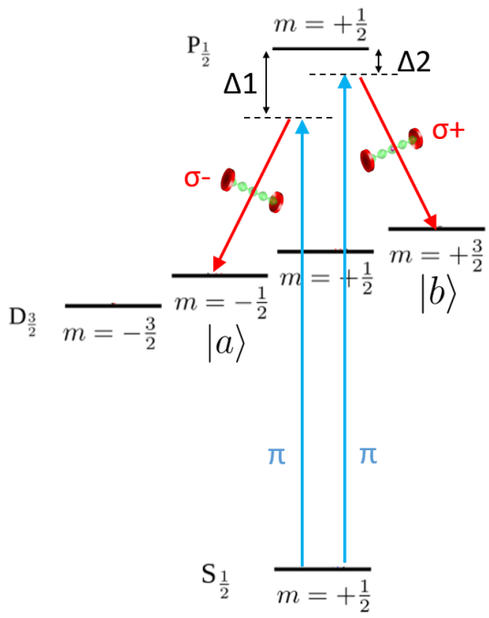

Figure 6.1: Entanglement scheme. Two π lasers drive two Raman transitions placing the ion in a coherent superposition.

The next experiment to be carried out in this system involves ion-photon entanglement. The scheme is similar to the one described in [87]. If the ion is initially prepared in the $S_{1/2}$, $m = +1/2$ state, the ion is placed in a coherent superposition between two Zeeman sub-levels by driving two Raman transitions, as shown in Figure 6.1. Equal population in $D_{3/2}$, $m - 1/2$ and $D_{3/2}$, $m + 3/2$ is achieved by using the correct driving laser power to compensate for the different Clebsch-Gordan coefficients. After photon emission, the system is in the entangled state

$$|\psi_{atom,photon1}\rangle = \frac{1}{\sqrt{2}}\left(|a, \sigma^-\rangle - |b, \sigma^+\rangle \right) \tag{6.1}$$

Having showed ion-photon entanglement the next step, in creating a Quantum Network, is to add a second system. Then we can show ion-ion entanglement between two remote systems.

Appendix A

Cavity-induced anticorrelated photon-emission rates of a single ion

During the 4 years of my PhD I have co-authored one more paper "Cavity-induced anticorrelated photon-emission rates of a single ion" [67], in addition to the three publications included in the main thesis. This publication was chronologically the first one out of the four included in this thesis. The reason why this publication was not included in the main body of the thesis, is because it did not fit the narrative of the thesis. Nevertheless, the work is important and for that reason I am including it in the Appendix.

Initially, we used the Purcell effect to show and measure the ion-cavity coupling, before optimising it by shifting the ion's position with respect to the cavity mode.

The Purcell effect is the enhancement of the spontaneous emission rate of an ion when placed in a resonant optical cavity. Fermi's golden rule states that the transition rate of an ion is proportional to the density of its final states. When an ion is placed in a resonant optical cavity the density of final states is enhanced.

Through the vacuum-stimulated emission of the cavity, which is frequency scanned across the transition $P_{1/2} \leftrightarrow D_{3/2}$, there is a strong suppression of the fluorescence on $P_{1/2} \leftrightarrow S_{1/2}$ transition. Therefore, there is an anti-correlation effect between the photon emission rates of the IR cavity emission and the UV free space fluorescence. By analysing the measurement results we obtain an average coherent ion-cavity coupling of $g_0 = 2\pi \times (5.3 \pm 0.1)$ MHz.

For this publication I contributed in setting up the experimental setup and assisting with the data acquisition.

PHYSICAL REVIEW A **96**, 023824 (2017)

Cavity-induced anticorrelated photon-emission rates of a single ion

Hiroki Takahashi, Ezra Kassa,* Costas Christoforou, and Matthias Keller
Department of Physics and Astronomy, University of Sussex, Brighton BN1 9RH, United Kingdom
(Received 24 May 2017; published 10 August 2017)

We report on the alteration of photon-emission properties of a single trapped ion coupled to a high-finesse optical fiber cavity. We show that the vacuum field of the cavity can simultaneously affect the emissions in both the infrared (IR) and ultraviolet (UV) branches of the Λ-type level system of $^{40}Ca^{+}$ despite the cavity coupling only to the IR transition. The cavity induces strong emission in the IR transition through the Purcell effect resulting in a simultaneous suppression of the UV fluorescence. The measured suppression of this fluorescence is as large as 66% compared with the case without the cavity. Through analysis of the measurement results, we have obtained an ion-cavity coupling of $\bar{g}_0 = 2\pi \times (5.3 \pm 0.1)$ MHz, the largest reported so far for a single ion in the IR domain.

DOI: 10.1103/PhysRevA.96.023824

The effect of a structured environment on the spontaneous emission of atomic particles was first discovered by Purcell in 1946 [1] and is named after him. More than 30 years later, it was experimentally demonstrated with Rydberg atoms [2,3]. Since then, enhanced and/or reduced emission rates due to an optical cavity surrounding single emitters have been shown in a variety of physical systems such as trapped ions [4–6], semiconductor quantum dots [7], nitrogen-vacancy centers in diamond [8], and rare-earth ions in solids [9,10]. In particular, single trapped ions coupled to optical cavities provide an ideal environment to study and exploit the enhanced light-matter interaction [4,11] due to their unparalleled quantum control. In these systems the use of cavities with small mode volumes is crucial in the enhancement of the ion-cavity coupling and, consequently, the emission into the cavity mode. To this end, miniaturized fiber-based Fabry-Pérot cavities (FFPCs) have been introduced and successfully combined with ion traps [6,12]. The integration of ion traps and FFPCs recently allowed the Purcell effect to be studied extensively in a two-level system [12]. However, the Purcell effect in a multilevel atomic system and its role in the branching ratios has not been investigated so far. In this article we demonstrate the coupling of a single ion to an optical FFPC and its strongly enhanced emission on an infrared (IR) transition into the cavity mode. Simultaneously, we measure the suppression of the spontaneous emission into free space on a strong ultraviolet (UV) transition of the same ion. While the presence of the cavity increases the ion's IR transition rate more than fourfold, the free-space emission of the ion on the UV transition is suppressed by 66%. Employing spectroscopic methods and the measurements of optical pumping dynamics, all relevant experimental parameters are determined and used for successfully modeling the experimental results.

A single $^{40}Ca^{+}$ ion is trapped in an endcap-style radio-frequency (rf) Paul trap described in Refs. [13,14]. It is formed by a pair of electrode assemblies, each consisting of two concentric stainless steel tubes [see Fig. 1(a)]. For both assemblies, the outer electrode is recessed by 230 μm with respect to the inner electrode. The separation between the inner electrodes of the opposing assemblies is 350 μm. By applying an rf voltage at a frequency of 19.6 MHz to the outer electrodes while setting the inner electrodes to rf ground, a trapping potential is formed between the two electrode assemblies. The axial and radial secular frequencies are measured to be 3.46 and 1.96 MHz, respectively, with an estimated trap depth of 0.9 eV. Four additional electrodes are placed in the radial plane at a distance of 1.0 mm from the center of the trap. By applying dc voltages to two of these radial electrodes as well as the upper and lower inner electrodes of the main assemblies, stray electric fields are compensated to minimize excess micromotion of the ion by using the standard rf correlation technique [15]. The ion trap is combined with an FFPC by incorporating each fiber into the tubular inner electrodes. Both fibers have a CO_2 laser-machined concave facet [16] with radii of curvature of 560 μm and a high reflective coating of 25 ppm transmission at 866 nm. One is a single-mode fiber to serve as the cavity input and the other is a multimode fiber which constitutes the output of the cavity. Each fiber is retracted by 5–10 μm from the end facet of the inner electrode in which it is inserted. The resulting cavity length of 367 μm is deduced by scanning the frequency of a laser injected in the cavity by one free spectral range (FSR) which equates to FSR $= c/2L$, where c is the speed of light and L is the cavity length. The geometry of the cavity leads to a predicted coherent ion-cavity coupling of $g_0 = 2\pi \times 17.2$ MHz with the $P_{1/2}$-$D_{3/2}$ transition of $^{40}Ca^{+}$ at 866 nm. Note that this is the theoretical expectation when the ion-cavity overlap is optimal. The cavity finesse is 48 000, corresponding to a cavity decay rate of $\kappa = 2\pi \times 4.2$ MHz. The magnetic field throughout the experiment is set to 0.78 G along the cavity axis.

Figure 1(b) shows a schematic of the experimental setup. The ion is driven by three different laser beams at 397, 850, and 854 nm which are near resonant with the $S_{1/2}$-$P_{1/2}$, $P_{3/2}$-$D_{3/2}$, and $P_{3/2}$-$D_{5/2}$ transitions, respectively. Associated with these lasers are the detunings Δ_{397}, Δ_{850}, and Δ_{854} from the respective resonance frequencies as shown in Fig. 2(a). The laser at 397 nm is used for Doppler cooling of the ion. The fluorescence on this transition as well as the spontaneous emission from the $P_{3/2}$ state is detected with a photomultiplier tube via free-space objective lenses. The repumper lasers at 850 and 854 nm are used to depopulate the metastable $D_{3/2}$ and $D_{5/2}$ states and bring the ion back to the $S_{1/2}$ state via

*Ezra.Kassa@sussex.ac.uk

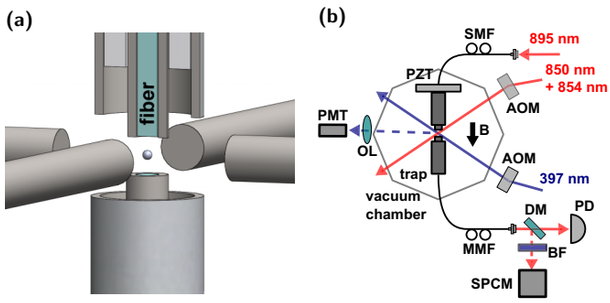

FIG. 1. (a) A close-up view of the ion-trap structure with an integrated FFPC. Only a cross section of the upper assembly is shown to reveal the internal structure: The fibers reside inside the inner electrodes and electrical isolation between the inner and outer electrodes is provided by ceramic spacer tubes. Four additional electrodes are located on the radial plane at the same height as the ion. (b) A simplified schematic of the experimental setup: AOM, acousto-optic modulator; BF, bandpass filter for 866 nm; DM, dichroic mirror; MMF, multimode fiber; OL, objective lens; PD, photodetector for the transmission of the 895-nm beam; PMT, photomultiplier tube; PZT, piezoelectric transducer; SMF, single-mode fiber; and SPCM, single-photon counting module. The output of the MMF is filtered with a DM which transmits the 895-nm beam used for cavity locking. The reflection is further filtered by a BF before being detected by the SPCM. The magnetic field (B) is controlled by external coils (not shown) and applied vertically along the cavity axis.

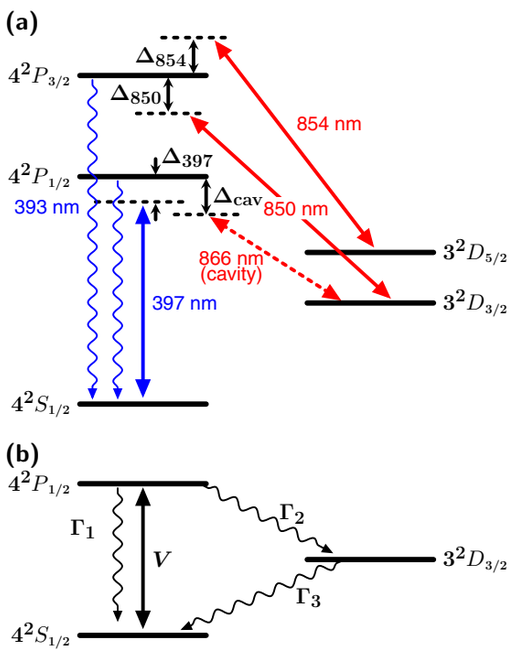

FIG. 2. (a) Energy-level diagram of the $^{40}Ca^+$ ion and driving lasers with relevant detunings. The cavity field operates on the 866-nm transition between the $4\,^2P_{1/2}$ and $3\,^2D_{3/2}$ states. The wavy lines indicate the UV fluorescence emissions to be detected with the PMT. The detunings are measured positive (negative) when the laser is blue (red) detuned. (b) Effective scheme for the three low-lying levels.

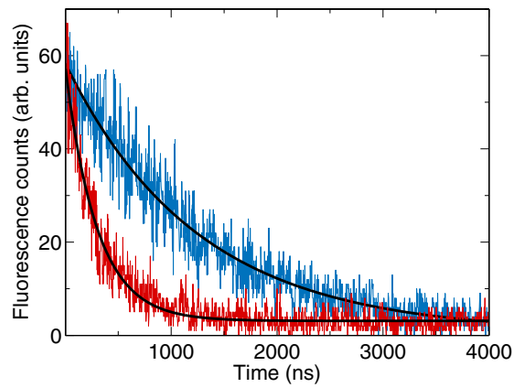

FIG. 3. UV fluorescence detected with the PMT as the ion is shelved to the $D_{3/2}$ state with the cavity on the Raman resonance (red, lower) and with the cavity far detuned ($\gg 2\kappa$) from the Raman resonance (blue, upper). The solid black lines are exponential fits.

spontaneous decay from the $P_{3/2}$ state. Another laser beam at 895 nm is injected into the FFPC through the input single-mode fiber and employed to stabilize the cavity length using the Pound-Drever-Hall technique. The error signal for the cavity length is generated from the transmission signal through the multimode fiber detected by the PD and fed back to the PZT attached to the upper assembly, which in turn changes the length of the FFPC. The frequency of this stabilization laser is adjusted such that the FFPC satisfies the resonance condition for the $P_{1/2}$-$D_{3/2}$ transition. All the lasers are frequency stabilized to a reference laser via a scanning cavity transfer lock [17].

A standard technique of observing the Purcell effect is through the measurement of the decay rate of the relevant transition. Here, it is manifested as an increased rate at which the ion's population is transferred from the $P_{1/2}$ state to the $D_{3/2}$ state. To infer this rate, we measure the transient change of the ion's fluorescence rate after the repumpers are abruptly switched off. Figure 3 shows the UV fluorescence in multiple repetitions of this shelving process with and without a near-resonant cavity. The detuning of the cavity, Δ_{cav}, and that of the cooling laser, Δ_{397}, are set to satisfy a Raman resonance condition $\Delta_{397} = \Delta_{cav} = -2\pi \times 11.4$ MHz. Exponential decay fits to the data give time constants of $\tau_{on} = 292 \pm 5$ ns and $\tau_{off} = 1246 \pm 23$ ns for the on- and off-resonant cases, respectively, demonstrating that the decay rate is enhanced by more than a factor of 4 by the cavity.

However, the Purcell effect can also be observed in the interplay of decay rates between competing transitions from the same excited state. While driving the ion continuously and scanning the cavity detuning across the Raman resonance, spectra for the cavity emission and the free-space UV fluorescence can be measured simultaneously with the SPCM and PMT, respectively [see Fig. 1(b)]. The cavity emission spectrum in Fig. 4(a) has a maximum measured net count rate of ~22 000 c/s and a half width at half maximum of $\delta = 10.3 \pm 0.1$ MHz. The UV fluorescence in Fig. 4(b) is normalized to the fluorescence rate measured with a far-detuned cavity. Anticorrelation between the two spectra is clearly visible. The suppression of the UV fluorescence

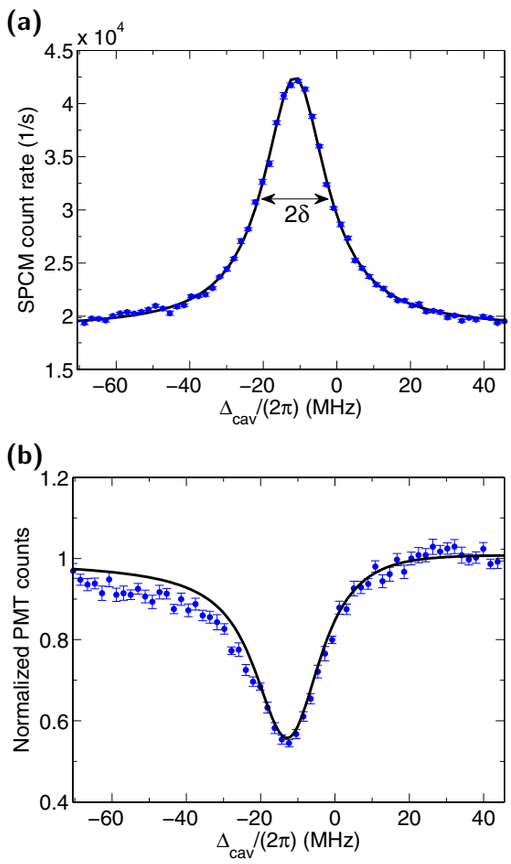

FIG. 4. (a) Emission of the ion into the cavity as its detuning is scanned across the Raman resonance. Scatter from the repumping and locking lasers contribute to the background counts of ∼19 000 c/s. The solid black line is a fit by the Lorentzian function. The error bars show the statistical mean standard errors. (b) Normalized UV fluorescence measured simultaneously with (a). The solid black line is a numerical simulation using the measured experimental parameters.

around the Raman resonance can be understood by using rate equations for the effective model shown in Fig. 2(b). In this model only the populations in the three low-lying levels are considered and those in the $P_{3/2}$ and $D_{5/2}$ states are ignored. Γ_1 and Γ_2 are the spontaneous decay rates from the $P_{1/2}$ state to the $S_{1/2}$ and $D_{3/2}$ states, respectively, and V is the pumping rate of the cooling laser. The 850- and 854-nm repumping lasers are modeled as an effective incoherent decay from the $D_{3/2}$ state to the $S_{1/2}$ state characterized by decay rate Γ_3. This system is described by the following rate equations:

$$\frac{dN_S}{dt} = -VN_S + (\Gamma_1 + V)N_P + \Gamma_3 N_D, \tag{1}$$

$$\frac{dN_P}{dt} = VN_S - (\Gamma_1 + \Gamma_2 + V)N_P, \tag{2}$$

$$\frac{dN_D}{dt} = \Gamma_2 N_P - \Gamma_3 N_D. \tag{3}$$

Here N_X $(X = S, P, D)$ is the population of one of the $S_{1/2}$, $P_{1/2}$, and $D_{3/2}$ states, respectively. The steady-state condition $(dN_S/dt = dN_P/dt = dN_D/dt = 0)$ leads to $N_P \approx (1 + \Gamma_2/\Gamma_3 + (\Gamma_1 + V)/V)^{-1}$. Here $\Gamma_1 + V \gg \Gamma_2$, which is approximately satisfied in our experiment, is used. If the cavity modifies the decay rate Γ_2 to Γ_2' due to the Purcell effect, the modified normalized fluorescence rate is given by

$$\frac{N_P'}{N_P} \approx 1 - \frac{1 - v}{1 + w\left(\frac{\Gamma_1 + 2V}{V}\right)}, \tag{4}$$

where $v = \Gamma_2/\Gamma_2'$, $w = \Gamma_3/\Gamma_2'$, and N_P and N_P' are the $P_{1/2}$ state populations at equilibrium with and without the resonant cavity, respectively. One can see that increasing Γ_2' (decreasing v and w) results in the suppression of the normalized fluorescence rate.

Even though qualitative understanding of the anticorrelated photon emissions can be obtained with the simplified model, in order to quantitatively analyze the measurement results, detailed characterization of the experimental parameters in conjunction with numerical simulation is necessary. Our simulations are based on the master equation model involving all the 18 Zeeman sublevels of the $S_{1/2}$, $P_{1/2}$, $P_{3/2}$, $D_{3/5}$, and $D_{5/2}$ states. The simulations use the Quantum Optics toolbox [18] for MATLAB. The laser parameters are measured individually and summarized in Table I. The detunings are obtained spectroscopically. Since no repumping dynamics is involved in the shelving measurement with the off-resonant cavity (Fig. 3), the only unknown parameter is Ω_{397} for a given Δ_{397}. By fitting the numerical simulation to the measured time constant τ_{off}, the Rabi frequency Ω_{397} is obtained. Having deduced Ω_{397}, Ω_{850} is similarly obtained from a shelving measurement to the $D_{5/2}$ state. Ω_{854} is obtained from the ac Stark shift caused by the 854-nm laser. For more details see the Appendix. A key parameter to characterize our system is the ion-cavity coherent coupling strength g_0. It can be extracted from the combination of the results in Figs. 3 and 4(a). g_0 is a function of the ion's axial position $(= z)$ in the standing wave of the cavity field $[\propto \cos(kz)]$, and the finite spatial localization of the ion leads to the averaging of couplings at different positions [19]. Furthermore, the ion's motion as well as the instability of the cavity and laser locks introduce inhomogeneous broadening in the spectra shown in Fig. 4. This can be described as a Gaussian distribution of the cavity detuning Δ_{cav} with a standard deviation σ. These two effects, the spatial average of g_0 and the inhomogeneous spectral broadening, originate from the ion's spatial and momentum distributions in phase space, respectively [see Fig. 5(a)] and hence are taken into account separately. In a simulation the former effect is taken into account by simply using an averaged effective coupling $\bar{g}_0$ rather than g_0. The effect of inhomogeneous broadening is taken into account by calculating the weighted average of the

TABLE I. Measured laser parameters for the simulations in Fig. 4(b) and Fig. 6. Ω_{397}, Ω_{850}, and Ω_{854} are the Rabi frequencies for the relevant laser beams. The cooling (397 nm) and repumping (850 and 854 nm) lasers are vertically and horizontally polarized, respectively, where the quantization axis is given by the vertically applied magnetic field.

Δ_{397}	$-2\pi \times 11.4 \pm 0.2$ MHz	Ω_{397}	$2\pi \times 18.2 \pm 0.2$ MHz
Δ_{850}	$-2\pi \times 1.1 \pm 0.1$ MHz	Ω_{850}	$2\pi \times 6.5 \pm 0.1$ MHz
Δ_{854}	$2\pi \times 24.8 \pm 0.1$ MHz	Ω_{854}	$2\pi \times 8.9 \pm 0.4$ MHz

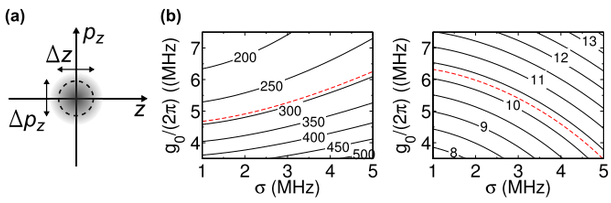

FIG. 5. (a) The ion is in a thermal distribution in the phase space spanned by the spatial (z) and momentum (p_z) coordinates. The delocalization in z results in the averaging of g_0 whereas the distribution along p_z results in the spectral inhomogeneous broadening due to the Doppler effect. (b) Numerical simulation of τ_{on} (left) and δ (right) as a function of $\bar{g}_0$ and σ shown as two-dimensional contour plots. The labels on the contour lines are in units of nanoseconds (left) and megahertz (right). The dashed red contour lines correspond to the measured values of $\tau_{on} = 292$ ns and $\delta = 10.3$ MHz.

simulations over a range of Δ_{cav} with a width σ. In order to deduce $\bar{g}_0$ and σ, we numerically calculate the dependence of τ_{on} and δ on them, as shown in Fig. 5(b). The dashed contour lines in Fig. 5(b) correspond to the experimentally observed values of τ_{on} and δ and the crossing point of these two lines uniquely determines the values of $\bar{g}_0$ and σ in our experimental realization. As a result, we get $\bar{g}_0 = 2\pi \times (5.3 \pm 0.1)$ MHz and $\sigma = 3.1 \pm 0.2$ MHz.

Having obtained $\bar{g}_0$ and σ in addition to the experimental parameters in Table I, numerical simulation for the UV fluorescence spectrum is carried out without a free fitting parameter (except for the frequency offset which is adjusted by using the peak position of the cavity emission). The theoretical prediction shown as the black line in Fig. 4(b) matches the experimental data well, demonstrating the validity of our model and the prior measurements. Further scans are taken with different 850-nm repumper detunings, Δ_{850}, and the maximum suppression in the normalized UV fluorescence spectra are collected and shown in Fig. 6. As the 850-nm laser is detuned, the effective repumping rate is decreased. This

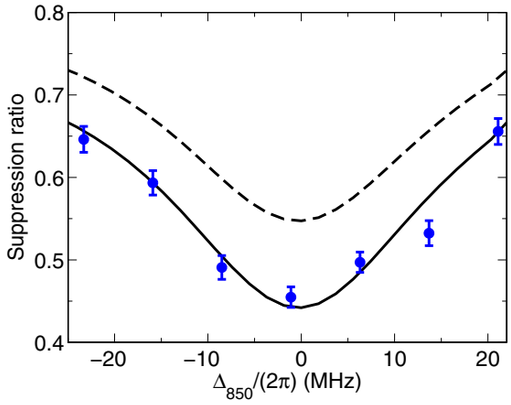

FIG. 6. Maximum suppression in the normalized UV fluorescence spectra for various Δ_{850}. The solid (dashed) black line shows the numerical simulation including (excluding) the fluorescence at 393 nm. Apart from Δ_{850}, the same parameters as the ones in Table I are used.

corresponds to decreasing w in Eq. (4), which leads to further suppression of the normalized fluorescence. As a result, a total suppression of the fluorescence up to 66% has been observed. This is a clear demonstration that the mere presence of a resonant cavity can significantly alter the radiation property of a single emitter. Note further that we detect the combined fluorescence at 397 and 393 nm [see Fig. 2(a)]. If only the photons at 397 nm were detected, even greater suppression would be seen as shown by the dashed line in Fig. 6.

In conclusion, we have developed an ion trap with an integrated high-finesse FFPC and have successfully coupled a single ion to the cavity. Due to the Λ-type three-level structure in $^{40}Ca^{+}$, the vacuum-stimulated emission of the resonant cavity on the $P_{1/2}$-$D_{3/2}$ transition leads to the strong suppression of the fluorescence on the $P_{1/2}$-$S_{1/2}$ transition. As a result, anticorrelated photon emission rates at two different wavelengths have been observed between the IR cavity emission and the free-space UV fluorescence. From the thorough analysis of the measurement results, we have obtained an averaged ion-cavity coupling of $\bar{g}_0 = 2\pi \times (5.3 \pm 0.1)$ MHz with a corresponding cooperativity parameter of $C = \frac{\bar{g}_0^2}{2\kappa\gamma} = 0.30$. This coupling strength is the largest reported value so far for a single trapped ion in the IR domain. Currently the overlap between the ion and cavity field is limited by the construction accuracy with which the trap was built. However, by applying synchronous rf voltages on the radial electrodes, the rf null of the potential can be displaced to optimize the ion-cavity overlap without increasing excess micromotion [20]. This would greatly improve the ion-cavity coupling towards the strong-coupling regime with an expected coupling strength of $g_0 = 2\pi \times 17.2$ MHz.

We gratefully acknowledge support from EPSRC through the UK Quantum Technology Hub: Networked Quantum Information Technologies (NQIT) (Grants No. EP/M013243/1 and No. EP/J003670/1). We thank the late Wolfgang Lange for his contribution in the foundations of this experiment. H.T. thanks the Japan Science and Technology Agency (PRESTO) for their funding at the early stage of the experiment.

APPENDIX: MEASURING THE RABI FREQUENCIES OF THE REPUMPING BEAMS

The Rabi frequency for the 850-nm beam is obtained by measuring the rate at which the ion's population is transferred from the $D_{3/2}$ to the $D_{5/2}$ state. This is accomplished with the pulse sequence shown in Fig. 7. Throughout the sequence

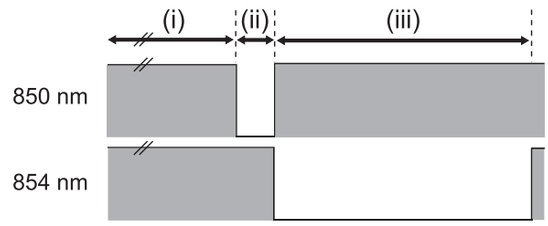

FIG. 7. Pulse sequence for the 850- and 854-nm beams in the Ω_{850} measurement. The time durations are 170 μs in stage (i), 30 μs in stage (ii), and 200 μs in stage (iii).

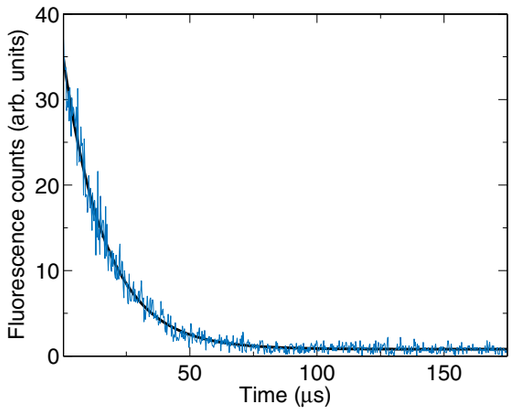

FIG. 8. Fluorescence counts as a function of time in stage (iii) of the sequence in Fig. 7. The solid black line is an exponential fit to the data.

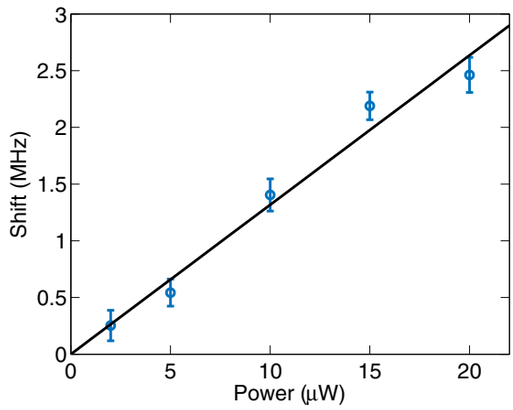

FIG. 9. Observed frequency shift of the fluorescence spectrum as a function of the 854-nm laser power. The solid line shows a linear fit to the data.

the cooling beam at 397 nm is kept on. Following the cooling stage denoted as stage (i), the 850-nm beam is turned off for 30 μs in stage (ii) in order to prepare the ion in the $D_{3/2}$ state. Subsequently the 850-nm beam is turned back on and the 854-nm beam is turned off in stage (iii), where the population of the ion is pumped into the $D_{5/2}$ state. Since Ω_{397}, Δ_{397}, and Δ_{850} have been already determined from the previous measurements, the dynamics in stage (iii) can be precisely simulated with our 18-level model with only Ω_{850} being an unknown parameter. Figure 8 shows the transient fluorescence count rate during stage (iii) accumulated over multiple repetitions of the pulse sequence. By fitting Ω_{850} in the numerical simulation to the observed decay time of 16.7 μs in Fig. 8, $\Omega_{850} = 2\pi \times (6.5 \pm 0.1)$ MHz is obtained.

Having obtained Ω_{397} and Ω_{850} as well as all the detunings Δ_{397}, Δ_{850}, and Δ_{854}, Ω_{854} is obtained from measurements of the ac Stark shift caused by the 854-nm beam on the fluorescence spectrum. Here the fluorescence spectrum is measured as a function of Δ_{850} and its center frequencies are recorded as the power of the 854-nm beam is varied. Figure 9 shows the measurement result which gives the frequency shift $\Delta_{\text{shift}}/P = (0.13 \pm 0.01)\,\text{MHz}/\mu\text{W}$ as a function of the optical power P. On the other hand, the numerical simulation predicts $\Delta_{\text{shift}}/\Omega_{854}^2 = 3.3 \times 10^{-3}\ \text{MHz}^{-1}$. From these relationships, we obtain $\Omega_{854} = 2\pi \times (6.3 \pm 0.3) \times \sqrt{P}$. Hence for 2.0 μW of optical power used in the experiment, the Rabi frequency $\Omega_{854} = 2\pi \times (8.9 \pm 0.4)\,\text{MHz}$.

[1] E. M. Purcell, Phys. Rev. **69**, 681 (1946).
[2] P. Goy, J. M. Raimond, M. Gross, and S. Haroche, Phys. Rev. Lett. **50**, 1903 (1983).
[3] R. G. Hulet, E. S. Hilfer, and D. Kleppner, Phys. Rev. Lett. **55**, 2137 (1985).
[4] M. Keller, B. Lange, K. Hayasaka, W. Lange, and H. Walther, Nature (London) **431**, 1075 (2004).
[5] A. Kreuter, C. Becher, G. P. T. Lancaster, A. B. Mundt, C. Russo, H. Häffner, C. Roos, J. Eschner, F. Schmidt-Kaler, and R. Blatt, Phys. Rev. Lett. **92**, 203002 (2004).
[6] M. Steiner, H. M. Meyer, C. Deutsch, J. Reichel, and M. Köhl, Phys. Rev. Lett. **110**, 043003 (2013).
[7] S. Unsleber, C. Schneider, S. Maier, Y.-M. He, S. Gerhardt, C.-Y. Lu, J.-W. Pan, M. Kamp, and S. Höfling, Opt. Express **23**, 32977 (2015).
[8] S. A. Wolf, I. Rosenberg, R. Rapaport, and N. Bar-Gill, Phys. Rev. B **92**, 235410 (2015).
[9] S. Karaveli and R. Zia, Opt. Lett. **35**, 3318 (2010).
[10] D. Ding, L. M. C. Pereira, J. F. Bauters, M. J. R. Heck, G. Welker, A. Vantomme, J. E. Bowers, M. J. A. de Dood, and D. Bouwmeester, Nat. Photonics **10**, 385 (2016).
[11] A. Stute, B. Casabone, P. Schindler, T. Monz, P. Schmidt, B. Brandstätter, T. Northup, and R. Blatt, Nature (London) **485**, 482 (2012).
[12] T. Ballance, H. Meyer, P. Kobel, K. Ott, J. Reichel, and M. Köhl, Phys. Rev. A **95**, 033812 (2017).
[13] H. Takahashi, A. Wilson, A. Riley-Watson, F. Oručević, N. Seymour-Smith, M. Keller, and W. Lange, New J. Phys. **15**, 053011 (2013).
[14] E. Kassa, Ph.D. thesis, University of Sussex, 2017.
[15] D. J. Berkeland, J. D. Miller, J. C. Bergquist, W. M. Itano and D. J. Wineland, J. Appl. Phys. **83**, 5025 (1998).
[16] H. Takahashi, J. Morphew, F. Oručević, A. Noguchi, E. Kassa, and M. Keller, Opt. Express **22**, 31317 (2014).
[17] N. Seymour-Smith, P. Blythe, M. Keller, and W. Lange, Rev. Sci. Instrum. **81**, 075109 (2010).
[18] S. M. Tan, J. Opt. B **1**, 424 (1999).
[19] S. Begley, M. Vogt, G. K. Gulati, H. Takahashi, and M. Keller, Phys. Rev. Lett. **116**, 223001 (2016).
[20] P. F. Herskind, A. Dantan, M. Albert, J. Marler, and M. Drewsen, J. Phys. B **42**, 154008 (2009).

Bibliography

[1] R. P. Feynman, *Feynman lectures on computation*. CRC Press, 2018.

[2] D. Deutsch, "Quantum theory, the church–turing principle and the universal quantum computer," *Proceedings of the Royal Society of London. A. Mathematical and Physical Sciences*, vol. 400, no. 1818, pp. 97–117, 1985.

[3] K. Gomi, "Council post: Quantum computing: Limits, options and applications," Sep 2020.

[4] R. Beals, H. Buhrman, R. Cleve, M. Mosca, and R. De Wolf, "Quantum lower bounds by polynomials," *Journal of the ACM (JACM)*, vol. 48, no. 4, pp. 778–797, 2001.

[5] L. K. Grover, "Quantum mechanics helps in searching for a needle in a haystack," *Physical review letters*, vol. 79, no. 2, p. 325, 1997.

[6] P. W. Shor, "Polynomial-time algorithms for prime factorization and discrete logarithms on a quantum computer," *SIAM review*, vol. 41, no. 2, pp. 303–332, 1999.

[7] R. Cleve and H. Buhrman, "Substituting quantum entanglement for communication," *Physical Review A*, vol. 56, no. 2, p. 1201, 1997.

[8] H. Buhrman, R. Cleve, and A. Wigderson, "Quantum vs. classical communication and computation," in *Proceedings of the thirtieth annual ACM symposium on Theory of computing*, pp. 63–68, 1998.

[9] D. P. DiVincenzo, "The physical implementation of quantum computation," *Fortschritte der Physik: Progress of Physics*, vol. 48, no. 9-11, pp. 771–783, 2000.

[10] J. Clarke and F. K. Wilhelm, "Superconducting quantum bits," *Nature*, vol. 453, no. 7198, pp. 1031–1042, 2008.

[11] M. A. Nielsen and I. L. Chuang, "Quantum computation and quantum information," *Phys. Today*, vol. 54, no. 2, p. 60, 2001.

[12] L. Henriet, L. Beguin, A. Signoles, T. Lahaye, A. Browaeys, G.-O. Reymond, and C. Jurczak, "Quantum computing with neutral atoms," *arXiv preprint arXiv:2006.12326*, 2020.

[13] T. D. Ladd, F. Jelezko, R. Laflamme, Y. Nakamura, C. Monroe, and J. L. O'Brien, "Quantum computers," *Nature*, vol. 464, no. 7285, pp. 45–53, 2010.

[14] P. W. Shor, "Proceedings of the 35th annual symposium on foundations of computer science," *IEE Computer society press, Santa Fe, NM*, 1994.

[15] J. I. Cirac and P. Zoller, "Quantum computations with cold trapped ions," *Physical review letters*, vol. 74, no. 20, p. 4091, 1995.

[16] W. Neuhauser, M. Hohenstatt, P. Toschek, and H. Dehmelt, "Localized visible ba+ mono-ion oscillator," *Physical Review A*, vol. 22, no. 3, p. 1137, 1980.

[17] C. D. Bruzewicz, J. Chiaverini, R. McConnell, and J. M. Sage, "Trapped-ion quantum computing: Progress and challenges," *Applied Physics Reviews*, vol. 6, no. 2, p. 021314, 2019.

[18] K. R. Brown, A. C. Wilson, Y. Colombe, C. Ospelkaus, A. M. Meier, E. Knill, D. Leibfried, and D. J. Wineland, "Single-qubit-gate error below 10- 4 in a trapped ion," *Physical Review A*, vol. 84, no. 3, p. 030303, 2011.

[19] J. Benhelm, G. Kirchmair, C. F. Roos, and R. Blatt, "Towards fault-tolerant quantum computing with trapped ions," *Nature Physics*, vol. 4, no. 6, pp. 463–466, 2008.

[20] A. Myerson, D. Szwer, S. Webster, D. Allcock, M. Curtis, G. Imreh, J. Sherman, D. Stacey, A. Steane, and D. Lucas, "High-fidelity readout of trapped-ion qubits," *Physical Review Letters*, vol. 100, no. 20, p. 200502, 2008.

[21] T. Harty, D. Allcock, C. J. Ballance, L. Guidoni, H. Janacek, N. Linke, D. Stacey, and D. Lucas, "High-fidelity preparation, gates, memory, and readout of a trapped-ion quantum bit," *Physical review letters*, vol. 113, no. 22, p. 220501, 2014.

[22] S. Crain, C. Cahall, G. Vrijsen, E. E. Wollman, M. D. Shaw, V. B. Verma, S. W. Nam, and J. Kim, "High-speed low-crosstalk detection of a 171 yb+ qubit using superconducting nanowire single photon detectors," *Communications Physics*, vol. 2, no. 1, pp. 1–6, 2019.

[23] A. Sørensen and K. Mølmer, "Quantum computation with ions in thermal motion," *Physical review letters*, vol. 82, no. 9, p. 1971, 1999.

[24] D. Leibfried, B. DeMarco, V. Meyer, D. Lucas, M. Barrett, J. Britton, W. M. Itano, B. Jelenković, C. Langer, T. Rosenband, *et al.*, "Experimental demonstration of a robust, high-fidelity geometric two ion-qubit phase gate," *Nature*, vol. 422, no. 6930, pp. 412–415, 2003.

[25] C. Ballance, T. Harty, N. Linke, M. Sepiol, and D. Lucas, "High-fidelity quantum logic gates using trapped-ion hyperfine qubits," *Physical review letters*, vol. 117, no. 6, p. 060504, 2016.

[26] T. Ruster, C. T. Schmiegelow, H. Kaufmann, C. Warschburger, F. Schmidt-Kaler, and U. G. Poschinger, "A long-lived zeeman trapped-ion qubit," *Applied Physics B*, vol. 122, no. 10, p. 254, 2016.

[27] Y. Wang, M. Um, J. Zhang, S. An, M. Lyu, J.-N. Zhang, L.-M. Duan, D. Yum, and K. Kim, "Single-qubit quantum memory exceeding ten-minute coherence time," *Nature Photonics*, vol. 11, no. 10, pp. 646–650, 2017.

[28] R. Barends, J. Kelly, A. Megrant, A. Veitia, D. Sank, E. Jeffrey, T. C. White, J. Mutus, A. G. Fowler, B. Campbell, *et al.*, "Superconducting quantum circuits at the surface code threshold for fault tolerance," *Nature*, vol. 508, no. 7497, pp. 500–503, 2014.

[29] H. Levine, A. Keesling, A. Omran, H. Bernien, S. Schwartz, A. S. Zibrov, M. Endres, M. Greiner, V. Vuletić, and M. D. Lukin, "High-fidelity control and entanglement of rydberg-atom qubits," *Physical review letters*, vol. 121, no. 12, p. 123603, 2018.

[30] J. P. Gaebler, T. R. Tan, Y. Lin, Y. Wan, R. Bowler, A. C. Keith, S. Glancy, K. Coakley, E. Knill, D. Leibfried, *et al.*, "High-fidelity universal gate set for be 9+ ion qubits," *Physical review letters*, vol. 117, no. 6, p. 060505, 2016.

[31] A. Erhard, J. J. Wallman, L. Postler, M. Meth, R. Stricker, E. A. Martinez, P. Schindler, T. Monz, J. Emerson, and R. Blatt, "Characterizing large-scale quantum computers via cycle benchmarking," *Nature communications*, vol. 10, no. 1, pp. 1–7, 2019.

[32] P. Klimov, J. Kelly, Z. Chen, M. Neeley, A. Megrant, B. Burkett, R. Barends, K. Arya, B. Chiaro, Y. Chen, *et al.*, "Fluctuations of energy-relaxation times in superconducting qubits," *Physical review letters*, vol. 121, no. 9, p. 090502, 2018.

[33] V. Schäfer, C. Ballance, K. Thirumalai, L. Stephenson, T. Ballance, A. Steane, and D. Lucas, "Fast quantum logic gates with trapped-ion qubits," *Nature*, vol. 555, no. 7694, pp. 75–78, 2018.

[34] B. Lekitsch, S. Weidt, A. G. Fowler, K. Mølmer, S. J. Devitt, C. Wunderlich, and W. K. Hensinger, "Blueprint for a microwave trapped ion quantum computer," *Science Advances*, vol. 3, no. 2, p. e1601540, 2017.

[35] A. W. Harrow and A. Montanaro, "Quantum computational supremacy," *Nature*, vol. 549, no. 7671, pp. 203–209, 2017.

[36] J. Wong-Campos, S. Moses, K. Johnson, and C. Monroe, "Demonstration of two-atom entanglement with ultrafast optical pulses," *Physical Review Letters*, vol. 119, no. 23, p. 230501, 2017.

[37] J. M. Martinis, "Qubit metrology for building a fault-tolerant quantum computer," *npj Quantum Information*, vol. 1, no. 1, pp. 1–3, 2015.

[38] A. G. Fowler, M. Mariantoni, J. M. Martinis, and A. N. Cleland, "Surface codes: Towards practical large-scale quantum computation," *Physical Review A*, vol. 86, no. 3, p. 032324, 2012.

[39] G. Pagano, P. Hess, H. Kaplan, W. Tan, P. Richerme, P. Becker, A. Kyprianidis, J. Zhang, E. Birckelbaw, M. Hernandez, *et al.*, "Cryogenic trapped-ion system for large scale quantum simulation," *Quantum Science and Technology*, vol. 4, no. 1, p. 014004, 2018.

[40] C. D. Bruzewicz, R. McConnell, J. Chiaverini, and J. M. Sage, "Scalable loading of a two-dimensional trapped-ion array," *Nature communications*, vol. 7, no. 1, pp. 1–6, 2016.

[41] "Our trapped ion technology."

[42] H. J. Kimble, "The quantum internet," *Nature*, vol. 453, no. 7198, pp. 1023–1030, 2008.

[43] D. Kielpinski, C. Monroe, and D. J. Wineland, "Architecture for a large-scale ion-trap quantum computer," *Nature*, vol. 417, no. 6890, pp. 709–711, 2002.

[44] M. Rowe, A. Ben-Kish, B. Demarco, D. Leibfried, V. Meyer, J. Beall, J. Britton, J. Hughes, W. Itano, B. Jelenković, *et al.*, "Transport of quantum states and separation of ions in a dual rf ion trap," *Quantum Information and Computation*, vol. 2, no. 4, pp. 257–271, 2002.

[45] W. Hensinger, S. Olmschenk, D. Stick, D. Hucul, M. Yeo, M. Acton, L. Deslauriers, C. Monroe, and J. Rabchuk, "T-junction ion trap array for two-dimensional ion shuttling, storage, and manipulation," *Applied Physics Letters*, vol. 88, no. 3, p. 034101, 2006.

[46] C. Monroe and J. Kim, "Scaling the ion trap quantum processor," *Science*, vol. 339, no. 6124, pp. 1164–1169, 2013.

[47] D. Hucul, I. V. Inlek, G. Vittorini, C. Crocker, S. Debnath, S. M. Clark, and C. Monroe, "Modular entanglement of atomic qubits using photons and phonons," *Nature Physics*, vol. 11, no. 1, pp. 37–42, 2015.

[48] L. Stephenson, D. Nadlinger, B. Nichol, S. An, P. Drmota, T. Ballance, K. Thirumalai, J. Goodwin, D. Lucas, and C. Ballance, "High-rate, high-fidelity entanglement of qubits across an elementary quantum network," *Physical Review Letters*, vol. 124, no. 11, p. 110501, 2020.

[49] A. Stute, B. Casabone, P. Schindler, T. Monz, P. Schmidt, B. Brandstätter, T. Northup, and R. Blatt, "Tunable ion–photon entanglement in an optical cavity," *Nature*, vol. 485, no. 7399, pp. 482–485, 2012.

[50] T. Northup and R. Blatt, "Quantum information transfer using photons," *Nature photonics*, vol. 8, no. 5, pp. 356–363, 2014.

[51] B. Casabone, K. Friebe, B. Brandstätter, K. Schüppert, R. Blatt, and T. Northup, "Enhanced quantum interface with collective ion-cavity coupling," *Physical review letters*, vol. 114, no. 2, p. 023602, 2015.

[52] A. Stute, B. Casabone, B. Brandstätter, K. Friebe, T. Northup, and R. Blatt, "Quantum-state transfer from an ion to a photon," *Nature photonics*, vol. 7, no. 3, pp. 219–222, 2013.

[53] M. Keller, B. Lange, K. Hayasaka, W. Lange, and H. Walther, "Continuous generation of single photons with controlled waveform in an ion-trap cavity system," *Nature*, vol. 431, no. 7012, pp. 1075–1078, 2004.

[54] V. Krutyanskiy, M. Meraner, J. Schupp, V. Krcmarsky, H. Hainzer, and B. P. Lanyon, "Light-matter entanglement over 50 km of optical fibre," *npj Quantum Information*, vol. 5, no. 1, pp. 1–5, 2019.

[55] L.-M. Duan, M. D. Lukin, J. I. Cirac, and P. Zoller, "Long-distance quantum communication with atomic ensembles and linear optics," *Nature*, vol. 414, no. 6862, pp. 413–418, 2001.

[56] A. Imamoḡlu, H. Schmidt, G. Woods, and M. Deutsch, "Strongly interacting photons in a nonlinear cavity," *Physical Review Letters*, vol. 79, no. 8, p. 1467, 1997.

[57] K. M. Gheri, W. Alge, and P. Grangier, "Quantum analysis of the photonic blockade mechanism," *Physical Review A*, vol. 60, no. 4, p. R2673, 1999.

[58] M. Harlander, M. Brownnutt, W. Hänsel, and R. Blatt, "Trapped-ion probing of light-induced charging effects on dielectrics," *New Journal of Physics*, vol. 12, no. 9, p. 093035, 2010.

[59] D. Hunger, T. Steinmetz, Y. Colombe, C. Deutsch, T. W. Hänsch, and J. Reichel, "A fiber fabry–perot cavity with high finesse," *New Journal of Physics*, vol. 12, no. 6, p. 065038, 2010.

[60] Y. Colombe, T. Steinmetz, G. Dubois, F. Linke, D. Hunger, and J. Reichel, "Strong atom–field coupling for bose–einstein condensates in an optical cavity on a chip," *Nature*, vol. 450, no. 7167, pp. 272–276, 2007.

[61] B. Brandstätter, A. McClung, K. Schüppert, B. Casabone, K. Friebe, A. Stute, P. O. Schmidt, C. Deutsch, J. Reichel, R. Blatt, *et al.*, "Integrated fiber-mirror ion trap for strong ion-cavity coupling," *Review of Scientific Instruments*, vol. 84, no. 12, p. 123104, 2013.

[62] T. Ballance, H. Meyer, P. Kobel, K. Ott, J. Reichel, and M. Köhl, "Cavity-induced backaction in purcell-enhanced photon emission of a single ion in an ultraviolet fiber cavity," *Physical Review A*, vol. 95, no. 3, p. 033812, 2017.

[63] H. Takahashi, J. Morphew, F. Oručević, A. Noguchi, E. Kassa, and M. Keller, "Novel laser machining of optical fibers for long cavities with low birefringence," *Optics express*, vol. 22, no. 25, pp. 31317–31328, 2014.

[64] E. Kassa, H. Takahashi, C. Christoforou, and M. Keller, "Precise positioning of an ion in an integrated paul trap-cavity system using radiofrequency signals," *Journal of Modern Optics*, vol. 65, no. 5-6, pp. 520–528, 2018.

[65] H. Takahashi, E. Kassa, C. Christoforou, and M. Keller, "Strong coupling of a single ion to an optical cavity," *Physical Review Letters*, vol. 124, no. 1, p. 013602, 2020.

[66] C. Christoforou, C. Pignot, E. Kassa, H. Takahashi, and M. Keller, "Enhanced ion-cavity coupling through cavity cooling in the strong coupling regime," *arXiv preprint arXiv:2003.01507*, 2020.

[67] H. Takahashi, E. Kassa, C. Christoforou, and M. Keller, "Cavity-induced anticorrelated photon-emission rates of a single ion," *Physical Review A*, vol. 96, no. 2, p. 023824, 2017.

[68] S. Earnshaw, "On the nature of the molecular forces which regulate the constitution of the luminiferous ether," *TCaPS*, vol. 7, p. 97, 1848.

[69] W. Paul, "Electromagnetic traps for charged and neutral particles," *Reviews of modern physics*, vol. 62, no. 3, p. 531, 1990.

[70] C. J. Foot *et al.*, *Atomic physics*, vol. 7. Oxford University Press, 2005.

[71] E. Kassa, "Student-led elearning modules: Modulex: Quadrupole ion traps," 2015.

[72] D. Leibfried, R. Blatt, C. Monroe, and D. Wineland, "Quantum dynamics of single trapped ions," *Reviews of Modern Physics*, vol. 75, no. 1, p. 281, 2003.

[73] E. Kassa, *Single ion coupled to a high-finesse optical fibre cavity for cQED in the strong coupling regime*. PhD thesis, University of Sussex, 2017.

[74] H. Takahashi, A. Wilson, A. Riley-Watson, F. Oručević, N. Seymour-Smith, M. Keller, and W. Lange, "An integrated fiber trap for single-ion photonics," *New Journal of Physics*, vol. 15, no. 5, p. 053011, 2013.

[75] D. J. Griffiths, "Introduction to electrodynamics," 2005.

[76] H. Kogelnik and T. Li, "Laser beams and resonators," *Applied optics*, vol. 5, no. 10, pp. 1550–1567, 1966.

[77] A. G. Riley-Watson, *A fibre-based single-photon source*. PhD thesis, University of Sussex, 2013.

[78] G. Brooker, *Modern classical optics*, vol. 8. Oxford University Press, 2003.

[79] P. Meystre and M. Sargent, *Elements of quantum optics*. Springer Science & Business Media, 2007.

[80] S. M. Tan, "A quantum optics toolbox for matlab 5," *J. Opt. B: Quantum Semiclass. Opt*, vol. 1, p. 161, 1999.

[81] P. F. Herskind, A. Dantan, M. Albert, J. P. Marler, and M. Drewsen, "Positioning of the rf potential minimum line of a linear paul trap with micrometer precision," *Journal of Physics B: Atomic, Molecular and Optical Physics*, vol. 42, no. 15, p. 154008, 2009.

[82] J. Cirac, A. Parkins, R. Blatt, and P. Zoller, "Cooling of a trapped ion coupled strongly to a quantized cavity mode," *Optics communications*, vol. 97, no. 5-6, pp. 353–359, 1993.

[83] J. I. Cirac, R. Blatt, P. Zoller, and W. D. Phillips, "Laser cooling of trapped ions in a standing wave," *Physical Review A*, vol. 46, no. 5, p. 2668, 1992.

[84] D. J. Wineland, J. Dalibard, and C. Cohen-Tannoudji, "Sisyphus cooling of a bound atom," *JOSA B*, vol. 9, no. 1, pp. 32–42, 1992.

[85] C. Monroe, R. Raussendorf, A. Ruthven, K. Brown, P. Maunz, L.-M. Duan, and J. Kim, "Large-scale modular quantum-computer architecture with atomic memory and photonic interconnects," *Physical Review A*, vol. 89, no. 2, p. 022317, 2014.

[86] H.-J. Briegel, W. Dür, J. I. Cirac, and P. Zoller, "Quantum repeaters: the role of imperfect local operations in quantum communication," *Physical Review Letters*, vol. 81, no. 26, p. 5932, 1998.

[87] T. Wilk, S. C. Webster, A. Kuhn, and G. Rempe, "Single-atom single-photon quantum interface," *Science*, vol. 317, no. 5837, pp. 488–490, 2007.